Crystal-field and spin-orbit effects on correlated single-layered t_{2g}^n perovskites: An LDA+DMFT study

Von der Fakultät für Mathematik, Informatik und Naturwissenschaften der RWTH Aachen University zur Erlangung des akademischen Grades einer Doktorin der Naturwissenschaften genehmigte Dissertation

vorgelegt von

Neda Riahisamani, M.Sc.
aus Saman, Iran

Berichter: Univ.-Prof. Eva Pavarini, Ph.D.
Univ.-Prof. Stefan Wessel, Ph.D.

Tag der mündlichen Prüfung: 24. Januar 2024

Diese Dissertation ist auf den Internetseiten der Universitätsbibliothek online verfügbar.

Abstract

Systems with strongly-correlated electrons have properties that are hard to explain. This is because, in these materials, characterized by open d or f electron shells, the strength of Coulomb repulsion is significant. In this situation, the effect of electron-electron correlation cannot be described via a static mean-field. Among strongly-correlated systems, single-layered perovskites are unique because several competing interactions have similar strength. This makes it more challenging to disentangle the key mechanisms of a given phenomenon from all the rest. The state-of-the-art approach to study this class of systems is the combination of density-functional theory (DFT), e.g., in the local-density approximation (LDA), with dynamical mean-field theory (DMFT). In this approach, for a given system, a material-specific Hubbard model is obtained via DFT-based calculations. In the next step, within DMFT the Hubbard model is mapped onto a self-consistent auxiliary quantum-impurity problem, which can be solved exactly using numerical techniques such as continuous-time quantum Monte Carlo.
In this thesis, we adopt the LDA+DMFT method to study the low energy electronic properties of single-layered t_{2g}^n perovskites. Firstly, we investigate the effects of the crystal-field splitting, $\varepsilon_{\mathrm{CF}}$, on the system. We find that for very large $|\varepsilon_{\mathrm{CF}}|$ the three-band model can be replaced by one with fewer degrees of freedom. We show that low energy many-body effects modify the Fermi surface shape, by either reducing or enhancing the effective $\varepsilon_{\mathrm{CF}}$, depending on n and $\varepsilon_{\mathrm{CF}}$. These low energy effects differ sizably from the high energy ones, the Hartree-Fock shifts. We show how the effective-masses evolve as a function of $\varepsilon_{\mathrm{CF}}$. In the second part of the thesis, we investigate the effects of the spin-orbit (SO) interaction. We find that the SO interaction couples the states considerably. Thus, it is convenient to discuss the results in the natural orbital basis. We show how the form of the latter evolves with $\varepsilon_{\mathrm{CF}}$. We discuss the effects on mass enhancement and scattering rates. We identify the crystal-field value for which the systems have occupations corresponding to a degenerate t_{2g} shell. Overall, many-body effects are more significant for n=2 and n=4.

Zusammenfassung

Systeme mit stark korrelierten Elektronen haben Eigenschaften, die schwer zu erklären sind. Das liegt daran, dass in diesen Materialien mit meist offenen d oder f Schalen die Stärke der Coulomb Abstoßung erheblich ist. In dieser Situation kann die Wirkung von Korrelationen nicht durch ein statisches Molekularfeld beschrieben werden. Unter den stark korrelierten Systemen sind einschichtige Perowskite dadurch ausgezeichnet, dass mehrere konkurrierende Wechselwirkungen eine ähnliche Stärke aufweisen. Dies macht es schwieriger, die dominierenden Mechanismen hinter einem bestimmten Phäno mens von allen anderen zu trennen. Der Stand der Technik zur Untersuchung stark korrelierter Materialien ist die Kombination von Dichtefunktionale Theorie (DFT), z.B. in der lokalen Dichte-Näherung (LDA), mit der dynamischen Molekularfeld Theorie (DMFT). Bei diesem Ansatz kann für ein bestimmtes System ein materialspezifisches Hubbard Modell aus DFT-basierte Rechnungen konstruiert werden. Im Rahmen der DMFT wird das Hubbard Modell dann auf ein selbstkonsistentes Quanten-Störstellen Problem abgebildet, das mit Hilfe numerischer Verfahren wie der Quanten Monte Carlo Methode in kontinuierlichen Zeit exakt gelöst werden kann.
In dieser Arbeit wird die LDA+DMFT Methode angewandt, um die elektronischen Eigenschaften von einschichtigen t_{2g}^n Perowskiten im Bereich niederenergetischer Anregungen zu untersuchen; dabei ist n die Füllung der t_{2g} Orbitale. Zunächst untersuchen wir die Auswirkungen des Kristallfeldes auf das System. Wir stellen fest, dass für sehr große $|\varepsilon_{\mathrm{CF}}|$ das Dreiband-Modell durch ein Modell mit weniger Bändern ersetzt werden kann. Wir zeigen, dass niederenergetische Vielteilcheneffekte die Form der Fermifläche modifizieren, indem sie das effektive $\varepsilon_{\mathrm{CF}}$ in Abhängigkeit von n und $\varepsilon_{\mathrm{CF}}$ entweder verringern oder erhöhen. Diese Niederenergie-Effekte unterscheiden sich deutlich von den Hochenergie-Effekten, der Hartree-Fock Verschiebung. Wir zeigen, wie sich die effektive Masse als Funktion von $\varepsilon_{\mathrm{CF}}$ entwickelt. Im zweiten Teil der Arbeit untersuchen wir die Auswirkungen der Spin-Orbit (SO) Kopplung. Wir stellen fest, dass die SO-Kopplung die Zustände erheblich koppelt. Daher ist es zweckmäßig, die Ergebnisse in der Basis der natürlichen Orbitale zu diskutieren. Wier zweigen wie sich die natürlichen Orbitale mit $\varepsilon_{\mathrm{CF}}$ entwickeln und diskutieren die Auswirkungen auf die Erhöhung der effektiven Masse und die Streuraten. Schließlich identifizieren wier den Wert der Kristallfeld-Aufspaltung für die Orbital-beseztung einer entarteten t_{2g} Schale entsprechen. Dabei sind die Vielteilcheneffekte für die

Füllungen n=2 und n=4 besonders ausgeprägt.

Contents

1 Introduction **1**

2 Density-functional theory **3**
2.1 Kohn-Sham equations 4
2.2 Local-density approximation 6

3 Dynamical mean-field theory **8**
3.1 Material-specific Hubbard models 8
3.2 One-band Hubbard model 10
3.3 DMFT for the one-band Hubbard model 11

4 Quantum Monte Carlo solvers **15**
4.1 Basic principles of Monte Carlo methods 15
4.2 Continuous-time quantum Monte Carlo 16

5 Multi-orbital Hubbard Hamiltonian **21**
5.1 Coulomb interaction matrix 21
5.2 Crystal-field matrix 25
5.3 Single-particle Green functions 30
5.3.1 Matsubara Green functions 31

6 Electronic properties of t_{2g} layered perovskites **34**
6.1 Representative materials 36
6.2 Results without SO interaction 40
6.2.1 Orbital-resolved spectral functions 40
6.2.2 Occupation numbers and orbital polarization 48
6.2.3 Effective-masses and scattering rates 59
6.2.4 Reduction of model size 64

6.2.5 Crystal-field splitting correction 70
6.3 Effects of the SO interaction 79
6.3.1 Results in the t_{2g} basis 81
6.3.2 Results in the natural orbitals basis 89

7 Summary **99**

A Kramers-Kronig relations **101**

1

Introduction

The general non-relativistic Hamiltonian describing all problems in condensed matter physics, in atomic units ($\hbar$=m_e=$|e|$=1) is:

$$\begin{aligned} \hat{H} &= \hat{T}_e + \hat{V}_{ee} + \hat{V}_{en} + \hat{V}_{nn} + \hat{T}_n \\ &= -\frac{1}{2}\sum_i \nabla^2_{\mathbf{r}_i} + \frac{1}{2}\sum_{i\neq i'} \frac{1}{|\mathbf{r}_i - \mathbf{r}_{i'}|} - \sum_{i\alpha} \frac{Z_\alpha}{|\mathbf{r}_i - \mathbf{R}_\alpha|} \\ &+ \frac{1}{2}\sum_{\alpha\neq\alpha'} \frac{Z_\alpha Z_{\alpha'}}{|\mathbf{R}_\alpha - \mathbf{R}_{\alpha'}|} - \sum_\alpha \frac{\nabla^2_{\mathbf{R}_\alpha}}{2M_\alpha}. \end{aligned} \tag{1.1}$$

Eq. (1.1) consists of the kinetic energy of electrons and nuclei, $\hat{T}_e$ and $\hat{T}_n$, the electron-electron Coulomb interaction, $\hat{V}_{ee}$, the nucleus-nucleus Coulomb interaction, $\hat{V}_{nn}$, and the electron-nucleus Coulomb interaction, $\hat{V}_{en}$. Here, the vectors $\{\mathbf{R}_\alpha\}$ represent the coordinates of N_n nuclei with masses M_α and atomic numbers Z_α, and $\{\mathbf{r}_i\}$ are the positions of the N_e electrons. Since the mass of the electrons is much smaller than those of the nuclei, ($m_e \ll M_\alpha$), one can decouple nuclei and electrons. This is the *Born-Oppenheimer approximation*, which enables us to write the total wave-function of Hamiltonian (1.1) as a product of the wave-function of the electrons, $\psi(\{\mathbf{r}_i\}\,;\{\mathbf{R}_\alpha\})$, and the wave-function of the nuclei, $\Phi(\{\mathbf{R}_\alpha\})$,

$$\Psi(\{\mathbf{r}_i\}\,,\{\mathbf{R}_\alpha\}) = \psi(\{\mathbf{r}_i\}\,;\{\mathbf{R}_\alpha\})\Phi(\{\mathbf{R}_\alpha\}).$$

The Hamiltonian for the electrons, $\hat{H}_e$, is then:

$$\begin{aligned} \hat{H}_e &= \hat{T}_e + \hat{V}_{ee} + \hat{V}_{en} + \hat{V}_{nn} \\ &= -\frac{1}{2}\sum_i \nabla^2_{\mathbf{r}_i} + \frac{1}{2}\sum_{i\neq i'} \frac{1}{|\mathbf{r}_i - \mathbf{r}_{i'}|} - \sum_{i\alpha} \frac{Z_\alpha}{|\mathbf{r}_i - \mathbf{R}_\alpha|} + \frac{1}{2}\sum_{\alpha\neq\alpha'} \frac{Z_\alpha Z_{\alpha'}}{|\mathbf{R}_\alpha - \mathbf{R}_{\alpha'}|}. \end{aligned} \tag{1.2}$$

In the non-interacting limit, $\hat{V}_{ee}$=0, $\hat{H}_e$ is separable, and the electrons are independent. While the independent-electron approximation strongly simplifies the problem, in real materials $\hat{V}_{ee}\neq 0$. In this situation, with increasing the number of the electrons, finding the wave-function of $\hat{H}_e$ can become quickly an unfeasible task, even for a single atom. To understand why finding the exact solution of the *quantum many-body problem* is impossible in practice beyond the few-electron case, let us consider a single iron atom. For N particles, the Schrödinger equation is a partial differential equation with $3N$ degrees of freedom. Having 26 electrons in a single iron atom, the associated electronic wave-function, $\psi(\mathbf{r}_1, \mathbf{r}_2, ..., \mathbf{r}_{26})$, is a function of 78 coordinates (ignoring spin). If we would like to store this wave-function on a $10 \times 10 \times 10$ grid, we would have to record 10^{78} values. Unfortunately, there is not enough matter in the visible universe for storing even the wave-function of a single iron atom. One can at this point ask if reductionism works. Taking it to the extreme, reductionism implies that, knowing the fundamental particles and their interactions, everything else can be calculated. However, it is already unclear what the fundamental particles are. If we consider water, one could say that it is made of molecules. Molecules are made of atoms, atoms of electrons and protons, protons of quarks and so on. Knowing this does not explain alone why water is wet. Understanding the physics of a many-body system inevitably involves understanding how these particles interact with each other [1]. This is where the problem becomes difficult very quickly. We understand the Schrödinger equation extremely well for a single particle, but for a very large number of particles it cannot be solved exactly, even on the world's biggest computers. To make progress, it is therefore necessary to find approximate methods that capture the crucial properties. In this thesis, we will adopt one of these successful approximate schemes to explain the electronic properties of one important family of materials, t_{2g} layered perovskites.

2

Density-functional theory

Density-functional theory (DFT) is one of the most popular and successful quantum mechanical approaches to study the properties of many-electron systems [2, 3]. To explain how DFT works, it is useful to take a step back and recall some elementary quantum mechanics. In quantum mechanics all information about the system can be obtained from the wave-function, ψ. In the non-relativistic limit, this wave-function is calculated from the Schrödinger equation. The usual quantum mechanical approach to the Schrödinger equation can be summarized by the following sequence

$$v_{ext}(\mathbf{r}) \Longrightarrow \psi(\mathbf{r}_1, \mathbf{r}_2, ..., \mathbf{r}_N) \Longrightarrow \text{observables},$$

i.e., one specifies the system by choosing the external potential, solves the Schrödinger equation for the ground state ψ and then calculates the observables by taking the expectation values of the operators with this wave-function. One of the observables which can be obtained in this way is the particle density

$$n(\mathbf{r}) = N \int d^3r_2 \int d^3r_3 \ ... \int d^3r_N \psi^*(\mathbf{r}, \mathbf{r}_2, ..., \mathbf{r}_N)\psi(\mathbf{r}, \mathbf{r}_2, ..., \mathbf{r}_N). \qquad (2.1)$$

DFT shifts the focus from ψ to $n(\mathbf{r})$, a function of only three coordinates. This approach is now the workhorse for electronic calculations. The extent to which DFT has contributed to science is reflected in the 1998 Nobel Prize in Chemistry, awarded to the pioneers, Kohn and Pople.
The DFT approach is based on the Hohenberg-Kohn theorem, which can be summarized by this sequence

$$n(\mathbf{r}) \Longrightarrow \psi(\mathbf{r}_1, \mathbf{r}_2, ..., \mathbf{r}_N) \Longrightarrow v_{ext}(\mathbf{r}).$$

The Hohenberg-Kohn theorem thus states that *there is a one-to-one correspondence between the ground state density of a N_e electron system and the external potential acting on it.*
For any material described by Eq. (1.2), the ground state total energy is a functional of the electron density, $E[n]$, which is minimized by the ground state density. Here, $E[n]$ can be written as

$$E[n] = F[n] + \int d\mathbf{r}\, v_{ext}(\mathbf{r}) n(\mathbf{r}).$$

The term $F[n] = T_e[n] + V_{ee}[n]$, the sum of the kinetic and the electron-electron interaction energy is a universal functional, $v_{ext}(\mathbf{r})$ is the system-specific potential energy, and it originates from V_{en}. The obstacle is that finding $n(\mathbf{r})$ still requires, in principle, the solution of the many-body problem. Kohn and Sham have shown, however, that $n(\mathbf{r})$ can be obtained by solving the Schrödinger equation of a fictitious non-interacting system [4]. I will explain how in the next section.

2.1 Kohn-Sham equations

The total-energy of the electronic system, thanks to the Hohenberg-Kohn theorem, can be written as

$$E[n] = T_e[n] + V_{ee}[n] + V_{ext}[n]. \tag{2.2}$$

It is convenient to introduce the two-electron density,

$$n(\mathbf{r}, \mathbf{r}') = n(\mathbf{r}) n(\mathbf{r}') g(\mathbf{r}, \mathbf{r}'),$$

where $g(\mathbf{r}, \mathbf{r}')$ is the pair correlation function. Then the Coulomb repulsion energy between the electrons can be expressed in terms of $g(\mathbf{r}, \mathbf{r}')$:

$$V_{ee} = \frac{1}{2} \int d\mathbf{r}\, d\mathbf{r}' \frac{n(\mathbf{r}) n(\mathbf{r}')}{|\mathbf{r} - \mathbf{r}'|} + \frac{1}{2} \int d\mathbf{r}\, d\mathbf{r}' \frac{n(\mathbf{r}) n(\mathbf{r}')(g(\mathbf{r}, \mathbf{r}') - 1)}{|\mathbf{r} - \mathbf{r}'|}, \tag{2.3}$$

where the first term is the average Coulomb interaction, the *Hartree energy*, V_H, and the second term is the *Coulomb exchange-correlation energy*, U_{xc}.
The kinetic energy, $T_e[n]$ can be decomposed into one part that represents the kinetic energy of the non-interacting particles with the density n, $T_s[n]$,

and one that represents the rest, $T_c[n]$. Indeed, $T_s[n]$ can be easily expressed in terms of the single-electron orbitals $\phi_i(\mathbf{r})$ of the non-interacting electrons with the density n, as:

$$T_s[n] = -\frac{1}{2}\sum_{i=1}^{N_e}\int d^3r\,\phi_i^*(\mathbf{r})\nabla_{\mathbf{r}}^2\phi_i(\mathbf{r}). \tag{2.4}$$

We can now rewrite the exact energy functional as

$$E[n] = T_e[n] + V_{ee}[n] + V_{ext}[n] = T_s[n] + V_H[n] + E_{xc}[n] + V_{ext}[n]. \tag{2.5}$$

Equation (2.5) is exact, but of course the *exchange-correlation functional*, $E_{xc}[n]$, is unknown and includes a Coulomb ($V_{ee}[n] - V_H[n]$) and a kinetic energy ($T[n] - T_s[n]$) term. Minimizing Eq. (2.5) results in the condition

$$\begin{aligned} 0 = \frac{\delta E[n]}{\delta(n(\mathbf{r}))} &= \frac{\delta T_s[n]}{\delta(n(\mathbf{r}))} + \frac{\delta V_{ext}[n]}{\delta(n(\mathbf{r}))} + \frac{\delta V_H[n]}{\delta(n(\mathbf{r}))} + \frac{\delta E_{xc}[n]}{\delta(n(\mathbf{r}))} \\ &= \frac{\delta T_s[n]}{\delta(n(\mathbf{r}))} + \upsilon_{ext}(\mathbf{r}) + \upsilon_H(\mathbf{r}) + \upsilon_{xc}(\mathbf{r}), \end{aligned} \tag{2.6}$$

where $\upsilon_{ext}(\mathbf{r})$ is the external potential, $\upsilon_H(\mathbf{r})$ yields the Hartree potential introduced in Eq. (2.3) and $\upsilon_{xc}(\mathbf{r})$ can only be calculated explicitly when an approximation for $E_{xc}[n]$ has been chosen.
Let us consider now a system of non-interacting electrons moving in the potential $\upsilon_s(\mathbf{r})$. For this system, the minimization at self-consistency condition is simply

$$0 = \frac{\delta E_s[n]}{\delta(n(\mathbf{r}))} = \frac{\delta T_s[n]}{\delta(n(\mathbf{r}))} + \frac{\delta V_s[n]}{\delta(n(\mathbf{r}))} = \frac{\delta T_s[n]}{\delta(n(\mathbf{r}))} + \upsilon_s(\mathbf{r}). \tag{2.7}$$

The density obtained solving this Euler equation is $n_s(\mathbf{r})$. Equations (2.6) and (2.7) have the same solution, $n_s(\mathbf{r}) \equiv n(\mathbf{r})$, if υ_s is chosen to be

$$\upsilon_s(\mathbf{r}) = \upsilon_{ext}(\mathbf{r}) + \upsilon_H(\mathbf{r}) + \upsilon_{xc}(\mathbf{r}). \tag{2.8}$$

Consequently, one can calculate the density of the interacting (many-body) system in the potential $\upsilon_{ext}(\mathbf{r})$, by solving the equation of the non-interacting (single-body) system in the potential $\upsilon_s(\mathbf{r})$.
The Schrödinger equation of the auxiliary system,

$$\left[-\frac{\nabla_{\mathbf{r}}^2}{2} + \upsilon_s(\mathbf{r})\right]\phi_i(\mathbf{r}) = \epsilon_i\phi_i(\mathbf{r}), \tag{2.9}$$

gives the orbitals which produce $n(\mathbf{r})$ of the original system,

$$n(\mathbf{r}) \equiv n_s(\mathbf{r}) = \sum_{i=1}^{N_e} |\phi_i(\mathbf{r})|^2. \tag{2.10}$$

Equations (2.8) to (2.10) are known as the *Kohn-Sham equations* [5]. In practice, we use the following algorithm:

1. Start with an initial guess for $n(\mathbf{r})$.
2. Calculate the corresponding $v_s(\mathbf{r})$, and solve the differential equation in Eq. (2.9) for ϕ_i.
3. Obtain the new density from Eq. (2.10) and start again.

The process is repeated, until it converges. For the self-consistent solution n_0, the total energy can be expressed as

$$E_0 = \sum_{i=1}^{N_e} \epsilon_i - \frac{1}{2} \int d\mathbf{r} \int d\mathbf{r}' \, \frac{n_0(\mathbf{r}) n_0(\mathbf{r}')}{|\mathbf{r} - \mathbf{r}'|} - \int d\mathbf{r} \, v_{xc}(\mathbf{r}) n_0(\mathbf{r}) + E_{xc}[n_0]. \tag{2.11}$$

Equation (2.11) follows from rewriting $V_{ext}[n]$ in (2.5) by means of (2.8) as

$$\begin{aligned} V_{ext}[n] &= \int d^3r \, v_{ext}(\mathbf{r}) n(\mathbf{r}) \\ &= \int d^3r \, \left[v_s(\mathbf{r}) - v_H(\mathbf{r}) - v_{xc}(\mathbf{r}) \right] n(\mathbf{r}) \\ &= V_s[n] - \int d^3r \, \left[v_H(\mathbf{r}) + v_{xc}(\mathbf{r}) \right] n(\mathbf{r}), \end{aligned} \tag{2.12}$$

and identifying the energy of the non-interacting (Kohn-Sham) system as $E_s = \sum_{i=1}^{N_e} \epsilon_i = T_s + V_s$ [6, 7].

2.2 Local-density approximation

One of the best known approximations to E_{xc} is the *local-density approximation* (LDA). In the LDA, the exchange-correlation functional is approximated in the form

$$E_{xc}^{(LDA)}[n] = \int d\mathbf{r} \, \varepsilon_{xc}(n(\mathbf{r})) n(\mathbf{r}), \tag{2.13}$$

where $\varepsilon_{xc}(n(\mathbf{r}))$ is the exchange-correlation energy per electron of a homogeneous gas of interacting electrons with density $n(\mathbf{r})$. In the LDA, one assumes that the real inhomogeneous system, with density $n(\mathbf{r})$ can be decomposed in small cells in each of which $n(\mathbf{r})$ is approximately constant. In each cell (i.e., locally) one can then use the per volume energy of the homogeneous system to approximate the contribution of the cell to the real inhomogeneous one. Therefore, the LDA is particularly justified in systems with reasonably slowly varying spatial density.
The exchange-correlation potential produced by the functional in Eq. (2.13), becomes

$$\upsilon_{xc}^{(LDA)}[n] \equiv \frac{\delta E_{xc}^{(LDA)}[n]}{\delta n(\mathbf{r})}. \tag{2.14}$$

Ceperley and Adler [8] in 1986, performed Quantum Monte Carlo (QMC) calculations for the interacting homogeneous electron gas at various densities. By fitting their results, analytic expression of υ_{xc} were obtained, that can be implemented in DFT codes.
The LDA has proved very successful even for systems which are quite different from the electron gas, e.g., for surfaces, where the density varies rapidly. However, for systems with strong local interaction, like the materials at the center of this thesis, the LDA gives qualitatively wrong results. In this case, we use the LDA only as a starting point to build material-specific many-body models.

3

Dynamical mean-field theory

Although DFT can be considered the standard model for electronic structure calculations, the Kohn-Sham approach does not capture the physics of strongly-correlated systems. In many materials with partially filled d and f shells, such as transition-metal oxides, electrons occupy narrow bands. This enhances the importance of the Coulomb interaction between the electrons, making them "strongly-correlated" [9]. In this section, we introduce the dynamical mean-field theory (DMFT), which is one of the most successful methods for studying strongly-correlated electron systems. Before we do this, we will discuss the representative models which we want to solve.

3.1 Material-specific Hubbard models

Strongly-correlated systems have been studied for a long time using simple low energy models. In recent years, it became possible to construct minimal material-specific models from first principles. Since the Kohn-Sham orbitals obtained via, e.g., the LDA, carry the essential information about a given material, the construction of material-specific many-body models naturally starts from LDA calculations. Let us consider a lattice with periodic potential, $v_s(\mathbf{r})=v_s(\mathbf{r}+\mathbf{R})$, where $\mathbf{R}$ denotes a lattice vector. The localized Wannier function which is localized at the lattice site i, can be expressed as

$$\psi_{i\alpha}(\mathbf{r}) = \frac{1}{\sqrt{N}_{\mathbf{k}}} \sum_{\mathbf{k}} \mathrm{e}^{-i\mathbf{k}.\mathbf{R}_i} \psi_{\alpha\mathbf{k}}(\mathbf{r}), \tag{3.1}$$

where the index α=(σ, s, n) represents spin index σ, site index s inside the unit cell and band index n; $\mathbf{k}$ is a momentum vector and $N_{\mathbf{k}}$ denotes the number of $\mathbf{k}$ points in the Brillouin zone. Writing Hamiltonian (1.2) in second quantization in the basis of the LDA Wannier functions, one finds

$$\hat{H}_e = \hat{H}^{LDA} + \hat{H}^{U} - \hat{H}^{DC}. \tag{3.2}$$

Here, $\hat{H}^{LDA}$ is the Kohn-Sham Hamiltonian, $\hat{H}^{U}$ the Coulomb term, and $\hat{H}^{DC}$ the double-counting correction. The LDA part of Hamiltonian (3.2) is given by

$$\hat{H}^{LDA} = -\sum_{ii'}\sum_{\alpha\alpha'} t^{i,i'}_{\alpha,\alpha'}\hat{c}^{\dagger}_{i\alpha}\hat{c}_{i'\alpha'}, \tag{3.3}$$

where $\hat{c}^{\dagger}_{i\alpha}$ ($\hat{c}_{i\alpha}$) creates (annihilates) an electron with flavor α at site i and $t^{i,i'}_{\alpha,\alpha'}$ reads as

$$t^{i,i'}_{\alpha,\alpha'} = -\int d\mathbf{r}\, \psi^{*}_{i\alpha}(\mathbf{r})\left[-\frac{1}{2}\nabla^{2}_{\mathbf{r}} + \upsilon_s(\mathbf{r})\right]\psi_{i'\alpha'}(\mathbf{r}). \tag{3.4}$$

The on-site (i=i') terms of Eq. (3.4) give the crystal-field matrix and $i\neq i'$ are the hopping integrals. Instead, the Coulomb term in Eq. (3.2) is expressed as

$$\begin{aligned} \hat{H}^{U} &= \frac{1}{2}\sum_{\substack{ii'\\ \tilde{i}\tilde{i}'}}\sum_{\substack{\alpha\alpha'\\ \tilde{\alpha}\tilde{\alpha}'}} U^{ii'\tilde{i}\tilde{i}'}_{\alpha\alpha'\tilde{\alpha}\tilde{\alpha}'}\hat{c}^{\dagger}_{i\alpha}\hat{c}^{\dagger}_{i'\alpha'}\hat{c}_{\tilde{i}'\tilde{\alpha}'}\hat{c}_{\tilde{i}\tilde{\alpha}}, \qquad (3.5)\\ U^{ii'\tilde{i}\tilde{i}'}_{\alpha\alpha'\tilde{\alpha}\tilde{\alpha}'} &= \int d\mathbf{r}\int d\mathbf{r}'\, \psi^{*}_{i\alpha}(\mathbf{r})\psi^{*}_{i'\alpha'}(\mathbf{r}')\frac{1}{|\mathbf{r}-\mathbf{r}'|}\psi_{\tilde{i}'\tilde{\alpha}'}(\mathbf{r}')\psi_{\tilde{i}\tilde{\alpha}}(\mathbf{r}). \end{aligned}$$

The electrons can be divided into two different types, strongly- and weakly-correlated. For the weakly-correlated electrons, $\hat{H}^{LDA}$ is sufficiently accurate alone. However, for the strongly-correlated electrons, LDA fails and $\hat{H}^{U} - \hat{H}^{DC}$ has to be taken into account explicitly. Downfolding uncorrelated electrons, however, renormalizes the Coulomb integrals in the correlated electrons sector. In this case, the Coulomb integrals cannot be calculated directly from Eq. (3.5). Approximate procedures to this end are the constrained LDA (cLDA) [10] and the constrained random-phase approximation (cRPA) [11]. Finally, $\hat{H}^{DC}$ cancels the contributions of the electron-electron interaction already included in the LDA, i.e., the long-range Hartree and the mean-field exchange-correlation interactions. Thus, the $\hat{H}^{U} - \hat{H}^{DC}$ term is a short-range many-body correction to the LDA and thus is nearly local. In general,

Hamiltonian (3.5) describes a system with inter- and on-site (local) Coulomb interactions. In the first approximation, we can assume that $\hat{H}^U - \hat{H}^{DC}$ is local and the correlated electrons belong to a single shell with quantum number nl, for example the $3d$ shell of transition metal ions. Thus, the Hamiltonian can be written as

$$\begin{aligned} \hat{H}_e &= \hat{H}^{LDA} + \hat{H}^U_{loc} - \hat{H}^{DC}_{loc}, \\ \hat{H}^U_{loc} - \hat{H}^{DC}_{loc} &= \frac{1}{2}\sum_i \sum_{\substack{mm' \\ \tilde{m}\tilde{m}'}} \sum_{\sigma\sigma'} U^i_{mm'\tilde{m}\tilde{m}'} \hat{c}^\dagger_{im\sigma} \hat{c}^\dagger_{im'\sigma'} \hat{c}_{i\tilde{m}'\sigma'} \hat{c}_{i\tilde{m}\sigma}, \\ m, m', \tilde{m}, \tilde{m}' &\in nl \text{ shell}. \end{aligned} \tag{3.6}$$

To ensure that the Coulomb interaction is as short-ranged as possible, it is important to use a localized basis. Among the successful methods for constructing the localized Wannier functions one can name the *ab initio* downfolding procedure based on the NMTO approach [12] and the maximally-localized Wannier functions algorithm of Marzari and Vanderbilt [13].

3.2 One-band Hubbard model

The minimal model for studying the physics of narrow band system is the Hubbard model

$$\hat{H} = \varepsilon_d \sum_{i\sigma} \hat{c}^\dagger_{i\sigma} \hat{c}_{i\sigma} - t \sum_{\substack{\langle ii' \rangle \\ \sigma}} \hat{c}^\dagger_{i\sigma} \hat{c}_{i'\sigma} + U \sum_i \hat{n}_{i\uparrow} \hat{n}_{i\downarrow}. \tag{3.7}$$

Here, the operator $\hat{n}_{i\sigma}{=}\hat{c}^\dagger_{i\sigma}\hat{c}_{i\sigma}$ counts the number of electrons with spin σ at site i, ε_d is the on-site energy and t is the hopping integral between the first-nearest neighbors $\langle ii' \rangle$. Furthermore, U denotes the strength of the on-site repulsion. The one-band Hubbard model is a simplified version of Hamiltonian (3.6), with $m{=}m'{=}\tilde{m}{=}\tilde{m}'{=}1$ and $\varepsilon_d{=}-t^{i,i}_{1,1}$, $t{=}t^{\langle i,i' \rangle}_{1,1}$, $U{=}U^{iiii}_{1111}$. In the non-interacting limit ($U{=}0$), Hamiltonian (3.7) describes a system of independent electrons

$$\hat{H}_0 = \varepsilon_d \sum_{i\sigma} \hat{c}^\dagger_{i\sigma} \hat{c}_{i\sigma} - t \sum_{\substack{\langle ii' \rangle \\ \sigma}} \hat{c}^\dagger_{i\sigma} \hat{c}_{i'\sigma}. \tag{3.8}$$

The Hamiltonian (3.8) is diagonal in the Bloch basis

$$\hat{H}_0 = \sum_{\mathbf{k}\sigma} \left[\varepsilon_d + \varepsilon_{\mathbf{k}}\right] \hat{c}^{\dagger}_{\mathbf{k}\sigma} \hat{c}_{\mathbf{k}\sigma}, \tag{3.9}$$

where the energy dispersion, $\varepsilon_{\mathbf{k}}$, depends on the geometry and the dimension of the lattice. For a hypercubic lattice of dimension d, $\varepsilon_{\mathbf{k}}$ is given by

$$\varepsilon_{\mathbf{k}} = -2t \sum_{\nu=1}^{\mathsf{d}} \cos(k_{r_\nu} a),$$

where a is the lattice constant and for d=3, r_1=x, r_2=y, and r_3=z.
In the opposite limit (t=0), the atomic limit, the Hubbard model describes a collection of isolated atoms, where the Hamiltonian of a single atom is

$$\hat{H}_i^{atom} = \varepsilon_d \sum_{\sigma} \hat{n}_{i\sigma} + U \hat{n}_{i\uparrow} \hat{n}_{i\downarrow}.$$

In the large U/t limit and at sufficient low energy, the Hubbard Hamiltonian for arbitrary filling is equivalent to the t-J model. At half-filling, N_{site}=N_e, where N_{site} is the number of sites, the t-J model becomes the Heisenberg model,

$$\hat{H}_{spin} = \frac{1}{2} J \sum_{\langle ii' \rangle} \left(\hat{\mathbf{S}}_i \cdot \hat{\mathbf{S}}_{i'} - \frac{1}{4} \hat{n}_i \hat{n}_{i'} \right). \tag{3.10}$$

Here, J=$\frac{4t^2}{U}$ is the strength of the antiferromagnetic exchange interaction that couples the spin in the neighboring sites and $\hat{\mathbf{S}}_i$=$(\hat{S}_i^x, \hat{S}_i^y, \hat{S}_i^z)$ [14].

3.3 DMFT for the one-band Hubbard model

To explain how DMFT works, we apply it to the one-band Hubbard model. Although the one-band Hubbard Hamiltonian, Eq. (3.7), is simpler than the original model, Eq. (3.6), it has no exact solution except in some special cases [15]. Before 1989, a wide variety of numerical and analytical methods were used to study it, but none of them could explain convincingly the paramagnetic insulator phase. This changed with the development of DMFT. In 1989, Metzner and Vollhardt showed that in the limit of infinite coordination number, the perturbation series strongly simplified [16]. Next,

Georges and Kotliar illustrated that the Hubbard model could be mapped onto a self-consistent quantum-impurity model in the local self-energy approximation [17]. This approach could be used to describe the paramagnetic metal-insulator transition. DMFT is exact for U=0 (the band limit), for t=0 (the atomic limit), and in the limit of infinite coordination number.
The local self-energy approximation is exact as the coordination number, $\mathcal{Z}$, becomes infinite. To show this, one rescales first the hopping amplitude as follows:

$$t = \frac{t^*}{\sqrt{\mathcal{Z}}}.$$

Taking this rescaling into account, one can show that the self-energy is purely local [18]:

$$\lim_{\mathcal{Z}\to\infty} \Sigma(\mathbf{k}, i\nu_n) = \Sigma(i\nu_n),$$

where ν_n is known as Matsubara frequency and defined as $\nu_n = \frac{(2n+1)\pi}{\beta}$, $n \in \mathbb{Z}$. The Matsubara frequencies are temperature-dependent through $\beta = 1/k_B T$. In this situation, the lattice Green function[1] is given by

$$G(\mathbf{k}, i\nu_n) = \left[i\nu_n - \varepsilon_{\mathbf{k}} - \hat{H}^{DC}_{loc} - \Sigma(i\nu_n) \right]^{-1}. \tag{3.11}$$

Then the local Green function is obtained as

$$G(i\nu_n) = \frac{1}{N_{\mathbf{k}}} \sum_{\mathbf{k}} G(\mathbf{k}, i\nu_n). \tag{3.12}$$

The first step of DMFT is to map the Hubbard model into an effective quantum-impurity model, such as the Anderson Hamiltonian

$$\begin{aligned}
\hat{H}_A &= \hat{H}_{bath} + \hat{H}_{hyb} + \hat{H}_{imp}, \qquad (3.13)\\
\hat{H}_{bath} &= -\sum_{\langle ii' \rangle} \sum_{\sigma} t_{i,i'} \hat{c}^{\dagger}_{i\sigma} \hat{c}_{i'\sigma},\\
\hat{H}_{hyb} &= \sum_{i\sigma} \left(V_i \hat{c}^{\dagger}_{i\sigma} \hat{d}_{\sigma} + V_i^* \hat{d}^{\dagger}_{\sigma} \hat{c}_{i\sigma} \right),\\
\hat{H}_{imp} &= U \hat{n}_{d\uparrow} \hat{n}_{d\downarrow} + \varepsilon_d \left(\hat{n}_{d\uparrow} + \hat{n}_{d\downarrow} \right).
\end{aligned}$$

The first term in Hamiltonian (3.13) describes the non-interacting electrons with hopping amplitude $t_{i,i'}$. The operator $\hat{c}^{\dagger}_{i\sigma}$ ($\hat{c}_{i\sigma}$) creates (annihilates) an

[1] Details on Green function are given in chapter 5.

electron with spin σ on the site i in the bath, $\hat{d}^{\dagger}_{\sigma}$ ($\hat{d}_{\sigma}$) creates (annihilates) an electron with spin σ on the impurity site, $\hat{n}_{d\sigma}=\hat{d}^{\dagger}_{\sigma}\hat{d}_{\sigma}$ and ε_d represent the number of electrons and the on-site energy of the electrons on the impurity site, respectively. The bath electrons hop into the impurity site with probability amplitude V_i, called hybridization. Unlike the Hubbard model, Hamiltonian (3.13) can be solved numerically via, e.g., exact diagonalization (ED) [19], the numerical renormalization group (NRG) [20], and the quantum Monte Carlo (QMC) methods [21]. By solving the quantum-impurity model, the impurity Green function, $G_{d,d}(i\nu_n)$, is obtained. The impurity Green function and the impurity self-energy, $\Sigma_A(i\nu_n)$, are related by the Dyson equation,

$$\begin{aligned} \mathcal{G}^0(i\nu_n) &= \left[G_{d,d}(i\nu_n)^{-1} + \Sigma_A(i\nu_n)\right]^{-1}, \\ \mathcal{G}^0(i\nu_n) &= \left[i\nu_n - \varepsilon_d - \Delta(i\nu_n)\right]^{-1}, \\ \Delta(i\nu_n) &= \frac{1}{N_{\mathbf{k}}}\sum_{\mathbf{k}}\frac{|V_{\mathbf{k}}|^2}{i\nu_n - \varepsilon_{\mathbf{k}}}, \end{aligned} \tag{3.14}$$

where $\mathcal{G}^0(i\nu_n)$ is the bath Green function, and $V_{\mathbf{k}}$ is the Fourier transform of hybridization amplitude. In the next step, we adopt the local self-energy approximation, i.e., we assume that the self-energy of the Hubbard model is equal to the local self-energy of the quantum-impurity model. Thus

$$G\left(i\nu_n\right) = \frac{1}{N_{\mathbf{k}}}\sum_{\mathbf{k}} G_{\mathbf{k}} \approx \frac{1}{N_{\mathbf{k}}}\sum_{\mathbf{k}}\left[i\nu_n - \varepsilon_{\mathbf{k}} - \hat{H}^{DC}_{loc} - \Sigma_A(i\nu_n)\right]^{-1}. \tag{3.15}$$

We use the Dyson equation once more to calculate the new bath Green function, which gives a new quantum-impurity model. This procedure is repeated, until the self-energy does not change any more. The DMFT loop can be summarized by these steps

1. Start with an input for the self-energy, $\Sigma(i\nu_n)$.
2. Use Eqs. (3.11) and (3.12) to construct the local lattice Green function.
3. Calculate the bath Green function from the Dyson equation; since the lattice system is mapped onto the quantum-impurity system, calculating the bath Green function, $\mathcal{G}^0\left(i\nu_n\right)$, from the lattice Green function, $G\left(i\nu_n\right)$, is consistent with the initial assumption,

$$\mathcal{G}^0\left(i\nu_n\right) = \left[G^{\sigma}\left(i\nu_n\right)^{-1} + \Sigma(i\nu_n)\right]^{-1}.$$

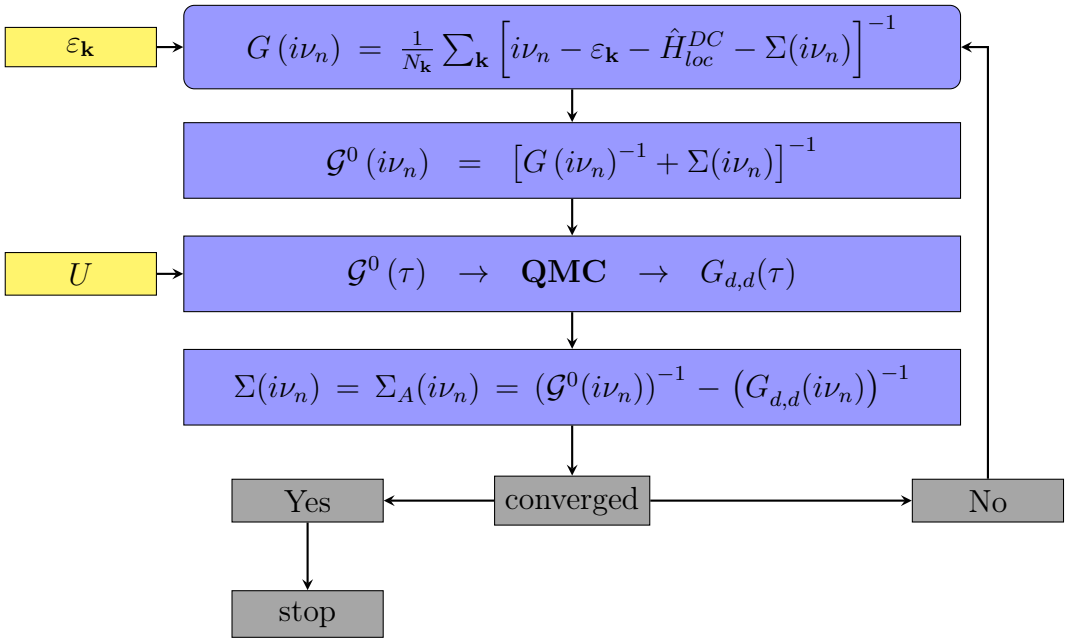


Figure 3.1: The DMFT self-consistency loop.

4. Solve the quantum-impurity model to obtain $G_{d,d}(i\nu_n)$, then calculate the local self-energy, $\Sigma_A(i\nu_n)$, from the Dyson equation, Eq. (3.14).

5. Apply the local self-energy approximation, $\Sigma(i\nu_n)$=$\Sigma_A(i\nu_n)$.

6. Repeat all steps starting from the second step with the new self-energy.

Iterations will be continued until the difference between the new self-energy and the self-energy of the previous iteration is smaller than a given error. In the self-consistency loop, in order to avoid oscillations, we use a mixing scheme. Commonly linear mixing is sufficient

$$\Sigma_{inp}^{(j+1)} = (1-\gamma)\Sigma_{inp}^{(j)} + \gamma\Sigma_{out}^{(j)}, \quad 0 < \gamma < 1$$

with $\Sigma_{inp(out)}^{j}$ as the input (output) of iteration j. Typically $\gamma\approx0.6$ is enough to reach convergence, but in some cases a smaller $\gamma\approx0.3$ is needed.

4

Quantum Monte Carlo solvers

4.1 Basic principles of Monte Carlo methods

The aim is to calculate integrals of the form

$$\langle O \rangle_P = \int_\Omega dx P(x) O(x), \tag{4.1}$$

where Ω is a discrete or continuous configuration space with elements x, and $P(x)$ is a probability distribution on this space,

$$\int_\Omega dx P(x) = 1 \quad \text{and} \quad P(x) \geq 0 \quad \forall \quad x \in \Omega. \tag{4.2}$$

When the configuration space, Ω, has high dimension, the most efficient way to calculate the sum over Ω is to use the Monte Carlo (MC) method. In the MC algorithm, the sum over all configuration space is obtained from sampling configurations. For a representative set of configurations, $\{x_i | i \in 1 \cdots M\}$, where M is the number of sample points, distributed according to the probability distribution $P(x)$, $\langle O \rangle_P$, is approximated as

$$\langle O \rangle_P \sim \frac{1}{M} \sum_{i=1}^{M} O(x_i) = X. \tag{4.3}$$

An important point is the distribution of X, $\mathcal{P}(X)$. If $O(x_1) \cdots O(x_M)$ are statistically independent and M large enough,

$$\mathcal{P}(X) = \frac{1}{\sqrt{2\pi}} \frac{1}{\sigma} \exp\left[-\frac{(X - \langle O \rangle_P)^2}{2\sigma^2} \right], \; \sigma^2 = \frac{1}{M} \left(\langle O^2 \rangle_P - \langle O \rangle_P^2 \right). \tag{4.4}$$

Thus, the statistical error scales as $1/\sqrt{M}$. In order to generate the configuration x_i according to the probability $P(x)$, a very successful way consists in using the Metropolis-Hastings algorithm. The configuration space is sampled by a Markov chain. To define the Markov process, we introduce a transition matrix, $T_{y,x}$, which corresponds to the transition probability from configuration x to configuration y. The Markov chain has to be ergodic, which means any configuration should be reachable from any other one within a finite number of Markov steps. Furthermore $P(x)$ should be a stationary point

$$\sum_x T_{y,x} P(x) = P(y).$$

This can be achieved if the *detailed balance condition*,

$$T_{y,x} P(x) = T_{x,y} P(y),$$

is satisfied. Splitting the transition probability from configuration x to y into a proposal probability, $T^{prop}_{y,x}$, and an acceptance probability, $T^{acc}_{y,x}$,

$$T_{y,x} = T^{prop}_{y,x} T^{acc}_{y,x},$$

one can see that the Metropolis-Hastings definition

$$T^{acc}_{y,x} = min\left\{1, \frac{P(y) T^{prop}_{x,y}}{P(x) T^{prop}_{y,x}}\right\},$$

satisfies the detailed balance condition. In practical implementations, the new configuration, y, is accepted if $u \leq T^{acc}_{y,x}$, where u is a random number in $u \in [0, 1)$. This procedure is repeated M times, until the error is below the desired accuracy [22].

4.2 Continuous-time quantum Monte Carlo

In the DMFT simulation, the most computationally expensive step is solving the quantum-impurity problem. The most flexible solvers so far are all based on QMC algorithms. In this section, we briefly discuss continuous-time quantum Monte Carlo (CT-QMC) method. Before we enter into details, we point out that there is a price to the flexibility of the CT-QMC methods. First, the computational time scales as $(N_{imp}\beta)^{\zeta}$, where N_{imp} is the number

of impurities and ζ is typically (depending on the specific of the algorithm) larger than one. Thus, it is important to restrict the calculation to the essential degrees of freedom, furthermore exploiting symmetries and using the power of massively parallel supercomputers can reduce the actual computational time. Second, for fermionic systems, QMC methods may suffer from the so-called "sign" problem; when this happens the calculations cannot be performed.
There are several flavors of CT-QMC [23–26]. Here, we briefly introduce the interaction-expansion approach (CT-INT). We explain it for the case of a one-band Anderson model. The first step consists in splitting Hamiltonian (3.13) in two parts, the non-interacting part, $\hat{H}_0$=$\hat{H}_{bath}+\hat{H}_{hyb}$ and the interacting part, $\hat{H}_U$=$\hat{H}_{imp}$; $\hat{H}$=$\hat{H}_0+\hat{H}_U$. In addition, we introduce the operator

$$\hat{U}(\beta) = \mathrm{e}^{\beta\hat{H}_0}\mathrm{e}^{-\beta\hat{H}}.$$

Next, we write the partition function in terms of $\hat{U}$ operator

$$Z = \mathrm{Tr}\left[\mathrm{e}^{-\beta\hat{H}}\right] = \mathrm{Tr}\left[\mathrm{e}^{-\beta\hat{H}_0}\hat{U}\left(\beta\right)\right]. \tag{4.5}$$

The operator $\hat{U}(\beta)$ satisfies the following differential equation

$$\frac{d\hat{U}(\beta)}{d\beta} = -\hat{H}_U(\beta)\hat{U}(\beta) \Longrightarrow \hat{U}(\beta) = \hat{T}_\tau \mathrm{exp}\left(-\int_0^\beta d\tau\, \hat{H}_U(\tau)\right), \tag{4.6}$$

where $\hat{T}_\tau$ is the time-ordering operator, which orders the operators according to the value of the argument τ, with the smallest one on the right. Replacing Eq. (4.6) into (4.5) gives the final expression for the partition function

$$\begin{aligned} Z &= \mathrm{Tr}\left[\mathrm{e}^{-\beta\hat{H}_0}\hat{T}_\tau \mathrm{e}^{-\int_0^\beta d\tau\, \hat{H}_U(\tau)}\right], \\ &= Z_0 \left\langle \mathrm{e}^{-\int_0^\beta d\tau\, \hat{H}_U(\tau)} \right\rangle_0, \\ Z_0 &= \mathrm{Tr}\left[\mathrm{e}^{-\beta\hat{H}_0}\right]. \end{aligned} \tag{4.7}$$

Here, the expectation value $\langle\bullet\rangle_0$ is taken with respect to the non-interacting single-impurity Anderson model with partition function Z_0. Now we can use the Taylor expansion to expand the exponential function in Eq. (4.7) in terms of the Hubbard interaction as follows:

$$\frac{Z}{Z_0} = \sum_{n=0}^{\infty} \frac{(-U)^n}{n!} \int_0^\beta d\tau_1 \cdots \int_0^\beta d\tau_n \, \langle \hat{n}_\uparrow(\tau_1)\hat{n}_\downarrow(\tau_1)\cdots\hat{n}_\uparrow(\tau_n)\hat{n}_\downarrow(\tau_n)\rangle_0 . \tag{4.8}$$

In order to reduce the sign problem, it turns out that it is useful to replace $\hat{H}_U$ with

$$\hat{H}_U \to \hat{\tilde{H}}_U = \frac{U}{2} \sum_{s=\pm 1} \left(\hat{n}_\uparrow - \frac{\rho}{2} - s\delta \right) \left(\hat{n}_\downarrow - \frac{\rho}{2} + s\delta \right), \tag{4.9}$$

where s is an additional Ising variable, ρ corresponds to the average electron density and δ is a small positive parameter. This gives

$$\begin{aligned} \frac{Z}{Z_0} &= \sum_{n=0}^{\infty} \left(\frac{-U}{2} \right)^n \frac{1}{n!} \int_0^\beta d\tau_1 \sum_{s_1} \cdots \int_0^\beta d\tau_n \\ &\times \left(\sum_{s_n} \prod_\sigma \langle [n_\sigma(\tau_1) - \alpha_\sigma(s_1)] \, ... \, [n_\sigma(\tau_n) - \alpha_\sigma(s_n)] \rangle_0 \right). \end{aligned} \tag{4.10}$$

Here, we have used the short-cut notation

$$\alpha_\sigma(s) = \frac{\rho}{2} + \sigma s \delta.$$

Now we can applying the Wick theorem to the thermal expectation values in Eq. (4.10). Consequently, we obtain

$$\langle [n_\sigma(\tau_1) - \alpha_\sigma(s_1)] \cdots [n_\sigma(\tau_n) - \alpha_\sigma(s_n)] \rangle_0 = \det \mathbf{M}_\sigma(C_n), \tag{4.11}$$

where $\mathbf{M}_\sigma(C_n)$ is expressed as

$$\begin{pmatrix} g_0(\tau_1,\tau_1) - \alpha_\sigma(s_1) & g_0(\tau_1,\tau_2) & \cdots & g_0(\tau_1,\tau_n) \\ g_0(\tau_2,\tau_1) & g_0(\tau_2,\tau_2) - \alpha_\sigma(s_2) & \cdots & g_0(\tau_2,\tau_n) \\ \cdot & \cdot & \cdot & \cdot \\ \cdot & \cdot & \cdot & \cdot \\ \cdot & \cdot & \cdot & \cdot \\ g_0(\tau_n,\tau_1) & g_0(\tau_n,\tau_2) & \cdots & g_0(\tau_n,\tau_n) - \alpha_\sigma(s_n) \end{pmatrix}. \tag{4.12}$$

The entries of matrix $\mathbf{M}_\sigma(C_n)$ are the Green functions of the non-interacting system which are given by

$$g_0(\tau_1,\tau_2) = \left\langle \hat{T}_\tau \hat{d}^\dagger_\sigma(\tau_1) \hat{d}_\sigma(\tau_2) \right\rangle_0. \tag{4.13}$$

A configuration C_n of order n is defined as

$$C_n = \{ [\tau_1, s_1] \cdots [\tau_n, s_n] \}, \tag{4.14}$$

with the short-hand notation

$$\sum_{C_n} = \sum_{n=0}^{\infty} \int_0^\beta d\tau_1 \sum_{s_1} \cdots \int_0^\beta d\tau_n \sum_{s_n}. \tag{4.15}$$

Then the partition function can be written as

$$\begin{aligned} \frac{Z}{Z_0} &= \sum_{C_n} W(C_n), \\ W(C_n) &= \left(-\frac{U}{2}\right)^n \frac{1}{n!} \prod_\sigma \det \mathbf{M}_\sigma(C_n). \end{aligned} \tag{4.16}$$

Now observable $\hat{O}(\tau)$ can be obtained as

$$\left\langle \hat{O}(\tau) \right\rangle = \frac{\sum_{C_n} W(C_n) \left\langle \left\langle \hat{O}(\tau) \right\rangle \right\rangle_{C_n}}{\sum_{C_n} W(C_n)}, \tag{4.17}$$

where for $\hat{O}(\tau) = \prod_\sigma \hat{O}_\sigma(\tau)$, the quantity $\left\langle \left\langle \hat{O}(\tau) \right\rangle \right\rangle_{C_n}$ in the nominator is expressed by

$$\left\langle \left\langle \hat{O}(\tau) \right\rangle \right\rangle_{C_n} = \frac{\prod_\sigma \left\langle \hat{T}_\tau \left[\hat{n}_\sigma(\tau_1) - \alpha_\sigma(s_1)\right] \ldots \left[\hat{n}_\sigma(\tau_n) - \alpha_\sigma(s_n)\right] \hat{O}_\sigma(\tau) \right\rangle_0}{\prod_\sigma \left\langle \hat{T}_\tau \left[\hat{n}_\sigma(\tau_1) - \alpha_\sigma(s_1)\right] \ldots \left[\hat{n}_\sigma(\tau_n) - \alpha_\sigma(s_n)\right] \right\rangle_0}. \tag{4.18}$$

The aim of using the QMC solver in the DMFT self-consistency loop is calculating the single-particle Green function of the impurity in the Anderson Hamiltonian, Eq. (3.13),

$$G_\sigma^{d,d}(\tau - \tau') = \left\langle \hat{T}_\tau \hat{d}_\sigma^\dagger(\tau) \hat{d}_\sigma(\tau') \right\rangle. \tag{4.19}$$

From the determinant identity in Eq. (4.11), the single-particle Green function in configuration C_n is given by the ratio of two determinants

$$\left\langle \left\langle \hat{T}_\tau \hat{d}_\sigma^\dagger(\tau) \hat{d}_\sigma(\tau') \right\rangle \right\rangle_{C_n} = \frac{\det B_\sigma(C_n)}{\det \mathbf{M}_\sigma(C_n)}, \tag{4.20}$$

where

$$B_\sigma(C_n) = \begin{pmatrix} & & & g_0(\tau_1,\tau') \\ & \mathbf{M}_\sigma(C_n) & & \cdot \\ & & & \cdot \\ & & & \cdot \\ & & & g_0(\tau_n,\tau') \\ g_0(\tau,\tau_1) & \cdot \quad \cdot \quad \cdot & g_0(\tau,\tau_n) & g_0(\tau_n,\tau') \end{pmatrix}. \tag{4.21}$$

Using the appropriate determinant identities we can obtain

$$\begin{aligned} g(\tau,\tau')_{C_n} &= \left\langle\left\langle \hat{T}_\tau \hat{d}^\dagger_\sigma(\tau)\hat{d}_\sigma(\tau')\right\rangle\right\rangle_{C_n} \\ &= g_0(\tau,\tau') - \sum_{r,s=1}^{n} g_0(\tau,\tau_r)\left(\mathbf{M}_\sigma(C_n)^{-1}\right)_{r,s} g_0(\tau_s,\tau'). \end{aligned} \tag{4.22}$$

Replacing Eq. (4.22) into (4.17) gives the final expression for $G^{d,d}_\sigma(\tau-\tau')$. A prerequisite for MC implementation is that the weight, $W(C_n)$ in Eq. (4.17) is positive. For quantum systems, the quantity used as "probability" is not always positive. However, one can still use MC sampling using the absolute value $|W(C_n)|$. Then, we will carry out the MC calculation with

$$\begin{aligned} \left\langle \hat{O}(\tau)\right\rangle &= \frac{\sum_{C_n} W(C_n)\left\langle\left\langle \hat{O}(\tau)\right\rangle\right\rangle_{C_n}}{\sum_{C_n} W(C_n)} \\ &= \frac{\sum_{C_n} |W(C_n)|\,\mathrm{sign}(W(C_n))\left\langle\left\langle \hat{O}(\tau)\right\rangle\right\rangle_{C_n}}{\sum_{C_n} |W(C_n)|\,\mathrm{sign}(W(C_n))}. \end{aligned} \tag{4.23}$$

The sign problem occurs when the denominator of Eq. (4.23) becomes very small, i.e., the average sign goes to zero. One can show that average sign decays exponentially with the inverse temperature and the number of impurities, N_{imp},

$$\langle \mathrm{sign}\rangle \simeq \mathrm{e}^{-\Delta\beta N_{imp}}, \tag{4.24}$$

where the pre-factor Δ is formulation-dependent. There are some cases that are sign problem free. For example, a class of one-dimensional problems [27] with particle-hole symmetry formulated within CT-INT [28], or the single-impurity Anderson model [29].

5

Multi-orbital Hubbard Hamiltonian

In section (3.1), we introduced the general form of the multi-orbital Hubbard model. Here, we will discuss how to obtain the parameters of this model. Specifically, in this thesis we study single-layered perovskites. A representative system of this structure is Sr_2RuO_4, is shown in Fig. (5.1). The electronic configuration of the ruthenium atom, Ru, is $[\mathrm{Kr}]\, 4d^7\, 5s^1$. In Sr_2RuO_4, the nominal oxidation state of the ruthenium is Ru^{4+}; this leaves Ru in $4d^4$ configuration. It is located at the center of RuO_6 octahedron.

5.1 Coulomb interaction matrix

Here, we discuss how to obtain the elements of the electron-electron Coulomb interaction matrix in the local approximation, $U_{mm'\tilde{m}\tilde{m}'}$ matrix in Eq. (3.6). As it was mentioned before, $U_{mm'\tilde{m}\tilde{m}'}$ is the matrix element of the screened Coulomb interaction. However, the screened Coulomb interaction has the same form as the bare Coulomb interaction. We now derive the elements of the $U_{mm'\tilde{m}\tilde{m}'}$ matrix in the atomic orbitals basis. An electron is described by both the spatial coordinates, $\mathbf{r}$, and spin coordinate, σ. We denote its wave-function as $\varphi_{nlm}(\mathbf{r})\chi(\sigma)$. Then $U_{mm'\tilde{m}\tilde{m}'}$ in the basis of atomic orbitals can be expressed as

$$\begin{aligned} U_{mm'\tilde{m}\tilde{m}'} &= \delta_{\sigma\tilde{\sigma}}\delta_{\sigma'\tilde{\sigma}'} \\ &\times \int d\mathbf{r} \int d\mathbf{r}'\, \varphi^*_{nlm}(\mathbf{r})\varphi^*_{nlm'}(\mathbf{r}')\frac{1}{|\mathbf{r}-\mathbf{r}'|}\varphi_{nl\tilde{m}'}(\mathbf{r}')\varphi_{nl\tilde{m}}(\mathbf{r}). \end{aligned} \tag{5.1}$$

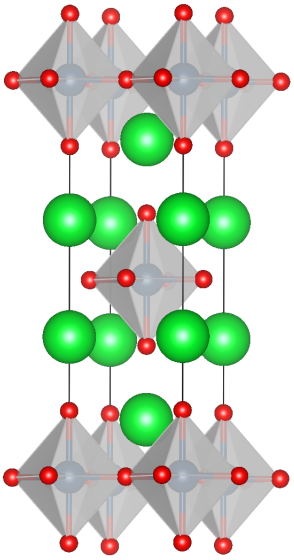


Figure 5.1: The conventional unit cell of Sr_2RuO_4. The blue spheres stand for the ruthenium, the green spheres for the strontium and the red ones for the oxygen ions. The space group is I4/mmm. The lattice constant are a=b=3.90 Å and c=12.68. Positions of atoms in the unit cell are given by Ru: $(0,0,0)$, Sr: $(\frac{1}{2},\frac{1}{2},0.85)$, O_1: $(0,\frac{1}{2},0)$, O_2: $(0,0,0.83)$. The structure is plotted using VESTA software.

The spin part is trivial, while the spatial component is rather complicated. If we parameterize the vector $\mathbf{r}$ by its spherical coordinates (r,θ,ϕ), the spatial part of the atomic orbital is given by

$$\varphi_{nlm}(\mathbf{r}) = R_{nl}(r)Y_{lm}(\theta,\phi).$$

Now we use the multipole expansion of the Coulomb interaction

$$\frac{1}{|\mathbf{r}-\mathbf{r}'|} = \sum_{k=0}^{\infty} \frac{r_<^k}{r_>^{k+1}} \frac{4\pi}{2k+1} \sum_{\mu=-k}^{k} Y^*_{k\mu}(\theta,\phi)Y_{k\mu}(\theta',\phi'), \tag{5.2}$$

where $r_<$= $\min(r_1,r_2)$ and $r_>$= $\max(r_1,r_2)$. For a specific shell with quantum numbers (n,l), Eq. (5.2) splits into radial and angular parts

$$\begin{aligned}\frac{1}{|\mathbf{r}-\mathbf{r}'|} &= \sum_{k=0}^{\infty} \underbrace{\langle R_{nl}R_{nl}|\frac{r_<^k}{r_>^{k+1}}|R_{nl}R_{nl}\rangle}_{\text{Radial part}} \\ &\times \frac{4\pi}{2k+1}\sum_{\mu=-k}^{k} \underbrace{\langle Y_{lm}|Y^*_{k\mu}|Y_{l\tilde{m}}\rangle\ \langle Y_{lm'}|Y_{k\mu}|Y_{l\tilde{m}'}\rangle}_{\text{Angular part}}.\end{aligned} \tag{5.3}$$

The radial part is a so-called Slater integral. This integral, which has the dimension of energy, controls the strength of the Coulomb repulsion interaction. The angular part consists of two Gaunt coefficients —a dimensionless integral over three spherical harmonics. The spherical harmonic function can be written as

$$Y_{lm}\left(\theta,\phi\right)=(-1)^{\frac{(m+|m|)}{2}}\left[\frac{2l+1}{4\pi}\frac{(l-|m|)\,!}{(l+|m|)\,!}\right]^{\frac{1}{2}}P_{l|m|}\left(\cos\theta\right)e^{im\phi},$$

where $P_{lm}(\theta)$ is the associated Legendre polynomials. Because of the ϕ-dependence of $Y_{lm}(\theta,\phi)$, the angular part of Eq. (5.3) is different from zero only if $m+m'{=}\tilde{m}+\tilde{m}'$. In the next step, we introduce the following short notations for the non-vanishing Gaunt coefficient and the Slater integral

$$\begin{aligned} c^{(k)}(m;\tilde{m}) &= \sqrt{\frac{4\pi}{2k+1}}\int_0^{2\pi}d\phi\int_{-1}^{1}d\cos(\theta) \\ &\times\ Y^*_{lm}(\theta,\phi)Y_{k,m-\tilde{m}}Y_{l,\tilde{m}}(\theta,\phi), \qquad (5.4)\\ F^{(k)} &= \int_0^{\infty}dr\,r^2\int_0^{\infty}dr'\,r'^2R^2_{nl}(r)\frac{r^k_<}{r^{k+1}_>}R^2_{nl}(r'). \qquad (5.5)\end{aligned}$$

Since the integrand in Eq. (5.5) is everywhere positive and $\frac{r^0_<}{r^1_>}>\frac{r^1_<}{r^2_>}>\frac{r^2_<}{r^3_>}>$ ..., it follows that

$$F^{(0)}>F^{(1)}>F^{(2)}>...>0.$$

Then the complete Coulomb matrix elements using the introduced notations are given by

$$U_{mm'\tilde{m}\tilde{m}'}=\delta_{\sigma\tilde{\sigma}}\delta_{\sigma'\tilde{\sigma}'}\delta_{m+m',\tilde{m}+\tilde{m}'}\sum_{k=0}^{\infty}c^{(k)}(m;\tilde{m})c^{(k)}(m';\tilde{m}')F^{(k)}, \qquad (5.6)$$

where the k index runs from 0 to infinity [30]. However, by applying the so-called *triangular condition* [31] for a shell with angular quantum number l, the k values reduce to $k{=}0,2,4,...,2l$. For the d shell with angular quantum number $l{=}2$, the Slater integral takes only three terms, $F^{(0)}, F^{(2)}$, and $F^{(4)}$. The most important Coulomb integrals are the two-index terms: The direct ($U_{mm'mm'}{\equiv}U_{mm'}$) and exchange ($U_{mm'm'm}{\equiv}J_{mm'}$) integrals, with $m{\neq}m'$. If

we write all possible two-index terms, the $\hat{H}_U$ is expressed as

$$\begin{aligned}\hat{H}^U &= \frac{1}{2}\sum_i \sum_{\substack{mm' \\ \sigma}} U_{mm'} \hat{n}_{im\sigma}\hat{n}_{im'-\sigma} + \frac{1}{2}\sum_i \sum_{\substack{m\neq m' \\ \sigma}} \left(U_{mm'} - J_{mm'}\right) \hat{n}_{im\sigma}\hat{n}_{im'\sigma} \\ &+ \sum_i \sum_{m\neq m'} J_{mm'} \left(\hat{c}^\dagger_{im\uparrow}\hat{c}^\dagger_{im\downarrow}\hat{c}_{im'\uparrow}\hat{c}_{im'\downarrow} + \hat{c}^\dagger_{im\uparrow}\hat{c}_{im\downarrow}\hat{c}^\dagger_{im'\downarrow}\hat{c}_{im'\uparrow}\right). \end{aligned} \tag{5.7}$$

The first two terms in Eq. (5.7) are the so-called density-density terms, and the last two terms are spin-flip and pair-hopping interactions, respectively. In practical calculations, it is useful to introduce the averaged quantities.

$$\begin{aligned}\tilde{U}_{avg} &= U_{avg} - J_{avg}, \\ \tilde{U}_{avg} &= \frac{1}{2l(2l+1)}\sum_{mm'}(U_{mm'} - J_{mm'}), \\ U_{avg} &= \frac{1}{(2l+1)^2}\sum_{mm'} U_{mm'}, \\ J_{avg} &= \frac{1}{2l(2l+1)}\sum_{mm'} J_{mm'} - \frac{1}{2l}U_{avg}. \end{aligned}$$

By expressing $U_{mm'}$ in terms of the Slater integral and Gaunt coefficient, U_{avg} is given by

$$\begin{aligned}U_{avg} &= \frac{1}{(2l+1)^2}\sum_{k=0}^{2l} F^{(k)} \frac{4\pi}{2k+1} \sum_{mm'}\sum_{\mu=-k}^{k} \langle lm|Y_{k\mu}|lm\rangle \left\langle lm'|Y^*_{k\mu}|lm'\right\rangle \\ &= \frac{1}{(2l+1)^2}\sum_{k=0}^{2l} F^{(k)} \frac{4\pi}{2k+1} \left(\sum_m \langle lm\,|Y_{k0}|\,lm\rangle\right)^2 \\ &= \frac{1}{(2l+1)^2}\sum_{k=0}^{2l} F^{(k)} \frac{4\pi}{2k+1} \left(\frac{(2l+1)^2}{4\pi}\delta_{k0}\right) = F^{(0)}. \end{aligned} \tag{5.8}$$

Similarly, we can show that J_{avg} is linear combinations of $F^{(k)}$:

$$\begin{aligned} J_{avg} &= \frac{1}{2l(2l+1)} \sum_{k=0}^{2l} F^{(k)} \frac{4\pi}{2k+1} \sum_{mm'} \sum_{\mu=-k}^{k} \langle lm|Y_{k\mu}|lm'\rangle \left\langle lm'|Y^*_{k\mu}|lm\right\rangle \\ &- \frac{1}{2l} F^{(0)} \\ &= \frac{1}{2l(2l+1)} \sum_{k=0}^{2l} F^{(k)} \frac{4\pi}{2k+1} \left(\sum_{mm'} \langle lm|Y_{k,m-m'}|lm'\rangle \right)^2 - \frac{1}{2l} F^{(0)} \\ &= \frac{1}{2l(2l+1)} \sum_{k=0}^{2l} \frac{4\pi}{2k+1} \left((2l+1) \sqrt{\frac{2k+1}{4\pi}} \langle l0|Y_{l0}|l0\rangle \right) - \frac{1}{2l} F^{(0)} \\ &= \frac{1}{2l} \sum_{k=0}^{2l} F^{(k)} \sqrt{\frac{4\pi}{2k+1}} \langle l0|Y_{k0}|l0\rangle - \frac{1}{2l} F^{(0)}. \end{aligned} \tag{5.9}$$

Since $\langle l0|Y_{00}|l0\rangle = Y_{00} \langle l0|l0\rangle = Y_{00} = \frac{1}{\sqrt{4\pi}}$, $F^{(0)}$ vanishes in Eq. (5.9). Then J_{avg} can be written in terms of $F^{(2)}, F^{(4)}, ..., F^{(k)}$ and Gaunt coefficients of the form $\langle l0|Y_{k0}|l0\rangle$. As an example, for the d shell by inserting the value of $\langle l0|Y_{k0}|l0\rangle$, we can show that $J_{avg} = \frac{1}{14} F^{(2)} + \frac{1}{14} F^{(4)}$.

5.2 Crystal-field matrix

For an isolated atom the Coulomb potential between electron and nucleus, $\upsilon_s(\mathbf{r})$, has the spherical symmetry which leads to $(2l+1)$ degenerate states for the shell with angular quantum number l. However, in a solid or a molecule the Coulomb potential generated by the surrounding ions applies lower symmetry which can lift the degeneracy of electronic states. Let us assume that the crystal is ionic, and neglect $\upsilon_H(\mathbf{r})$ and $\upsilon_{xc}(\mathbf{r})$ in Eq. (2.8). Then the one-electron potential can be written as

$$\begin{aligned} \upsilon_s(\mathbf{r}) &= \sum_i \frac{Q_i}{|\mathbf{R}_i - \mathbf{r}|} = \frac{Q_0}{|\mathbf{R}_0 - \mathbf{r}|} + \sum_{i \neq 0} \frac{Q_i}{|\mathbf{R}_i - \mathbf{r}|}, \\ &= \upsilon_0(\mathbf{r}) + \upsilon_c(\mathbf{r}), \end{aligned} \tag{5.10}$$

where $\mathbf{r}$ is the electron coordinate and $\mathbf{R}_i$ and Q_i is the position vector and charge of the ith point-charge, respectively. The first term, $\upsilon_0(\mathbf{r})$, is the

ionic potential and the second term, $\upsilon_c(\mathbf{r})$, is the electrostatic potential at $\mathbf{r}$, generated by all the surrounding ions in the crystal which is called *crystal-field potential*. Let us consider the cubic perovskite system, with structure ABC_3. We want to calculate the crystal-field potential at the site of the transition metal, B ion. If we only consider the first-nearest neighbors, the relevant C ions are those located at positions $(\pm a, 0, 0)$, $(0, \pm a, 0)$, $(0, 0, \pm a)$, where a is the lattice constant. For this purpose, it is convenient to use the multipole expansion for the Coulomb potential, Eq. (5.2). Then, $\upsilon_c(\mathbf{r})$ at the position of the B ion, for the angular quantum number l=2, can be written as

$$\upsilon_c^{\text{cub}}(\mathbf{r}) = \sum_{k=0}^{4} \sum_{\mu=-4}^{4} r^k q_{k\mu} C_\mu^{(k)}(\theta, \phi), \tag{5.11}$$

$$q_{k\mu} = \sqrt{\frac{4\pi}{2k+1}} \frac{Q}{a^{k+1}} \sum_{i=1}^{6} Y_{k\mu}^*(\theta_i, \phi_i), \tag{5.12}$$

$$C_\mu^{(k)}(\theta, \phi) = \sqrt{\frac{4\pi}{2k+1}} Y_{k\mu}(\theta, \phi), \tag{5.13}$$

where (r, θ, ϕ) and (a, θ_i, ϕ_i) are the spherical coordinates of $\mathbf{r}$ and $\mathbf{R}_i$, respectively. Hence, (θ_1, ϕ_1), (θ_2, ϕ_2), ... are known to be

$$(\frac{\pi}{2}, 0),\ (\frac{\pi}{2}, \frac{\pi}{2}),\ (\frac{\pi}{2}, \pi),\ (\frac{\pi}{2}, \frac{3\pi}{2}),\ (0, 0),\ (\pi, 0).$$

After calculating the $q_{k\mu}$ coefficient for each of (θ_i, ϕ_i), we obtain

$$\upsilon_c^{\text{cub}}(\mathbf{r}) = \frac{6Q}{a} + \frac{7Q}{2a^5} r^4 \left[C_0^{(4)}(\theta, \phi) + \sqrt{\frac{5}{14}} \left[C_4^{(4)}(\theta, \phi) + C_{-4}^{(4)}(\theta, \phi) \right] \right]. \tag{5.14}$$

The first term is independent of the electron coordinate which just shifts the origin of the energy by $\frac{6Q}{a}$. We introduce a new quantity, $\tilde{\upsilon}_c^{\text{cub}}(\mathbf{r})$, which is defined by $\tilde{\upsilon}_c^{\text{cub}}(\mathbf{r}) = \upsilon_c^{\text{cub}}(\mathbf{r}) - \frac{6Q}{a}$. Then, the matrix elements of $\tilde{\upsilon}_c^{\text{cub}}(\mathbf{r})$ in the basis of atomic orbitals with quantum numbers $(n2m)$ and $(n2m')$ is given by

$$\left\langle \varphi_{n2m} \left| \tilde{\upsilon}_c^{\text{cub}}(\mathbf{r}) \right| \varphi_{n2m'} \right\rangle = \int d\mathbf{r}\, \varphi_{n2m}^*(\mathbf{r}) \tilde{\upsilon}_c^{\text{cub}}(\mathbf{r}) \varphi_{n2m'}(\mathbf{r}). \tag{5.15}$$

The non-vanishing matrix elements are given as follows:

$$\begin{aligned}
\left\langle \varphi_{n20} \left| \tilde{v}_c^{\mathrm{cub}}(\mathbf{r}) \right| \varphi_{n20} \right\rangle &= 6Dq, \\
\left\langle \varphi_{n2\pm2} \left| \tilde{v}_c^{\mathrm{cub}}(\mathbf{r}) \right| \varphi_{n2\pm2} \right\rangle &= Dq, \\
\left\langle \varphi_{n2\pm1} \left| \tilde{v}_c^{\mathrm{cub}}(\mathbf{r}) \right| \varphi_{n2\pm1} \right\rangle &= -4Dq, \\
\left\langle \varphi_{n2\pm2} \left| \tilde{v}_c^{\mathrm{cub}}(\mathbf{r}) \right| \varphi_{n2\mp2} \right\rangle &= 5Dq,
\end{aligned} \tag{5.16}$$

where $D{=}\frac{35Q}{4a^5}$, $q{=}\left(\frac{2}{105}\right)\langle r^4\rangle_{n2}$ and $\langle r^m\rangle_{n2}{=}\int dr\, r^{2+m}|R_{n2}(r)|^2$. Then the correspondent secular equation is expressed by

$$\begin{vmatrix}
\epsilon^0+Dq-\epsilon & 0 & 0 & 0 & 5Dq \\
0 & \epsilon^0-4Dq-\epsilon & 0 & 0 & 0 \\
0 & 0 & \epsilon^0-6Dq-\epsilon & 0 & 0 \\
0 & 0 & 0 & \epsilon^0-4Dq-\epsilon & 0 \\
\epsilon^0+5Dq-\epsilon & 0 & 0 & 0 & \epsilon^0+Dq+\epsilon
\end{vmatrix} = 0, \tag{5.17}$$

where $\epsilon^0{=}\epsilon_3+\frac{6Q}{a}$, and ϵ_3 is the energy of the $3d$-states of the hydrogen atom. The bases of the secular matrix for (5.17) are arranged in the order, $m{=}2,1,0,-1,-2$. Solving this equation, we can conclude that the d-levels of the transition metal, which has five-fold degeneracy, are split into doubly and triply degenerate levels. The wave-functions associated with doubly and triply degenerate states are called e_g- and t_{2g}-states, respectively. The associated wave-functions with the split levels are as follows:

$$e_g \longrightarrow \quad \left\{ \varphi_{n20},\ \frac{1}{\sqrt{2}}\left(\varphi_{n22}+\varphi_{n2-2}\right) \right\}, \tag{5.18}$$

$$t_{2g} \longrightarrow \quad \left\{ \varphi_{n21},\ \varphi_{n2-1},\ \frac{1}{\sqrt{2}}\left(\varphi_{n22}-\varphi_{n2-2}\right) \right\}. \tag{5.19}$$

The magnitude of the splitting between the e_g- and t_{2g}-states is given by

$$\Delta = \epsilon(e_g) - \epsilon(t_{2g}){=}10Dq.$$

The wave-functions in Eqs. (5.18) and (5.19) are not real, but can be made real by applying a unitary transformation within each degenerate subspace. Let us define the unitary transformation as

$$\varphi_\gamma = \sum_i \varphi_i U_{i\gamma}, \tag{5.20}$$

where for t_{2g}-subspace φ_i are

$$\varphi_1{=}\varphi_{n21}, \quad \varphi_2{=}\varphi_{n2-1}, \quad \varphi_3{=}\frac{1}{\sqrt{2}}(\varphi_{n22}-\varphi_{n2-2}).$$

By using the unitary transformation matrix,

$$U=\begin{pmatrix} \frac{i}{\sqrt{2}} & \frac{-1}{\sqrt{2}} & 0 \\ \frac{i}{\sqrt{2}} & \frac{1}{\sqrt{2}} & 0 \\ 0 & 0 & -i \end{pmatrix}, \tag{5.21}$$

the real functions for the t_{2g}-states are obtained as follows:

$$\begin{aligned}
\varphi_\xi &= \frac{i}{\sqrt{2}}\left(\varphi_{n21}+\varphi_{n2-1}\right)=\sqrt{\frac{15}{4\pi}}\left(\frac{yz}{r^2}\right)R_{n2}(r),\\
\varphi_\eta &= \frac{-1}{\sqrt{2}}\left(\varphi_{n21}-\varphi_{n2-1}\right)=\sqrt{\frac{15}{4\pi}}\left(\frac{xz}{r^2}\right)R_{n2}(r),\\
\varphi_\zeta &= \frac{-i}{\sqrt{2}}\left(\varphi_{n22}-\varphi_{n2-2}\right)=\sqrt{\frac{15}{4\pi}}\left(\frac{xy}{r^2}\right)R_{n2}(r).
\end{aligned} \tag{5.22}$$

Similarly, the real wave-functions obtained for the e_g-states are

$$\varphi_\nu = \frac{1}{\sqrt{2}}\left(\varphi_{n22}+\varphi_{n2-2}\right)=\sqrt{\frac{15}{16\pi}}\left[\frac{(x^2-y^2)}{r^2}\right]R_{n2}(r), \tag{5.23}$$

$$\varphi_u = \varphi_{n20}=\sqrt{\frac{15}{16\pi}}\left[\frac{(3z^2-r^2)}{r^2}\right]R_{n2}(r). \tag{5.24}$$

Here, we are interested in Sr_2RuO_4, which is a single-layered tetragonal system. The degenerate t_{2g}- and e_g-states can split in the presence of the tetragonal field. If the Ru symmetry is D_{4h}, as in the case of Sr_2RuO_4, the reducible t_{2g} representation can be written in terms of the irreducible representations of D_{4h} as

$$t_{2g}{=}b_{2g}\oplus e_g,$$

where the xy is the basis function for the b_{2g} and (xz, yz) are the basis functions for the e_g representation. Following the same steps which were explained to derive the cubic crystal-field, one can show that

$$\begin{aligned}
\upsilon_c^{\rm tet}(\mathbf{r}) &= \tilde{\upsilon}_c^{\rm cub}(\mathbf{r})+\upsilon_c^{\rm ax,z}(\mathbf{r}),\\
\upsilon_c^{\rm ax,z}(\mathbf{r}) &= A(r)C_0^{(2)}(\theta,\phi)+B(r)C_0^{(4)}(\theta,\phi),
\end{aligned} \tag{5.25}$$

where $A(r)$ and $B(r)$ are functions of r only. Using Eqs. (5.22) and (5.25), the matrix elements of $v_c^{\mathrm{ax,z}}(\mathbf{r})$ between the components of t_{2g}-states can be obtained. Then by diagonalizing the associated matrix, the splitting Δ_1 of the t_{2g}-states is

$$\Delta_1 = \epsilon(e_g) - \epsilon(b_{2g}) = \frac{3}{7}\langle A(r)\rangle - \frac{5}{21}\langle B(r)\rangle\,, \tag{5.26}$$

where the b_{2g} state is the non-degenerate and e_g is doubly degenerate states. The expectation values in Eq. (5.26) can be given by

$$\begin{aligned}\langle A(r)\rangle &= \int_0^\infty dr\, r^2 A(r) R_{n2}^2(r),\\ \langle B(r)\rangle &= \int_0^\infty dr\, r^2 B(r) R_{n2}^2(r).\end{aligned} \tag{5.27}$$

Similarly, the splitting Δ_2 of the e_g-states can be expressed as

$$\Delta_2 = \epsilon(a_{1g}) - \epsilon(b_{1g}) = \frac{4}{7}\langle A(r)\rangle + \frac{5}{21}\langle B(r)\rangle\,. \tag{5.28}$$

Then the LDA part of Hamiltonian in Eq. (3.3) can be written as

$$\hat{H}^{\mathrm{LDA}} = \sum_{i\sigma}\sum_{mm'} \varepsilon_{m,m'} \hat{c}^\dagger_{im\sigma}\hat{c}_{im'\sigma} - \sum_{\sigma}\sum_{i\neq i'}\sum_{mm'} t^{i,i'}_{m,m'}\hat{c}^\dagger_{im\sigma}\hat{c}_{i'm'\sigma}, \tag{5.29}$$

where the $\varepsilon_{m,m'}$ is the crystal-field matrix, and thus, in principle, in the atomic limit $\varepsilon_{m,m'} = \varepsilon_d\delta_{m,m'}$.
If we massively downfold all bands but the t_{2g}, the associated 3-band Hubbard model becomes

$$\begin{aligned}\hat{H}_e &= \sum_{i\sigma}\sum_{mm'} \varepsilon_{m,m'}\hat{c}^\dagger_{im\sigma}\hat{c}_{im'\sigma} - \sum_{\sigma}\sum_{i\neq i'}\sum_{mm'} t^{i,i'}_{m,m'}\hat{c}^\dagger_{im\sigma}\hat{c}_{i'm'\sigma}\\ &+ U\sum_{im}\hat{n}_{im\uparrow}\hat{n}_{im\downarrow} + \frac{1}{2}\sum_i\sum_{\substack{m\neq m'\\ \sigma\sigma'}} \left(U - 2J - J\delta_{\sigma\sigma'}\right)\hat{n}_{im\sigma}\hat{n}_{im'\sigma}\\ &- J\sum_i\sum_{m\neq m'}\left(\hat{c}^\dagger_{im\uparrow}\hat{c}^\dagger_{im\downarrow}\hat{c}_{im'\uparrow}\hat{c}_{im'\downarrow} + \hat{c}^\dagger_{im\uparrow}\hat{c}_{im\downarrow}\hat{c}^\dagger_{im'\downarrow}\hat{c}_{im'\uparrow}\right),\end{aligned} \tag{5.30}$$

where m, m'=xy, xz, yz, instead, U and J are the direct and exchange screened Coulomb integrals for t_{2g} electrons. Comparing to Eq. (5.7), U=$U_{mm'}$ and J=$J_{mm'}$.

5.3 Single-particle Green functions

Let us consider a system of fermions in the grand canonical ensemble. The time dependence of the operators in the Heisenberg picture is given by

$$\hat{A}(t) = \mathrm{e}^{i(\hat{H}-\mu\hat{N})t}\hat{A}\mathrm{e}^{-i(\hat{H}-\mu\hat{N})t}, \tag{5.31}$$

where μ and $\hat{N}$ are the chemical potential and the particle-number operator, respectively.
The *propagator* or *Green function* of particle is defined by

$$\mathcal{C}_\alpha(\mathbf{r},t;\mathbf{r}',t') = -i\big\langle\hat{\mathcal{T}}\big\{\hat{\psi}_\alpha(\mathbf{r},t)\hat{\psi}^\dagger_\alpha(\mathbf{r}',t')\big\}\big\rangle, \tag{5.32}$$

where $\hat{\mathcal{T}}$ is the time-ordering operator, which orders the operators in decreasing time sequence from left to right. The field operator $\hat{\psi}^\dagger_\alpha(\mathbf{r}',t')$ adds a particle with flavor α to the system at position $\mathbf{r}'$ at time t'. There are various types of single-particle Green functions. The retarded Green function is defined as

$$\mathcal{C}^R_\alpha(\mathbf{r},t;\mathbf{r}',t') = -i\theta(t-t')\left\langle\left[\hat{\psi}_\alpha(\mathbf{r},t)\,,\hat{\psi}^\dagger_\alpha(\mathbf{r}',t')\right]_+\right\rangle, \tag{5.33}$$

where $\theta(t-t')$ is the Heaviside unit step function and the anti-commutator, $[...,...]_+$, is defined as

$$[\hat{A},\hat{B}]_+ = \hat{A}\hat{B}+\hat{B}\hat{A}.$$

In the sense of propagator, $\mathcal{C}^R_\alpha$ has its name "retarded" because it is required that $t > t'$. Although we call them "single-particle Green function", in fact they are many-body objects since they describe the propagation of single particles in a many-body system.
Instead of working with Green functions defined in space and time, it is more convenient to use their Fourier transforms. The field operators can be expressed in terms of the creation and annihilation operators in the basis of plane-waves in the form

$$\begin{aligned}\hat{\psi}_\alpha(\mathbf{r},t) &= \frac{1}{\sqrt{\mathrm{V}}}\sum_{\mathbf{k}}\hat{c}_{\mathbf{k}\alpha}(t)\mathrm{e}^{i\mathbf{k}.\mathbf{r}},\\ \hat{\psi}^\dagger_\alpha(\mathbf{r}',t') &= \frac{1}{\sqrt{\mathrm{V}}}\sum_{\mathbf{k}'}\hat{c}^\dagger_{\mathbf{k}'\alpha}(t')\mathrm{e}^{-i\mathbf{k}'.\mathbf{r}'}.\end{aligned} \tag{5.34}$$

Thus, for a system with translational invariance, where the Green function depends only on the difference $\mathbf{r}-\mathbf{r}'$, we have

$$\mathcal{C}_\alpha^R\big(\mathbf{r}-\mathbf{r}',t,t'\big)=\frac{1}{\mathrm{V}}\sum_{\mathbf{k}\mathbf{k}'}\mathrm{e}^{i\mathbf{k}\cdot\mathbf{r}}\mathcal{C}_\alpha^R\big(\mathbf{k}t,\mathbf{k}'t'\big)\mathrm{e}^{-i\mathbf{k}'\cdot\mathbf{r}'}. \tag{5.35}$$

Since the right hand-side cannot explicitly depend on either the origin or on $\mathbf{r}'$, it follows that $\mathcal{C}_\alpha^R(\mathbf{k},\mathbf{k}')=\delta_{\mathbf{k},\mathbf{k}'}\mathcal{C}_\alpha^R\big(\mathbf{k}\big)$, allowing us to write

$$\mathcal{C}_\alpha^R(\mathbf{k},t,t')=-i\theta(t-t')\left\langle\left[\hat{c}_{\mathbf{k}\alpha}(t),\hat{c}_{\mathbf{k}\alpha}^\dagger(t')\right]_+\right\rangle. \tag{5.36}$$

Taking the Fourier transform with respect to time, the spectral function in the frequency domain is defined as

$$A_\alpha(\mathbf{k},\nu)=-2\,\mathbf{Im}\,\mathcal{C}_\alpha^R(\mathbf{k},\nu), \tag{5.37}$$

where $\mathbf{Im}\,\mathcal{C}_\alpha^R(\mathbf{k},\nu)$ is the imaginary part of the retarded Green function. In the non-interacting case, the Green function, can be calculated exactly. Writing the time dependence of the creation and annihilation operators in the Heisenberg picture, the frequency Fourier transform of the Green function of the non-interacting particles is

$$\mathcal{C}_\alpha^{(0)R}(\mathbf{k},\nu)=\frac{1}{\nu-\xi_{\mathbf{k}\alpha}+i\delta}, \tag{5.38}$$

where $\xi_{\mathbf{k}\alpha}=\varepsilon_{\mathbf{k}\alpha}-\mu$ and δ is a positive infinitesimal.
Using Eqs. (5.37) and (5.38), the spectral function of non-interacting system is obtained as

$$A_\alpha^{(0)}(\mathbf{k},\nu)=2\pi\delta\big(\nu-\xi_{\mathbf{k}\alpha}\big), \tag{5.39}$$

that means an excitation with energy ν can only happen by adding an electron with energy $\xi_{\mathbf{k}\alpha}{=}\nu$.

5.3.1 Matsubara Green functions

The Green function introduced above was defined for arbitrary temperature. However, a consistent perturbation theory can be developed only at zero temperature. At finite temperature the thermal average is taken with real Boltzmann weights,

$$\mathcal{C}_\alpha(\mathbf{r},t;\mathbf{r}',t')=\frac{-i}{Z}\mathrm{Tr}\big(\mathrm{e}^{-\beta(\hat{H}-\mu\hat{N})}\hat{\mathcal{T}}\big\{\hat{\psi}_\alpha(\mathbf{r},t)\hat{\psi}_\alpha^\dagger(\mathbf{r}',t')\big\}\big) \tag{5.40}$$

In order to have a perturbative treatment of the Green function both real and complex exponentials in Eq. (5.40) have to be expanded in powers of the perturbation. Owing to the mixing of the real and complex coefficients, this expression cannot be consistently treated in perturbation theory. As a way out T. Matsubara (1955) introduced an imaginary time variable, τ. The imaginary-time Green function known as the temperature Green function or Matsubara Green function is defined by

$$G_\alpha(\mathbf{r},\tau;\mathbf{r}',\tau') = -\frac{1}{Z}\mathrm{Tr}\big(\mathrm{e}^{-\beta(\hat{H}-\mu\hat{N})}\hat{T}_\tau\big\{\hat{\psi}_\alpha(\mathbf{r},\tau)\hat{\psi}^\dagger_\alpha(\mathbf{r}',\tau')\big\}\big). \tag{5.41}$$

The time dependence of the field operators in the Heisenberg picture is given by replacing $it \to \tau$ in Eq. (5.31). If the Hamiltonian is time-independent, the Green function depends only on $\tau - \tau'$. Convergence of the G_α is guaranteed only if $-\beta \leq \tau - \tau' \leq \beta$.
Using the Fourier series, we find for non-interacting particles

$$G^{(0)}_\alpha(\mathbf{k}, i\nu_n) = \frac{1}{i\nu_n - \xi_{\mathbf{k}\alpha}}. \tag{5.42}$$

Using the Dyson equation

$$G_\alpha(\mathbf{k}, i\nu_n) = G^{(0)}_\alpha(\mathbf{k}, i\nu_n) + G^{(0)}_\alpha(\mathbf{k}, i\nu_n)\Sigma_\alpha(\mathbf{k}, i\nu_n)G_\alpha(\mathbf{k}, i\nu_n), \tag{5.43}$$

the Matsubara Green function for a system of interacting particles is

$$G_\alpha(\mathbf{k}, i\nu_n) = \frac{1}{i\nu_n - \xi_{\mathbf{k}\alpha} - \Sigma_\alpha(\mathbf{k}, i\nu_n)}. \tag{5.44}$$

Assuming the local self-energy approximation, at small energies, we can expand $\Sigma_\alpha(i\nu_n)$ in powers of ν_n, which leads to

$$G^{\mathrm{FL}}_\alpha(\mathbf{k}, i\nu_n) \approx \frac{\mathsf{Z}_\alpha}{i\nu_n - \mathsf{Z}_\alpha\tilde{\xi}_{\mathbf{k}\alpha}}, \tag{5.45}$$

where Z is a matrix with elements defined as Z_α,

$$\mathsf{Z}_\alpha = \frac{1}{m^*_\alpha} = \big(1 - \frac{\mathbf{Im}\,\Sigma_\alpha(i\nu_0)}{\nu_0}|_{\nu_0\to 0^+}\big)^{-1}, \tag{5.46}$$

$$\Gamma_\alpha = -\mathsf{Z}_\alpha \mathbf{Im}\,\Sigma_\alpha(i\nu_0)|_{\nu_0\to 0^+} \tag{5.47}$$

and the effective energy, $\tilde{\xi}_{\mathbf{k}\alpha}$, is expressed as

$$\tilde{\xi}_{\mathbf{k}\alpha} = \xi_{\mathbf{k}\alpha} + \mathbf{Re}\,\Sigma_\alpha(i\nu_0)|_{\nu_0\to 0^+},$$

where $\mathbf{Re}\,\Sigma_\alpha(i\nu_0)$ is the real part of $\Sigma_\alpha(i\nu_0)$.
The relation between the retarded Green function, $\mathcal{C}^R_\alpha(\mathbf{k},\nu)$, and the Matsubara Green function, $G_\alpha(\mathbf{k},i\nu_n)$, is proven by use of the Lehmann representation. If we know $G_\alpha(\mathbf{k},i\nu_n)$, we can find $\mathcal{C}^R_\alpha(\mathbf{k},\nu)$ by analytic continuation,

$$\mathcal{C}^R_\alpha(\mathbf{k},\nu) = G_\alpha(\mathbf{k},i\nu_n \to \nu + i\delta).$$

Therefore, the corresponding spectral function of $\mathcal{C}^{FL}_\alpha(\mathbf{k},\nu)$ is given by

$$A^{\mathrm{FL}}_\alpha(\mathbf{k},\nu) \approx 2\pi \mathsf{Z}_\alpha \delta(\nu - \mathsf{Z}_\alpha\tilde{\xi}_{\mathbf{k}\alpha}) \tag{5.48}$$

This shows that $\mathrm{A}^{\mathrm{FL}}_\alpha$ resembles that of a free electron gas and the pole is identified as quasi-particle. However, since the general sum rule

$$\int_{-\infty}^{\infty} \frac{d\nu}{2\pi} A_\alpha(\mathbf{k},\nu) = 1, \tag{5.49}$$

is not fulfilled by Eq. (5.48), there must be another part of the spectral function, which we denote A'_α, that has an integrated weight given by $1-\mathsf{Z}_\alpha$,

$$A^{\mathrm{FL}}_\alpha(\mathbf{k},\nu) = 2\pi \mathsf{Z}_\alpha \delta(\nu - \mathsf{Z}_\alpha\tilde{\xi}_{\mathbf{k}\alpha}) + A'_\alpha(\mathbf{k},\nu), \tag{5.50}$$

where $A'_\alpha(\mathbf{k},\nu)$ contains more complicated many-body excitation which are not described by a free-electron like spectral function [32].

6

Electronic properties of t_{2g} layered perovskites

Perovskite materials are extremely interesting, from both fundamental and technological points of view [33–38]. The chemical formula for a cubic perovskite is ABC_3, where A is a cation, B is a transition metal and C can be oxygen, O, or one of the halogens. This structure can be viewed as made by BC_6 ochtahedra in which the B ions are surrounded by six C ions; each octahedron is inside a cube of A atoms. The discovery of the first known compound with such a structure, $CaTiO_3$ was made in 1839 by a Russian mineralogist, Perovski, who gave the name to this family of systems. Perovskites are a subject of intensive investigations because of their surprisingly large variety of electrical, magnetic, and structural properties, in many cases very sensitive to external parameters like temperature. Reducing the dimensionality leads to the formation of a peculiar kind of systems, known as *layered perovskites*, with chemical formula $A_{n+1}B_nC_{3n+1}$, where n indicates the number of layers; in the $n \to \infty$ limit, one recovers the cubic perovskite structure. Layered perovskites depending on n, can exhibit different physical and chemical properties. Examples are the ruthenates of Ruddlesden-Popper (RP) family (A=Ca and Sr, B=Ru, C=O), Fig. (6.1), which present Fermi surface anomalies [39] (n=1) and heavy d-electron masses (n=1, 2) [40–43]. It is believed that the surprising properties of ruthenates are the consequence of the interplay of orbital, spin, and lattice degrees of freedom in the partially filled Ru 4d shells. In Ref. [44], using experimental data from x-ray-absorption spectroscopy (XAS) and combining them with LDA+DMFT results, it was shown that, due to the interplay of dimensionality, crystal-field

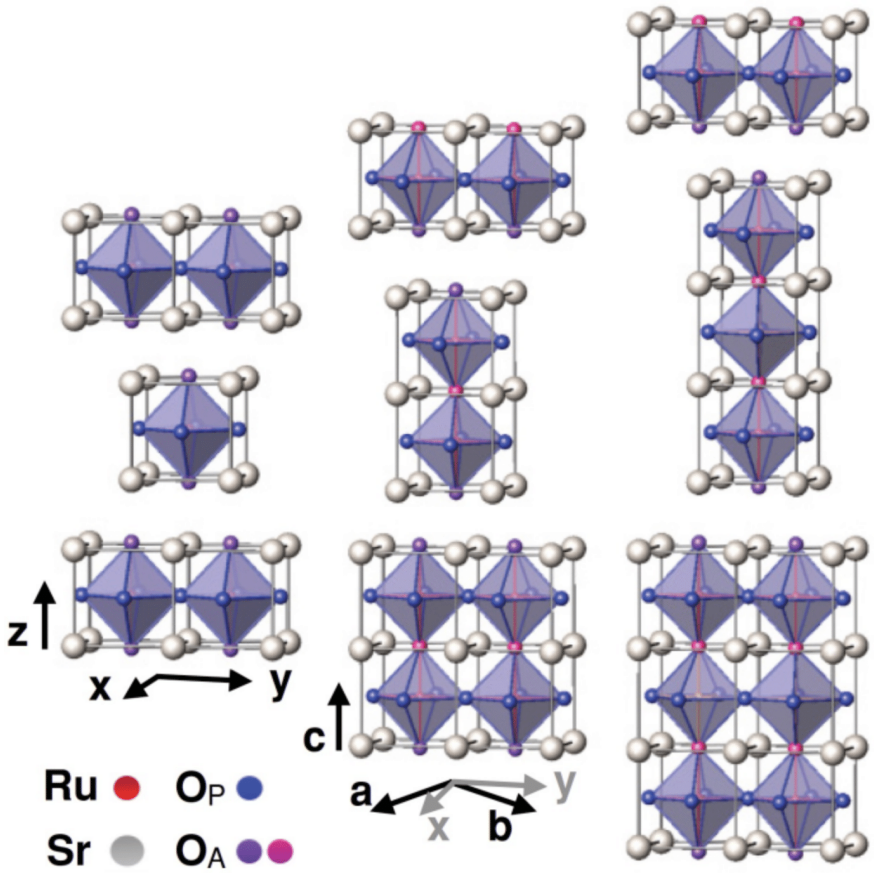


Figure 6.1: The crystal structure of $Sr_{n+1}Ru_nO_{3n+1}$ family (n=1, 2, 3). From left to right: Sr_2RuO_4, $Sr_3Ru_2O_7$ and $Sr_4Ru_3O_{10}$. Figure taken from Ref. [44]. Reprinted figure with permission from [M. Malvestuto, E. Carleschi, R. Fittipaldi, E. Gorelov, E. Pavarini, M. Cuoco, Y. Maeno, F. Parmigiani, and A. Vecchione, Phys. Rev. B 83, 165121 (2011)]. Copyright (2011) by the American Physical Society.

and Coulomb repulsion, there is a significant rearrangement of the t_{2g} orbital occupation in the series. This behavior reflects a shift in the position of the van Hove singularities close to the Fermi level.

One has to observe that materials with perovskite structure are abundantly available in nature, but only in few cases, they exhibit the ideal cubic structure or ideal octahedra. Typically they undergo structural phase transitions that lower the global symmetry. Due to this reduction of symmetry, the degeneracy of the t_{2g} and e_g subshells of the cubic structure is lifted. With respect to the cubic case, in layered perovskites a symmetry reduction is already present due to the missing bonds along the c axis. Furthermore,

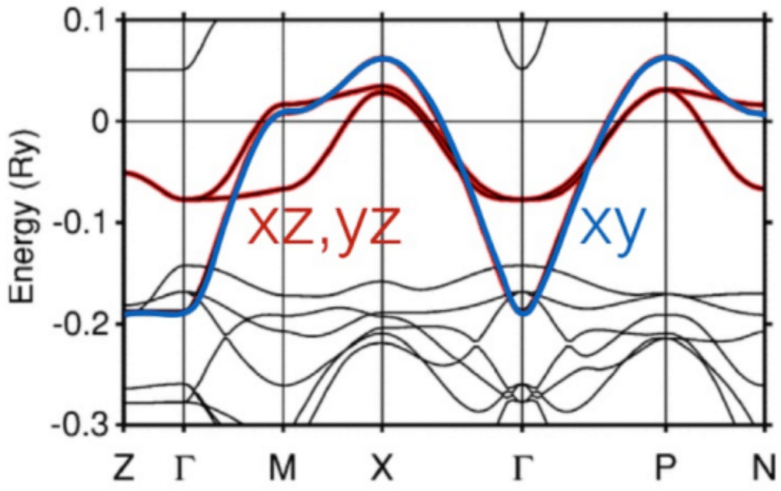


Figure 6.2: The LDA band structure of Sr_2RuO_4 with t_{2g}^4 configuration. Figure taken from Ref. [45]. Reprinted figure with permission from [E. Pavarini and I. I. Mazin, Phys. Rev. B 74, 035115 (2006)]. Copyright (2006) by the American Physical Society.

typically the octahedra elongate along the c axis.
In the following we introduce some representative single-layered perovskite and review their electronic properties.

6.1 Representative materials

In $\mathbf{Sr_2RuO_4}$, ($4d^4$ electronic configuration) due to the tetragonal symmetry, the t_{2g}-states split into a doublet (xz/yz orbitals) and a singlet (xy orbital) and the e_g-states split into two singlets. The energy difference between t_{2g}- and e_g-states is $\sim$ 3.5 eV [44], with the t_{2g}-states lower in energy. Because of this large energy splitting, the nominal electronic configuration of the Ru ions is $\mathbf{t_{2g}^4 e_g^0}$. The intra t_{2g} crystal-field splitting, the parameter which here we call $\varepsilon_{\mathrm{CF}}$, is small, however. In addition, because of the layered structure, the xz and yz bands are almost 1-dimensional, while the xy band is quasi 2-dimensional. As a result, the xy bandwidth, W_{xy}, is approximately twice as large as the xz/yz ones, W_{xz}/W_{yz}. The LDA bands of Sr_2RuO_4 around the Fermi level are shown in Fig. (6.2). The figure shows the t_{2g} bands crossing the Fermi level, in red the xz, yz bands and in blue the xy band. Sr_2RuO_4 has attracted a lot of attention because it is an anomalous superconductor

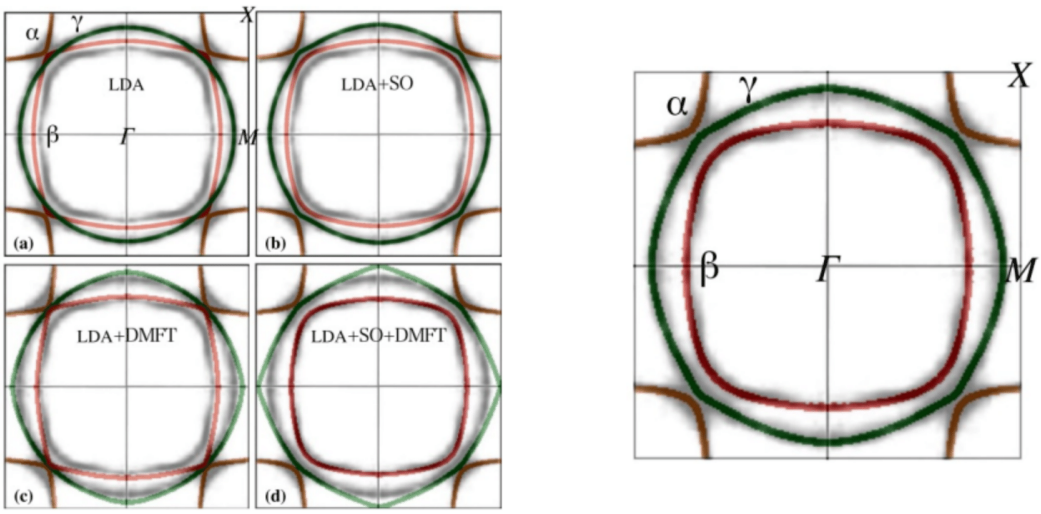


Figure 6.3: Fermi surface of Sr_2RuO_4. Light lines represent the α and β sheets and dark lines the γ sheet. In the left panel, sub-panel (a) shows the Fermi surface obtained via LDA, (b) LDA+SO, (c) LDA+DMFT, and (d) LDA+SO+DMFT calculations with isotropic Coulomb matrix, (U, J)=$(3.1, 0.7)$ eV, in the $T \to 0$ limit. In the right panel, the Fermi surface from LDA+SO+DMFT calculation with D_{4h} Coulomb terms is shown. The calculation is performed for ΔU=$3\Delta U'$=0.3 eV, where ΔU=$U_{xy,xy} - U_{xz,xz}$ and $\Delta U'$=$U_{xy,yz} - U_{xz,yz}$. Figures taken from Ref. [53]. Experimental data are shown with gray density maps taken from Ref. [51]. Reprinted figures with permission from [G. Zhang, E. Gorelov, E. Sarvestani, and E. Pavarini, Phys. Rev. Lett.116, 106402 (2016)]. Copyright (2016) by the American Physical Society.

with T_c∼1.2 K [34]. Its normal state is a Fermi liquid with large effective masses, as is known, e.g., from quantum oscillations [46]. The Fermi surface of Sr_2RuO_4 has been studied experimentally, via de Haas-van Alphen technique [47, 48] and angle-resolved photoemission spectroscopy (ARPES) [49–51]. It is made by three sheets, the electronlike γ (xy band) and β (xz, yz bands) sheets and the holelike α sheet (xz, yz bands). These sheets are shown in Fig. (6.3). From a theoretical point of view, LDA calculations with spin-orbit (SO) interaction reproduce the Fermi surface topology qualitatively [45, 52]. However, these calculations cannot describe the relative size of the sheets. This can be understood from the left panel of the Fig. (6.3), where the experimental Fermi surface from ARPES [51] is shown with gray density. As depicted in sub-panel (a), the LDA describes well the α and γ sheets. However, the area enclosed by the β sheet is larger in LDA than ARPES. Sub-panel (b) shows that switching on the SO interaction, the β-γ crossing becomes an anticrossing; the β sheet shrinks and the γ sheet expands which brings the Fermi surface closer to one from ARPES; how-

ever the β sheet remains too large with respect to the experiment. When the Coulomb interaction has been incorporated via LDA+DMFT, due to the low energy many-body effects on the crystal-field splitting, the α and γ sheets expand whereas the β sheet shrinks; the LDA+DMFT Fermi surface still deviates from ARPES data, however, sub-panel (c). Including the SO term, LDA+SO+DMFT, the agreement worsens for γ sheet and it improves for the α and β sheets; these effects are shown in sub-panel (d). In Ref. [53], via LDA+SO+DMFT calculations, it is shown that the discrepancy can be solved if both SO and Ru D_{4h} low symmetry Coulomb terms are taken into account. The Fermi surface obtained in this way is shown in the right panel of the Fig. (6.3). In the last years, the peculiar role of Hund's rule coupling J in enhancing the effective masses has been pointed out, Hund's metal behavior [54]. Furthermore, sizable effective masses have been further confirmed in experiments[55–57]. Theoretically, the challenge is that several competing interactions have similar strength. Estimation of the average screened Coulomb repulsion shows that it is comparable with the t_{2g} bandwidth [58]. The next example is strontium rhodate, $\mathbf{Sr_2RhO_4}$. Its electronic structure is similar to that of Sr_2RuO_4, however with $\mathbf{t_{2g}^5}$ electronic configuration. In the idealized structure, in which Rh sites have D_{4h} symmetry, the t_{2g} crystal-field splitting is small, about 0.10 eV [59]. The screened Coulomb parameters obtained via cRPA are $U{\sim}2$ eV and $J{\sim}0.2-0.3$ eV [60]. Relatively large mass enhancements have been found from quantum oscillation and ARPES experiments [61, 62]. The experimental Fermi surface is in remarkable disagreement with the one calculated in LDA, a very rare result even for strongly-correlated materials. This discrepancy was partially solved by taking into account the effect of the rotation of the corner-sharing octahedra [63, 64]. However, a discrepancy remained, even after considering the actual crystal structure in the calculations. It was next found that including the SO interaction in the LDA calculations can reduce this disagreement [65]. Furthermore, in Ref. [66] it was shown that the Coulomb interaction leads to an effective Hartree-Fock enhancement of the SO couplings. In fact, with optimal choices of (U, J), the LDA+U Fermi surface becomes close to the experimental one. However, later it was pointed out that the large LDA+U SO enhancement could be an artefact of the static mean-field approximation [67]. In Ref. [59] using LDA+SO+DMFT, it was found that the effective zero frequency enhancement of the SO interaction doubles the value of the corresponding LDA couplings. This result explains the experimental Fermi surface. In Fig. (6.4), the diagonal elements of the t_{2g} spectral function ma-

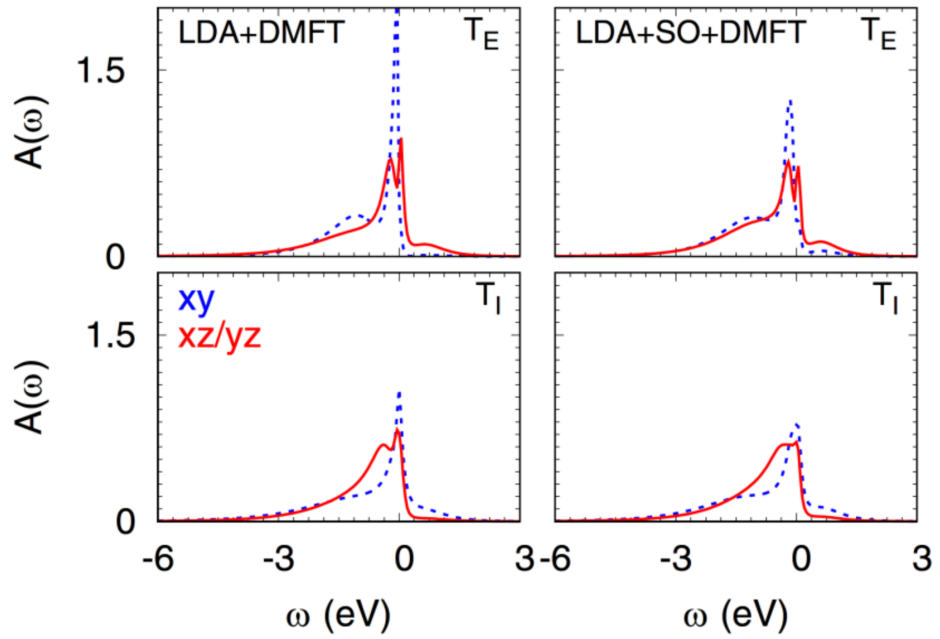


Figure 6.4: The diagonal elements of the t_{2g} spectral function matrix for Sr_2RhO_4. The results for the experimental tetragonal structure are shown in the top panels and the ones for an idealized tetragonal structure are presented in the bottom panels. Calculations are for $T\sim$290 K and (U, J)=(2.3, 0.4) eV. The results obtained via LDA+DMFT are given in the left panels and ones via LDA+SO+DMFT in the right panels. The solid red curves are the spectral function of the xz/yz bands and the dashed blue ones of the xy band. Figure taken from Ref. [59]. Reprinted figure with permission from [G. Zhang and E. Pavarini, Phys. Rev. B 99, 125102 (2019)]. Copyright (2019) by the American Physical Society.

trix are shown. In the figure the top panels present the results obtained for the experimental structure and those for an idealized tetragonal are given in the bottom panels. The left panels are obtained via LDA+DMFT and the right ones via LDA+SO+DMFT.

Now let us consider $\mathbf{Sr_2VO_4}$ with one electron in t_{2g}-states, $\mathbf{t_{2g}^1}$ configuration. In the beginning, Sr_2VO_4 attracted attention as a "dual" of La_2CuO_4, a system that, when doped, shows unconventional superconductivity. It, however, was pointed out by Pickett *et al.* [68] that due to the level of splitting between t_{2g}- and e_g-states, La_2CuO_4 is a $\frac{1}{2}$-filled single-band (x^2-y^2) system, while Sr_2VO_4 is $\frac{1}{6}$-filled three-band (xy, xz, yz) system. Thus, the theoretical idea of unconventional superconductivity in Sr_2VO_4 lost ground to large extent. In addition, experimental studies showed that these two systems have different magnetic and transport properties [69, 70]. In Ref. [71] it was found that under high pressure the crystal-field splitting changes. In this situation,

the xz/yz bands become empty and then, due to the large intra-orbital repulsion, the xy orbital becomes a Mott-insulator. Therefore, Sr_2VO_4 under high pressure is still a candidate for a d^1 superconductor. For what concerns energy scales, ab initio calculations give $\sim$0.08 eV for the crystal-field splitting [72]. Furthermore, the origin of some intriguing properties has been ascribed to the SO interaction [73–76].
Recently, new members of the layered Cr based RP series $Sr_{n+1}Cr_nO_{3n+1}$ beside the 3-dimensional $SrCrO_3$ [77] have been studied, e.g., Sr_2CrO_4 [78], $Sr_3Cr_2O_7$ [79]. These systems have $\mathbf{t_{2g}^2}$ configuration. $\mathbf{Sr_2CrO_4}$ has a dual relation to Sr_2RuO_4, in the sense that it has two holes instead of two electrons in the t_{2g} orbitals. The compound exhibits a rich interplay of SO interaction, tetragonal crystal-field and Coulomb interaction [78]. In Ref. [80] using DFT calculations, it was shown that Sr_2CrO_4 is metallic with narrow t_{2g}-states around the Fermi level. The xy orbital is 0.05 eV lower in energy with respect to the xz/yz orbitals.
In the following we discuss our results. We study single-layered perovskites in the presence of the tetragonal crystal-field and SO interaction. We fix the Coulomb parameters to (U, J)=(2.3, 0.4) eV, the values for Sr_2RuO_4 which have been estimated via cRPA approach [81], and investigate the system when crystal-field splitting, and the filling number, n, of the t_{2g} states, are varying. In the beginning, we present the results in the absence of the SO interaction and later the effects of the SO interaction will be discussed.

6.2 Results without SO interaction

6.2.1 Orbital-resolved spectral functions

Here, we investigate the effect of the crystal-field on the spectral functions. To obtain the spectral functions from QMC data, we employ the maximum entropy method [82]. First, we study the high temperature limit. We present results for five possible integer filling numbers, n=1, 2, 3, 4, 5. We increase crystal-field splitting, $\varepsilon_{\mathrm{CF}}$, from -1.20 eV to 1.20 eV, that is from $-3J$ to $3J$; this allows us to reach the regime in which Hund's rules no longer apply. Positive (negative) $\varepsilon_{\mathrm{CF}}$ indicates that the xy orbital is lower (higher) in energy with respect to the xz/yz orbitals, as shown in Fig. (6.5).
Before we investigate the spectral functions, let us discuss their structure in the strongly-correlated regime. The spectral function in the metallic phase

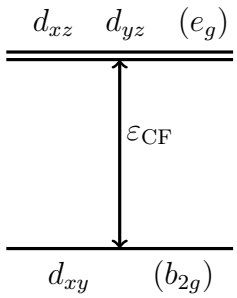


Figure 6.5: Schematic diagram of the arrangement of the xy, xz and yz orbitals in the presence of the crystal-field. When the xy orbital is lower (higher) in energy with respect to the xz/yz orbitals, crystal-field splitting, $\varepsilon_{\rm CF}$, is positive (negative).

is typically characterized by three peaks . An example is shown in Fig. (6.6), where we introduce the terminology that we use in this chapter. The central peak is the so-called quasi-particle peak, and disappears in the Mott insulating regime. The two satellites are the lower and upper Hubbard bands. In the one band case, they are centered around $\pm\frac{U}{2}$, and they become delta functions in the atomic limit.

The spectral functions per spin for different filling numbers and bands are shown in Fig. (6.7). The first row of the figure shows the spectral function for the xy band, $A^{\sigma}_{xy}(\nu)$, the second one for the xz/yz bands, $A^{\sigma}_{xz/yz}(\nu)$, and the third one for the total spectral function, $A^{\sigma}_{t_{2g}}(\nu)$; all functions are plotted versus frequency. Furthermore, in the figure the first column shows the spectral functions for n=1, the second one for n=2, the third one for n=3, the fourth one for n=4, and the fifth one for n=5. The curves are shifted vertically by $\varepsilon_{\rm CF}$. In all panels of the figure, the Fermi level is set equal to zero and it is indicated with the gray dashed line.

First, let us look at the results for $\mathbf{n}$=**1**. The spectral function of the xy band, A^{σ}_{xy}, is represented in panel A_1. The panel shows that at very large negative $\varepsilon_{\rm CF}$, the xy band is almost empty and the orbital occupancy is increasing when $\varepsilon_{\rm CF}$ increases. Furthermore, the number of states near the Fermi level increases with $\varepsilon_{\rm CF}$. At very large positive $\varepsilon_{\rm CF}$ the xy channel is half-filled and the spectral function exhibits the characteristic three peaks structure: the Hubbard bands and the quasi-particle peak near the Fermi level, as expected in the strongly-correlated regime. Next we consider the spectral function for the xz/yz bands, $A^{\sigma}_{xz/yz}$, which is shown in panel A'_1. The orbital occupancy decreases when $\varepsilon_{\rm CF}$ increases, until at very large positive $\varepsilon_{\rm CF}$ ($\varepsilon_{\rm CF}$>0.70 eV)

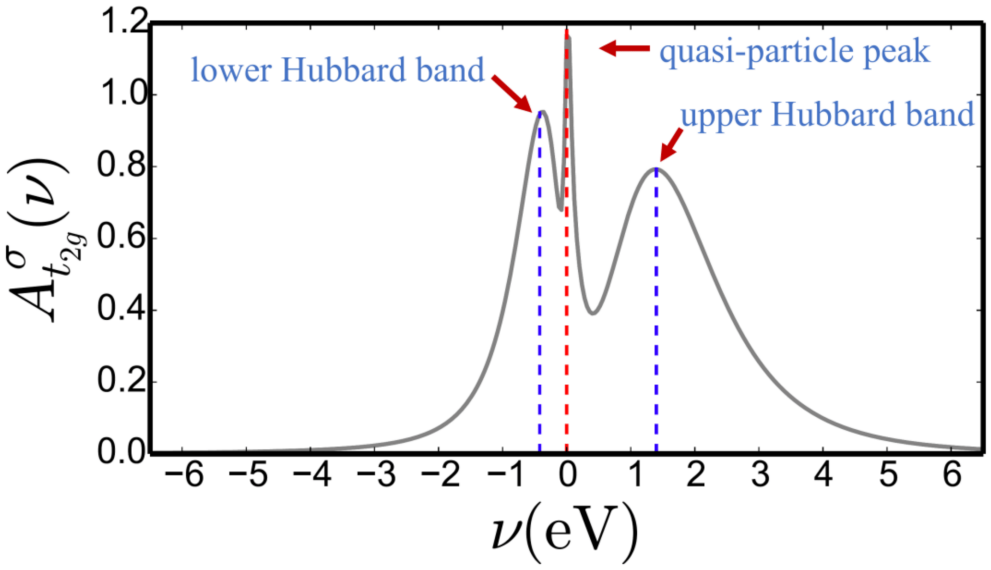


Figure 6.6: The figure represents $A^{\sigma}_{t_{2g}}$ for the n=2 case for $\varepsilon_{\rm CF} = -0.90\,$eV at T=290 K. In this situation the system is in the strongly-correlated regime and the spectral function exhibits a characteristic three peaks structure: the lower and upper Hubbard bands and the quasi-particle peak at the Fermi level.

the band becomes completely empty. At the same time, with increasing $\varepsilon_{\rm CF}$, spectral weight is transferred from negative to positive frequencies. Let us now discuss the result for the total spectral function, $A^{\sigma}_{t_{2g}}$, which is shown in panel A''_1. The figure shows that with increasing $\varepsilon_{\rm CF}$, spectral weight moves from the zero energy quasi-particle peak to the upper Hubbard band with a sharp peak at positive frequency. For $\varepsilon_{\rm CF}$=1.20 eV the spectral function shows a small peak at zero frequency and a larger one at positive frequency. The system remains metallic for all values of $\varepsilon_{\rm CF}$.

Now we consider the results for the **n=2** case. We start from the top panel, panel A_2. For very large negative $\varepsilon_{\rm CF}$ the xy orbital is almost empty. The orbital occupancy increases with increasing $\varepsilon_{\rm CF}$. Instead, the number of states near the Fermi level increases when $\varepsilon_{\rm CF}$ increases on the positive side. As a consequence, at $\varepsilon_{\rm CF}$=0.30 eV the spectral function for the xy channel exhibits a clear zero energy quasi-particle peak. Further increasing $\varepsilon_{\rm CF}$ transfers spectral weight from the quasi-particle peak to the lower and upper Hubbard bands. The xy spectral function remains metallic. Now we analyze the spectral function of the xz/yz channels, which is shown in panel A'_2. The orbitals become empty with increasing $\varepsilon_{\rm CF}$. Starting from very large negative

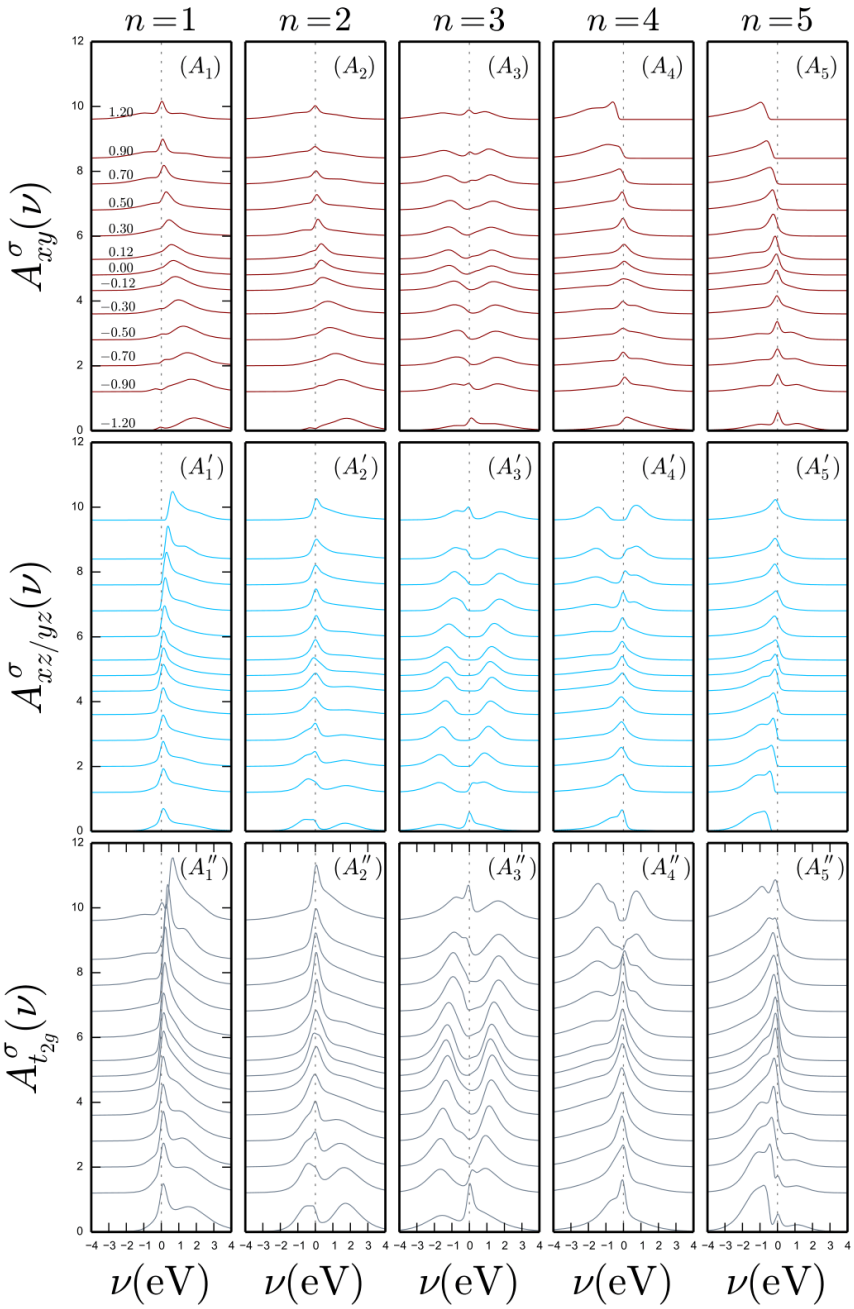


Figure 6.7: Evolution of the spectral functions per spin at T=1160 K with increasing crystal-field splitting, $\varepsilon_{\rm CF}$, for different integer filling numbers. Panels A_n show the spectral function of the xy channel, A'_n the spectral function of the xz/yz channels and A''_n the total spectral function of the system where n is the integer value of the filling number, n=1, 2, 3, 4, 5. In all panels, curves are for the different values of $\varepsilon_{\rm CF}$, defined as $\varepsilon_{\rm CF}$=$\varepsilon_{xz/yz}$−ε_{xy}. The chemical potential is set as the energy zero in all panels. The curves are shifted by an amount proportional to $\varepsilon_{\rm CF}$.

$\varepsilon_{\rm CF}$, one can see that the number of states near the Fermi level is finite, but no large quasi-particle peak is visible. Around $\varepsilon_{\rm CF}=-0.30\,$eV, the spectral function shows a broad zero frequency quasi-particle peak. Further increasing $\varepsilon_{\rm CF}$ leads to the formation of pronounced lower and upper Hubbard bands with a broad zero frequency quasi-particle peak. At $\varepsilon_{\rm CF}$=0.30 eV, the zero frequency quasi-particle peak is relatively narrow and the Hubbard bands spread out. Now let us analyze the behavior of the total spectral function, which is shown in panel A_2''. The system remains metallic for all values of $\varepsilon_{\rm CF}$. At $\varepsilon_{\rm CF}=-0.30\,$eV the spectral function develops a broad zero frequency quasi-particle peak. The peak becomes narrower with increasing $\varepsilon_{\rm CF}$, while spectral weight is transferred from the Fermi level to high frequency.
Let us now look at the results for the **n=3** case. As shown in panel A_3, the spectral function for the xy band shows metallic behavior at very large negative $\varepsilon_{\rm CF}$, until at $\varepsilon_{\rm CF}=-0.70\,$eV it develops a small gap. Increasing $\varepsilon_{\rm CF}$, the gap decreases, until at $\varepsilon_{\rm CF}>0.70\,$eV some spectral weight appears near the Fermi level. At very large positive $\varepsilon_{\rm CF}$ the spectral function shows the characteristic three peaks structure for the metallic phase. Now we analyze the behavior of the spectral function of the xz/yz bands which is shown in panel A_3'. At $\varepsilon_{\rm CF}=-1.20\,$eV the spectral function is metallic with a relatively narrow zero frequency quasi-particle peak. At $\varepsilon_{\rm CF}=-0.90\,$eV it develops a small gap. Further increasing $\varepsilon_{\rm CF}$, the gap becomes larger, then it narrows again. At $\varepsilon_{\rm CF}$=1.20 eV, the spectral function shows metallic behavior with a quite narrow quasi-particle peak at the Fermi level. The gap in the xy band is smaller than the one for the xz/yz bands. The maximum value of the gap for the xy band is obtained for $\varepsilon_{\rm CF}=-0.12\,$eV while for the xz/yz bands it occurs at $\varepsilon_{\rm CF}$=0. Finally we consider the result for the total spectral function which is plotted in panel A_3''. At $\varepsilon_{\rm CF}=-1.20\,$eV the system is a metal with the characteristic three peaks structure. Further increasing $\varepsilon_{\rm CF}$ opens a gap. The gap reaches its maximum value at $\varepsilon_{\rm CF}=-0.12\,$eV. For larger $\varepsilon_{\rm CF}$ the size of the gap decreases when $\varepsilon_{\rm CF}$ increases, until at $\varepsilon_{\rm CF}$=0.70 eV it becomes relatively small. Eventually, the system becomes a metal with a quite narrow quasi-particle peak at the Fermi level. Summarizing, at very large negative and positive $\varepsilon_{\rm CF}$ the system is a metal. In this situation the three bands are not all half-filled, a consequence of the breaking down of the Hund's rules.
Now we look at the next case, **n=4**, which is the hole analogous of n=2 in the atomic limit. First of all, let us consider the spectral function of the xy band which is plotted in panel A_4. Spectral weight is transferred from positive to negative frequency states progressively with increasing $\varepsilon_{\rm CF}$, until

at $\varepsilon_{\rm CF}\geq$0.90 eV the band becomes completely filled. In addition, the number of states near the Fermi level is increasing when $\varepsilon_{\rm CF}$ increases, until at $\varepsilon_{\rm CF}=-0.70$ eV, the spectral function shows a broad quasi-particle peak at the Fermi level. Further increasing $\varepsilon_{\rm CF}$ leads to the disappearance of the zero frequency quasi-particle peak with sizable spectral weight transferred to negative frequency. Furthermore, the spectral function shows metallic behavior for all values of $\varepsilon_{\rm CF}$. Now we consider the spectral function of the xz/yz bands which is shown in panel A_4'. The quasi-particle peak at the Fermi level becomes narrower with increasing $\varepsilon_{\rm CF}$, which means the band goes deeper into the strongly-correlated regime. Furthermore, for $\varepsilon_{\rm CF}\geq$0.12 eV, one can see that spectral weight is transferred from the low energy peak to the high frequency Hubbard band. Finally the system becomes a Mott insulator at $\varepsilon_{\rm CF}$=1.20 eV, when the quasi-particle peak at the Fermi level vanishes and a gap opens. Now we consider the behavior of the total spectral function which is shown in panel A_4''. Again one can see that spectral weight is transferred from low frequency peak to high frequency Hubbard band with increasing $\varepsilon_{\rm CF}$, until at very large positive $\varepsilon_{\rm CF}$ the quasi-particle peak at the Fermi level vanishes and the system becomes a Mott insulator.

Lastly, let us look at the results for $\mathbf{n=5}$ which is the hole analogous of n=1 in the atomic limit. As shown in panel A_5, the orbital occupancy of the xy band increases when $\varepsilon_{\rm CF}$ increases, until at $\varepsilon_{\rm CF}\geq$0.70 eV the xy channel becomes completely filled. Furthermore, increasing $\varepsilon_{\rm CF}$ the quasi-particle peak at the Fermi level becomes narrower, spectral weight is progressively transferred from the zero frequency peak to the Hubbard bands, until at $\varepsilon_{\rm CF}=-0.50$ eV the spectral function exhibits the characteristic three peaks structure. Further increasing $\varepsilon_{\rm CF}$ transfers sizable spectral weight from the upper Hubbard band and the zero frequency quasi-particle peak to the lower Hubbard band. At very large positive $\varepsilon_{\rm CF}$ the zero frequency quasi-particle peak vanishes. Now we consider the spectral function of the xz/yz bands, which is shown in panel A_5'. The orbital occupancy increases when $\varepsilon_{\rm CF}$ decreases, until for $\varepsilon_{\rm CF}\leq-0.70$ eV, the bands become completely filled. Going in the opposite direction, the number of states near the Fermi level increases when $\varepsilon_{\rm CF}$ increases, until at very large positive $\varepsilon_{\rm CF}$ the bands become weakly-correlated, and the spectral function exhibits a broad zero frequency quasi-particle peak. Finally we consider the total spectral function, which is shown in panel A_5''. The figure shows that the system is a metal for all values of $\varepsilon_{\rm CF}$. In addition, the zero frequency quasi-particle peak vanishes when $\varepsilon_{\rm CF}$ increases.

Before looking at the behavior of the spectral functions at lower tempera-

tures, we note that, as discussed in the previous section, for large $|\varepsilon_{\rm CF}|$ the xy orbital or xz/yz orbitals become either completely empty or filled. Since completely filled or empty orbitals do not contribute much to the low energy electronic properties of the system, and as we will see later, the occupation numbers of the bands are almost temperature-independent quantities, low temperature calculations, which are very cpu-demanding, have been only performed up to the crystal-field values which yield the empty/occupied bands. Furthermore, since n=3 yields always an insulator except for very large $|\varepsilon_{\rm CF}|$ and thus the properties do not depend much on the temperature, from now on we only consider n=1, 2, 4, 5.

Let us now look at the spectral functions at T=290 K, room temperature; further reducing the temperature does not bring qualitatively changes, as we will see later on, so this is a temperature representative of the low temperature regime. In particular, we will emphasize the differences with respect to the high temperature regime. The results are shown in Fig. (6.8), where all parameters are defined as in Fig. (6.7). We start from panel A_1, the **n=1** case. Here we see that at $\varepsilon_{\rm CF}=-1.20$ eV, the quasi-particle peak becomes narrower, and spectral weight is transferred from the Fermi level to negative frequencies. When $\varepsilon_{\rm CF}$ increases to $\varepsilon_{\rm CF}=-0.90$ eV, a gap opens and the system becomes a Mott insulator, while at high temperature there is still spectral weight at zero frequency. Also, at $\varepsilon_{\rm CF}=-0.30$ eV and $\varepsilon_{\rm CF}$=0.30 eV spectral weight is transferred to the Hubbard bands. For all remaining values of $\varepsilon_{\rm CF}$, the quasi-particle peak at zero frequency becomes more pronounced. The zero frequency quasi-particle peak becomes sharper also for $A^{\sigma}_{xz/yz}$ and $A^{\sigma}_{t_{2g}}$, as shown in panels A'_1 and A''_1.

Let us now look at the behavior of the spectral functions of the **n=2** case. As shown in panel A_2 of Fig. (6.8), at $\varepsilon_{\rm CF}=-1.20$ eV a gap opens and the system becomes a Mott insulator. In addition, at $\varepsilon_{\rm CF}=-0.90$ eV, A^{σ}_{xy} exhibits the characteristic three peaks structure. Further increasing $\varepsilon_{\rm CF}$ develops a small gap, until at $\varepsilon_{\rm CF}=-0.30$ eV and $\varepsilon_{\rm CF}=-0.12$ eV, again the system shows the characteristic three peaks structure. At $\varepsilon_{\rm CF}$=0 and $\varepsilon_{\rm CF}$=0.12 eV, sizable spectral weight is transferred to negative frequencies and a small gap is formed. At larger values of $\varepsilon_{\rm CF}$, the temperature decrease just leads to a more pronounced zero frequency peak. As shown in panel A'_2, at $\varepsilon_{\rm CF}\leq-0.50$ eV, $A^{\sigma}_{xz/yz}$ exhibits the three peaks characteristic structure. Instead, for small values of $|\varepsilon_{\rm CF}|$, the zero frequency quasi-particle and the Hubbard bands become narrower. In addition, as shown in panel A''_2, for $\varepsilon_{\rm CF}\leq$0 spectral

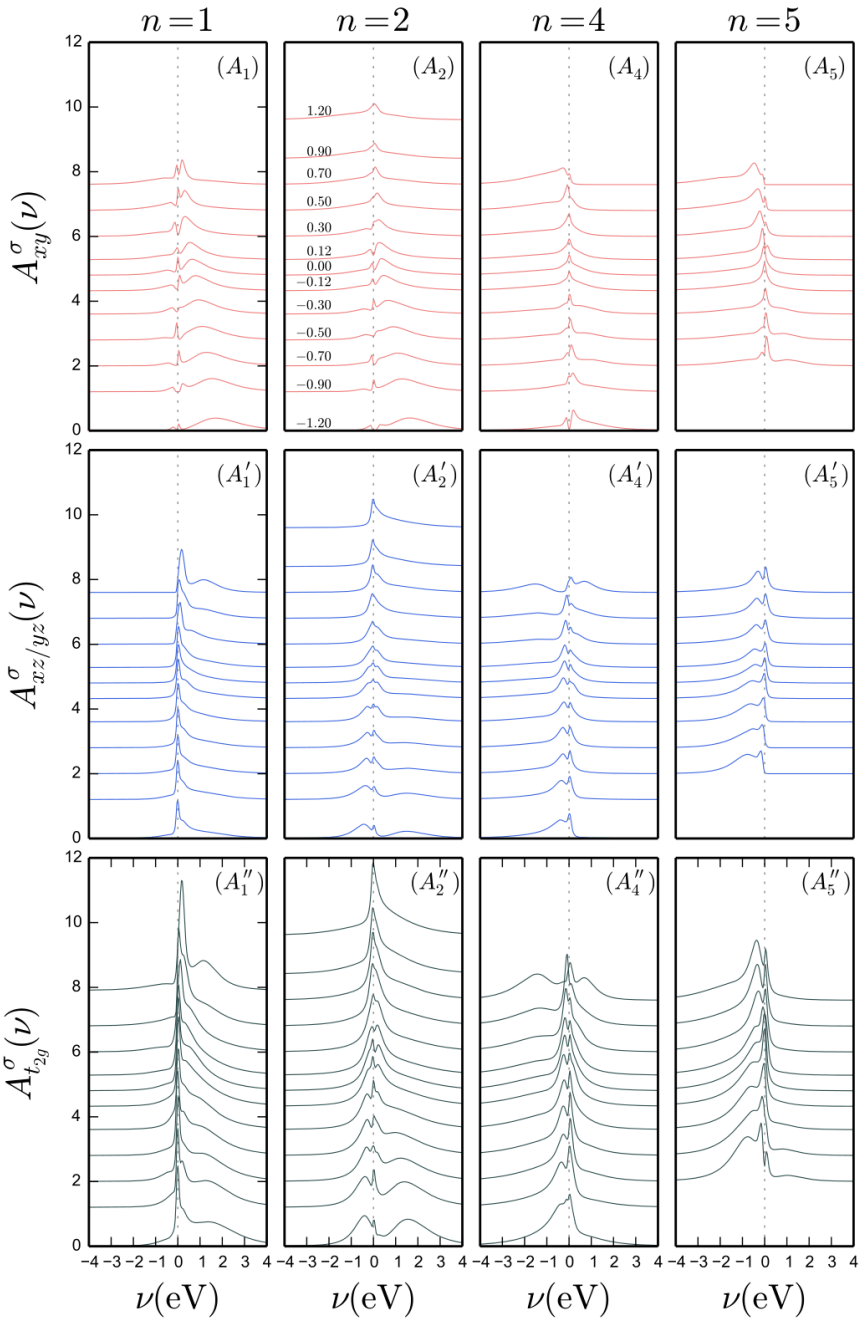


Figure 6.8: Evolution of the spectral functions per spin at T=290 K with increasing crystal-field splitting, $\varepsilon_{\rm CF}$, for different integer filling numbers. Panels A_n show the spectral function of the xy channel, A'_n the spectral function of the xz/yz channels and A''_n the total spectral function of the system where n is the integer value of the filling numbers, $n = 1, 2, 4, 5$. In all panels, curves are for different values of $\varepsilon_{\rm CF}$. The chemical potential is set as the energy zero in all panels.

weight is transferred to the positive and negative frequency which leads to the formation of the three peaks structure. At larger values of $\varepsilon_{\mathrm{CF}}$, the zero frequency quasi-particle peak becomes narrower.
Now we consider the spectral functions for **n=4**. As plotted in panel A_4, at $\varepsilon_{\mathrm{CF}}$=−1.20 eV, A^{σ}_{xy} shows a gap and the system becomes insulator. When $\varepsilon_{\mathrm{CF}}$ increases, spectral weight is transferred to the upper Hubbard band which makes the zero frequency quasi-particle peak more narrower. In addition, for $\varepsilon_{\mathrm{CF}} \geq -0.50$ eV, lowering the temperature makes the zero frequency quasi-particle peak narrower. Now we describe the behavior of the spectral function of the xz/yz bands, shown in panel A'_4. One can see that decreasing temperature transfers spectral weight to negative frequency states, makes the zero frequency quasi-particle peak more pronounced and forms a peak at the lower Hubbard bands for $\varepsilon_{\mathrm{CF}} \leq 0.50$ eV. For $\varepsilon_{\mathrm{CF}}$=0.70 eV, $A^{\sigma}_{xz/yz}$ is similar at both temperatures. Furthermore, the total spectral function, $A^{\sigma}_{t_{2g}}$ shows the same behavior as just discussed for $A^{\sigma}_{xz/yz}$.
Finally, we look at the results for the **n=5** case. As shown in panel A_5, at $\varepsilon_{\mathrm{CF}} = -0.70$ eV, the zero frequency quasi-particle peak becomes narrower and a small peak develops at negative frequency states. At larger values of $\varepsilon_{\mathrm{CF}}$, A^{σ}_{xy} shows a small peak at positive frequency states and the one at negative frequency states, until at $\varepsilon_{\mathrm{CF}}$=0.50 eV where A^{σ}_{xy} shows a small peak at the zero frequency. In addition, at $\varepsilon_{\mathrm{CF}}$=0.70 eV, the peak at negative frequency states becomes sharper. Let us now look at the differences in $A^{\sigma}_{xz/yz}$ at the two temperatures. For $\varepsilon_{\mathrm{CF}} \leq -0.30$ eV, the peaks at negative frequency states become more pronounced. In addition, at larger values of $\varepsilon_{\mathrm{CF}}$ spectral weight is transferred to low frequency. This leads to the formation of two peaks, one at positive frequency and the other at zero frequency. Furthermore, as shown in panel A''_5, the quasi-particle zero frequency peak becomes sharper. The structure of the spectral functions in all channels is the same.
Summarizing, the main effect of lowering temperature is at low energy, where the quasi-particle peak, if present, becomes more narrower, and a gap, if present, becomes more pronounced. The overall trends remain the same.

6.2.2 Occupation numbers and orbital polarization

In DMFT, the occupation numbers of orbitals can be obtained from the Matsubara Green function. Rewriting Eq. (5.41) in terms of creation and

annihilation operators, gives

$$G_\alpha(\tau,\tau') = -\big\langle \hat{T}_\tau \big\{ \hat{c}_\alpha(\tau)\hat{c}^\dagger_\alpha(\tau') \big\} \big\rangle. \tag{6.1}$$

For a time-independent Hamiltonian, the Matsubara Green function depends on the time difference, $\tau - \tau'$. Therefore, choosing τ'=0, Eq. (6.1) can be rewritten as

$$G_\alpha(\tau) = -\big\langle \hat{T}_\tau \big\{ \hat{c}_\alpha(\tau)\hat{c}^\dagger_\alpha(0) \big\} \big\rangle. \tag{6.2}$$

Using the cyclic property of trace, $G_\alpha(\tau)$ has the following symmetry

$$G_\alpha(\tau) = G_\alpha(\tau+\beta) \quad \text{for} \quad -\beta < \tau < 0.$$

Considering Eq. (6.2), the number of electrons of flavor α, can be obtained as

$$G_\alpha(\tau \to 0^+) = -1 + n_\alpha, \quad G_\alpha(\tau \to \beta^-) = -n_\alpha. \tag{6.3}$$

Therefore, using Eq. (6.3), the occupation number of the xy orbital is

$$G^\sigma_{xy}(\tau \to 0^+) = -1 + n^\sigma_{xy}, \quad G^\sigma_{xy}(\tau \to \beta^-) = -n^\sigma_{xy}. \tag{6.4}$$

Instead, the occupation number of the xz/yz orbitals is given by

$$G^\sigma_{xz/yz}(\tau \to 0^+) = -1 + n^\sigma_{xz/yz}, \quad G^\sigma_{xz/yz}(\tau \to \beta^-) = -n^\sigma_{xz/yz}. \tag{6.5}$$

In this section, we study the behavior of the occupation numbers and orbital polarization versus $\varepsilon_{\rm CF}$. The occupation number of the xy and xz/yz orbitals are denoted by n^σ_{xy} and $n^\sigma_{xz/yz}$, respectively, and the orbital polarization is defined as

$$p^\sigma = n^\sigma_{xy} - \frac{1}{2}(n^\sigma_{xz} + n^\sigma_{yz}). \tag{6.6}$$

The results are depicted in Fig. (6.9). The first two columns of the figure show the evolution of n^σ_{xy} and $n^\sigma_{xz/yz}$, respectively, and the last column presents the behavior of p^σ. The first row represents the results for n=1, the second one for n=2, the third one for n=3, the fourth one for n=4 and the fifth one for n=5 case. In the first two columns, the dashed lines correspond to n^σ_m=0.5; m=$xy, xz/yz$, which indicates the half-filled bands. Instead, the dashed line in the third column indicates p^σ=0.
Generally, the figure shows that, on the one hand, n^σ_{xy} increases when $\varepsilon_{\rm CF}$ increases; on the other hand, $n^\sigma_{xz/yz}$ decreases, and as a result, the orbital polarization increases. Furthermore, the behavior of the occupation numbers

$p^\sigma = n^\sigma_{xy} - \frac{1}{2}\left(n^\sigma_{xz} + n^\sigma_{yz}\right)$		
	p^σ_{min}	p^σ_{max}
n=1	$0 - \frac{1}{2}(\frac{1}{2}) = \frac{-1}{4}$	$\frac{1}{2} - \frac{1}{2}(0) = \frac{+1}{2}$
n=2	$0 - \frac{1}{2}(1) = \frac{-1}{2}$	$1 - \frac{1}{2}(0) = +1$
n=4	$0 - \frac{1}{2}(2) = -1$	$1 - \frac{1}{2}(1) = \frac{+1}{2}$
n=5	$\frac{1}{2} - \frac{1}{2}(2) = \frac{-1}{2}$	$1 - \frac{1}{2}(\frac{3}{2}) = \frac{+1}{4}$

Table 6.1: The theoretical limits of the orbital polarization for each filling number.

and the orbital polarization is basically temperature-independent for all presented filling numbers.
Before we start, let us discuss the theoretical limits (maximum and minimum) of the orbital polarization. These are summarized in Tab. (6.1).
With the help of this table, we now discuss the numerical results. First, we investigate the **n=1** case. The xy band, panel B_1, is almost empty for very large negative $\varepsilon_{\mathrm{CF}}$. When $\varepsilon_{\mathrm{CF}}$ increases the band starts filling, and eventually becomes half-filled for very large positive $\varepsilon_{\mathrm{CF}}$, while the xz/yz bands are almost empty for the same limit of $\varepsilon_{\mathrm{CF}}$, shown in panel B_1'. In addition, p^σ becomes zero at small negative $\varepsilon_{\mathrm{CF}}$ and finally reaches its largest value, i.e., $p^\sigma \approx 0.5$, plotted in panel B_1''.
Next, we look at the **n=2** case. Panel B_2 shows that the xy band is almost empty for very large negative $\varepsilon_{\mathrm{CF}}$, and becomes almost half-filled at $\varepsilon_{\mathrm{CF}} \approx 0.70\,\mathrm{eV}$ and $\varepsilon_{\mathrm{CF}} \approx 0.90\,\mathrm{eV}$. Instead, the xz/yz bands are almost half-filled for very large negative $\varepsilon_{\mathrm{CF}}$. When $\varepsilon_{\mathrm{CF}}$ increases $n^\sigma_{xz/yz}$ is reduced, however the bands do not become yet completely empty up to the maximum $\varepsilon_{\mathrm{CF}}$ considered here. Furthermore, for small positive $\varepsilon_{\mathrm{CF}}$, p^σ becomes almost zero. Further increasing $\varepsilon_{\mathrm{CF}}$ turns $p^\sigma > 0$ and finally for very large positive $\varepsilon_{\mathrm{CF}}$, becomes $p^\sigma \approx 0.5$.
Then we consider the **n=3** case. In panel B_3, the occupation number of the xy band is plotted. For very large $\varepsilon_{\mathrm{CF}} < 0$, $n^\sigma_{xy} < 0.5$. When $\varepsilon_{\mathrm{CF}}$ increases to $\varepsilon_{\mathrm{CF}} \approx -0.70\,\mathrm{eV}$, the occupation number is $n^\sigma_{xy} \approx 0.5$ and remains half-filled upon increasing $\varepsilon_{\mathrm{CF}}$, until at very large positive $\varepsilon_{\mathrm{CF}}$ it increases, $n^\sigma_{xy} > 0.5$. In addition, as shown in panel B_3', at $\varepsilon_{\mathrm{CF}} \approx -1.20\,\mathrm{eV}$, $n^\sigma_{xz/yz} > 0.5$, when $\varepsilon_{\mathrm{CF}}$ increases to $\varepsilon_{\mathrm{CF}} \approx -0.90\,\mathrm{eV}$, the bands become half-filled and $n^\sigma_{xz/yz}$ remains unvarying, until at $\varepsilon_{\mathrm{CF}} \approx 1.20\,\mathrm{eV}$ the occupation number of the bands decreases, $n^\sigma_{xz/yz} < 0.5$. Furthermore, p^σ is almost zero, except for very large $|\varepsilon_{\mathrm{CF}}|$.

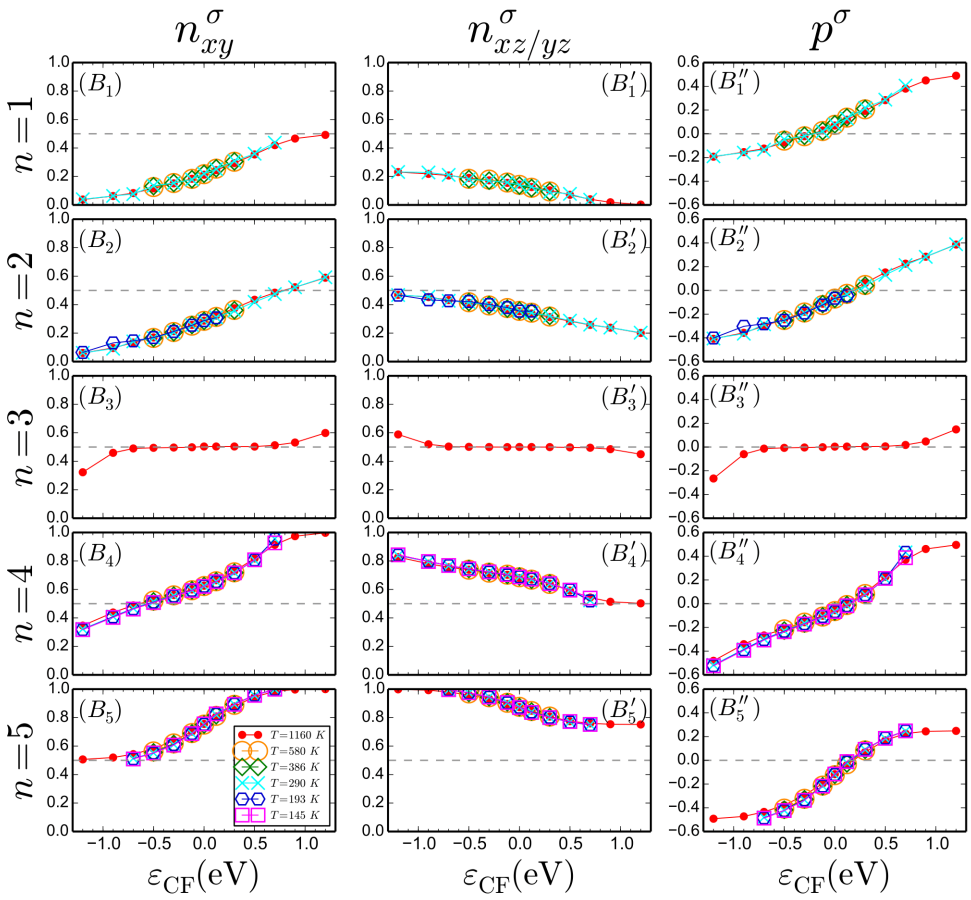


Figure 6.9: Evolution of the occupation numbers per spin of the xy and xz/yz orbitals, n^{σ}_{xy} and $n^{\sigma}_{xz/yz}$, and the orbital polarization per spin, p^{σ}, defined in Eq. (6.6), with increasing $\varepsilon_{\rm CF}$. The results are shown at different temperatures, indicated in the legend of panel B_5, for the five integer filling numbers, n=1, 2, 3, 4, 5. The behavior of n^{σ}_{xy}, $n^{\sigma}_{xz/yz}$ and p^{σ} are plotted in panel B_n, B'_n and B''_n, respectively.

Now we look at the **n=4** case. The xy band is half-filled at $\varepsilon_{\rm CF}\approx -0.50\,$eV and eventually becomes completely filled for very large positive $\varepsilon_{\rm CF}$, where the xz/yz bands are half-filled. Furthermore, as shown in panel B''_4, the smallest value of p^{σ}, i.e., $p^{\sigma}\approx -0.5$, and the largest one, i.e., $p^{\sigma}\approx$0.5 are obtained for very large negative and positive $\varepsilon_{\rm CF}$, respectively. In addition, at $\varepsilon_{\rm CF}\approx -0.12\,$eV, $p^{\sigma}\approx$0.

Lastly, we discuss the **n=5** case. Panel B_5 illustrates that the xy band is half-filled for very large negative $\varepsilon_{\rm CF}$ and eventually becomes completely filled for very large $\varepsilon_{\rm CF}>$0. Instead, the xz/yz bands are completely filled for very

large negative $\varepsilon_{\rm CF}$. In addition, as shown in panel B_5'', for very large negative and positive $\varepsilon_{\rm CF}$, p^σ saturates to $p^\sigma\approx -0.5$ and $p^\sigma\approx 0.25$, respectively and becomes $p^\sigma\approx 0$ at $\varepsilon_{\rm CF}\approx 0.12\,$eV.
We can sum up the results of this section as follows. The orbital polarization becomes almost zero at the same value of $\varepsilon_{\rm CF}$, i.e., $\varepsilon_{\rm CF}\approx 0.12\,$eV for the n=2, 4, 5 cases. Instead, for n=1, $p^\sigma\approx 0$ at $\varepsilon_{\rm CF}\approx -0.12\,$eV, while for the n=3 case, it is almost zero for all values of $\varepsilon_{\rm CF}$, except for very large $|\varepsilon_{\rm CF}|$. Furthermore, the xy band becomes half-filled at different values of $\varepsilon_{\rm CF}$, depending on the filling number. For n=1, this is obtained for very large positive $\varepsilon_{\rm CF}$, for n=2 at $\varepsilon_{\rm CF}\approx 0.70\,$eV and $\varepsilon_{\rm CF}\approx 0.90\,$eV, at n=3 at all values of $\varepsilon_{\rm CF}$, except for very large $|\varepsilon_{\rm CF}|$, for the n=4 case, at $\varepsilon_{\rm CF}\approx -0.50\,$eV and for the n=5 case, for large negative $\varepsilon_{\rm CF}$. Instead, the xz/yz bands become half-filled only at filling numbers n=2, 3, 4 in the energy window considered. For n=2, the xz/yz bands become half-filled at $\varepsilon_{\rm CF}\approx -1.20\,$eV, for n=3 for all values of $\varepsilon_{\rm CF}$, except for $|\varepsilon_{\rm CF}|\approx 1.20\,$eV, and for the n=4 case, for very large positive $\varepsilon_{\rm CF}$. In addition, the xy band becomes completely filled only for the n=4, 5 cases for very large positive $\varepsilon_{\rm CF}$ in the energy window considered. In all other cases, one would have to further increase $\varepsilon_{\rm CF}$ to obtain n^σ_{xy}=1. In the considered interval of $\varepsilon_{\rm CF}$, the xy band is almost empty only for n=1, 2 cases, at $\varepsilon_{\rm CF}\approx -1.20\,$eV. In addition, the xz/yz bands become completely filled just for the n=5 case, for very large negative $\varepsilon_{\rm CF}$, while the bands are completely empty only for n=1 case, for the opposite limit of $\varepsilon_{\rm CF}$.
Here we discuss the numerical details. In Fig. (6.10), we show a typical $G(\tau)$ and its borders. The number of electrons of the xy band is obtained from $G^\sigma_{xy}(\tau)$ at τ=0^+ and τ=β^-. The figure shows that at τ=0^+, $G^\sigma_{xy}(\tau)\approx -0.2$, which indicates that $n^\sigma_{xy}\approx 0.8$. As shown in Eqs. (6.4) and (6.5), the occupation numbers of the xy and xz/yz orbitals can be extracted from the corresponding components of the Matsubara Green function. The behavior of $G^\sigma_{xy}(\tau)$ and $G^\sigma_{xz/yz}(\tau)$ are shown in Figs. (6.11) and (6.12), respectively. Each panel presents the results for different filling numbers. The figures show the evolution of the Matsubara Green functions with increasing $\varepsilon_{\rm CF}$; the curves are shifted vertically of $\varepsilon_{\rm CF}$, with the rule that $\varepsilon_{\rm CF}$ is increasing from bottom to top in each panel. Now let us look at some representative limit cases. As shown in panel B_1' of Fig. (6.9), for the n=1 case, the xz/yz bands become completely empty at $\varepsilon_{\rm CF}\approx 1.20\,$eV. The corresponding Matsubara Green functions for this case is the first curve from the top in the first column of Fig. (6.12). We see that $G^\sigma_{xz/yz}(\tau)$ raises sharply from -1

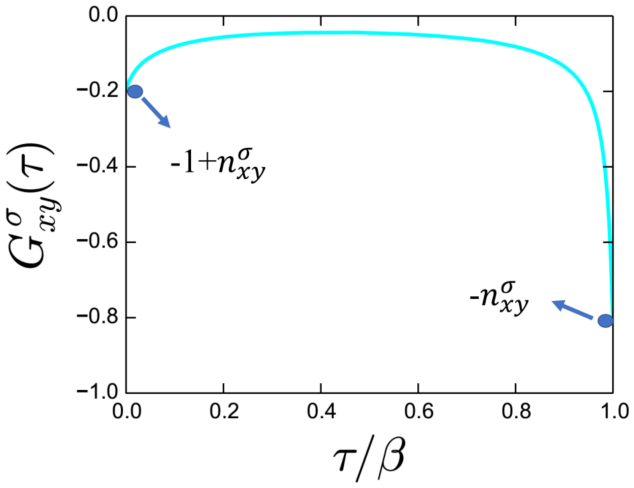


Figure 6.10: The Matsubara Green function for the xy band, $G^{\sigma}_{xy}(\tau)$. The function is plotted for the n=4 case, at T=290 K, and for $\varepsilon_{\rm CF}$=0.50 eV. The horizontal axis scales as τ/β, where $\beta = \frac{1}{\rm k_B T}$.

at $\tau = 0^+$, $G^{\sigma}_{xz/yz}(0^+) \approx -1$, and then it becomes zero at $\tau=\beta^-$. Instead, as shown in panel B_5 of Fig. (6.9), for the n=5 case, the xy band becomes completely filled at $\varepsilon_{\rm CF} \geq 0.70$ eV. The equivalent Matsubara Green functions for this case are the first three curves from the top in the last column of Fig. (6.11). In this case the Matsubara Green function is almost zero at $\tau=0^+$ and it falls steeply to -1 at $\tau=\beta^-$, $G^{\sigma}_{xy}(\beta^-) \approx -1$. Instead, for the half-filled band the corresponding Matsubara Green function has the same value at $\tau=0^+$ and $\tau=\beta^-$, i.e., $G^{\sigma}_{m}(\beta^-)=G^{\sigma}_{m}(0^+) \approx -0.5$. As an example for this case, the xy band for n=3 for $\varepsilon_{\rm CF} \approx 0.50$ eV is half-filled which is shown in panel B_3 of Fig. (6.9); the corresponding Matsubara Green function is the fourth curve from the top in the third column of Fig. (6.11).
The behavior of the Matsubara Green functions at different temperatures are presented with different colors in Figs. (6.11) and (6.12). Since the occupation numbers in all channels are temperature-independent, the values do not change at $\tau=0^+$ and $\tau=\beta^-$ with decreasing the temperature. However, the Matsubara Green functions become steeper when the temperature decreases. The Green functions are represented with lines in the figures. The QMC error bars are smaller than the line width, in the scale shown in the figures.
An important point of DMFT calculations is the convergence of quantities towards a self-consistent solution. The convergence plots of the occupation numbers, n^{σ}_{xy} and $n^{\sigma}_{xz/yz}$, for n=4, are represented in Figs. (6.13) and (6.14)

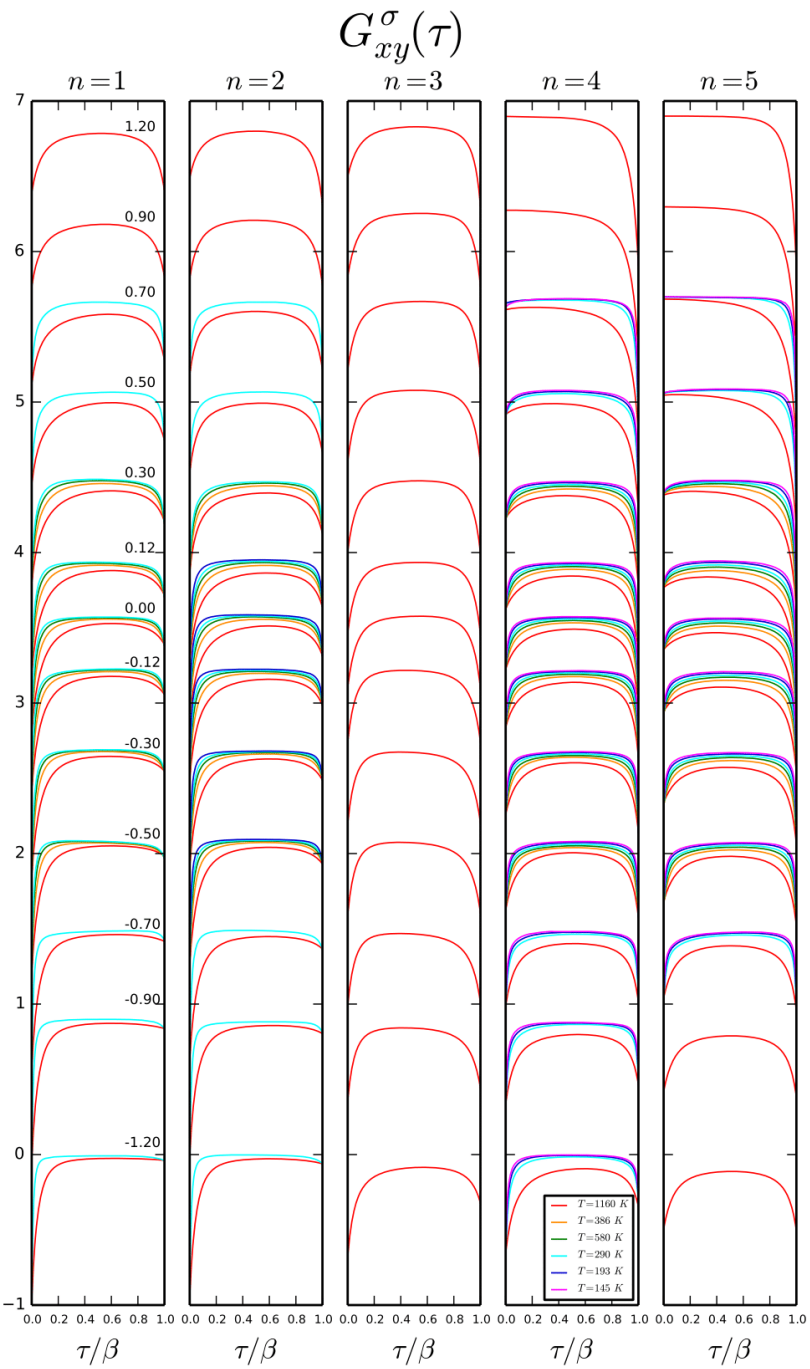


Figure 6.11: Evolution of the Matsubara Green function for the xy orbital, $G^{\sigma}_{xy}(\tau)$, with increasing $\varepsilon_{\mathrm{CF}}$. The results are shown for the five integer filling numbers, n=1, 2, 3, 4, 5 and at different temperatures. The curves are shifted vertically by $\varepsilon_{\mathrm{CF}}$, that $\varepsilon_{\mathrm{CF}}$ is increasing from bottom to top in each panel from $\varepsilon_{\mathrm{CF}}=-1.20\,\mathrm{eV}$ to $\varepsilon_{\mathrm{CF}}$=1.20 eV. The horizontal axes scale as τ/β, where $\beta=\frac{1}{\mathrm{k_B T}}$.

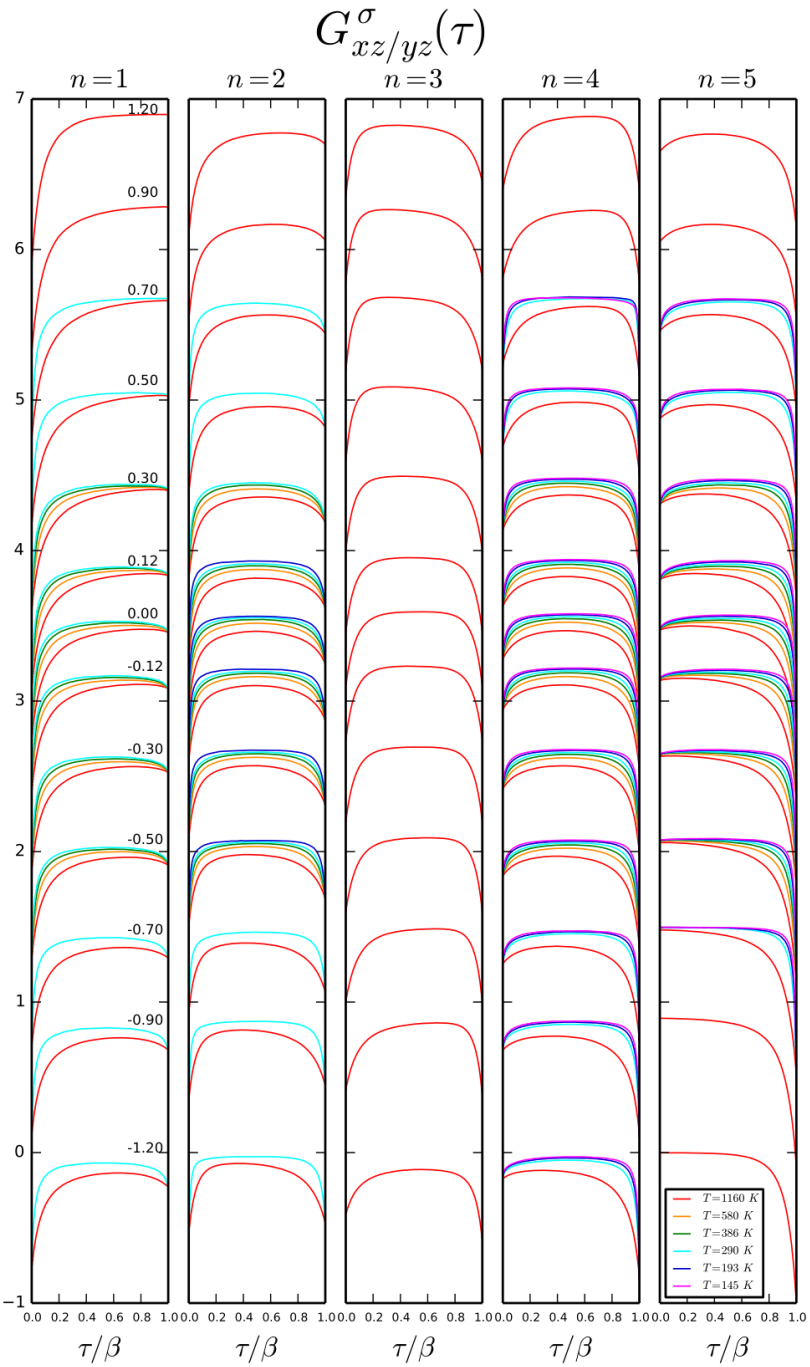


Figure 6.12: Evolution of the Matsubara Green function for the xz/yz orbitals, $G^{\sigma}_{xz/yz}(\tau)$, with increasing $\varepsilon_{\mathrm{CF}}$. The results are shown for the five integer filling numbers, n=1, 2, 3, 4, 5 and at different temperatures. The curves are shifted vertically by $\varepsilon_{\mathrm{CF}}$, that $\varepsilon_{\mathrm{CF}}$ is increasing from bottom to top in each panel from $\varepsilon_{\mathrm{CF}}=-1.20\,\mathrm{eV}$ to $\varepsilon_{\mathrm{CF}}$=1.20 eV. The horizontal axes scale as τ/β, where $\beta=\frac{1}{\mathrm{k_B T}}$.

at different temperatures, respectively. As shown in the figures, the occupation numbers converge quickly at all considered temperatures and all values of $\varepsilon_{\mathrm{CF}}$. In fact, these are the quantities that converge quickly. The effective masses and energy differences often requires more iterations.

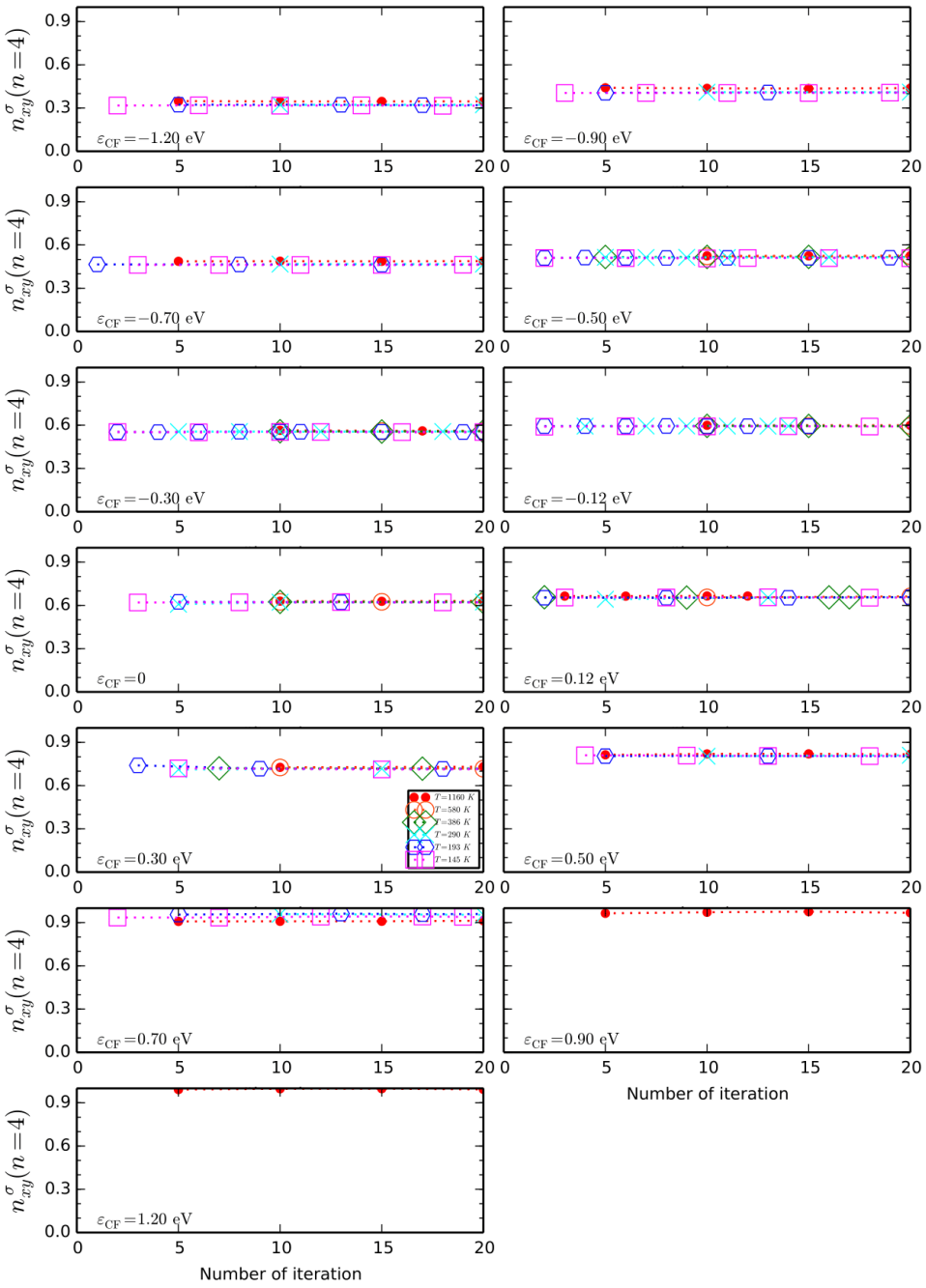


Figure 6.13: Convergence plots for n^{σ}_{xy} for n=4 case at different temperatures. Each panel shows the result for different values of $\varepsilon_{\mathrm{CF}}$.

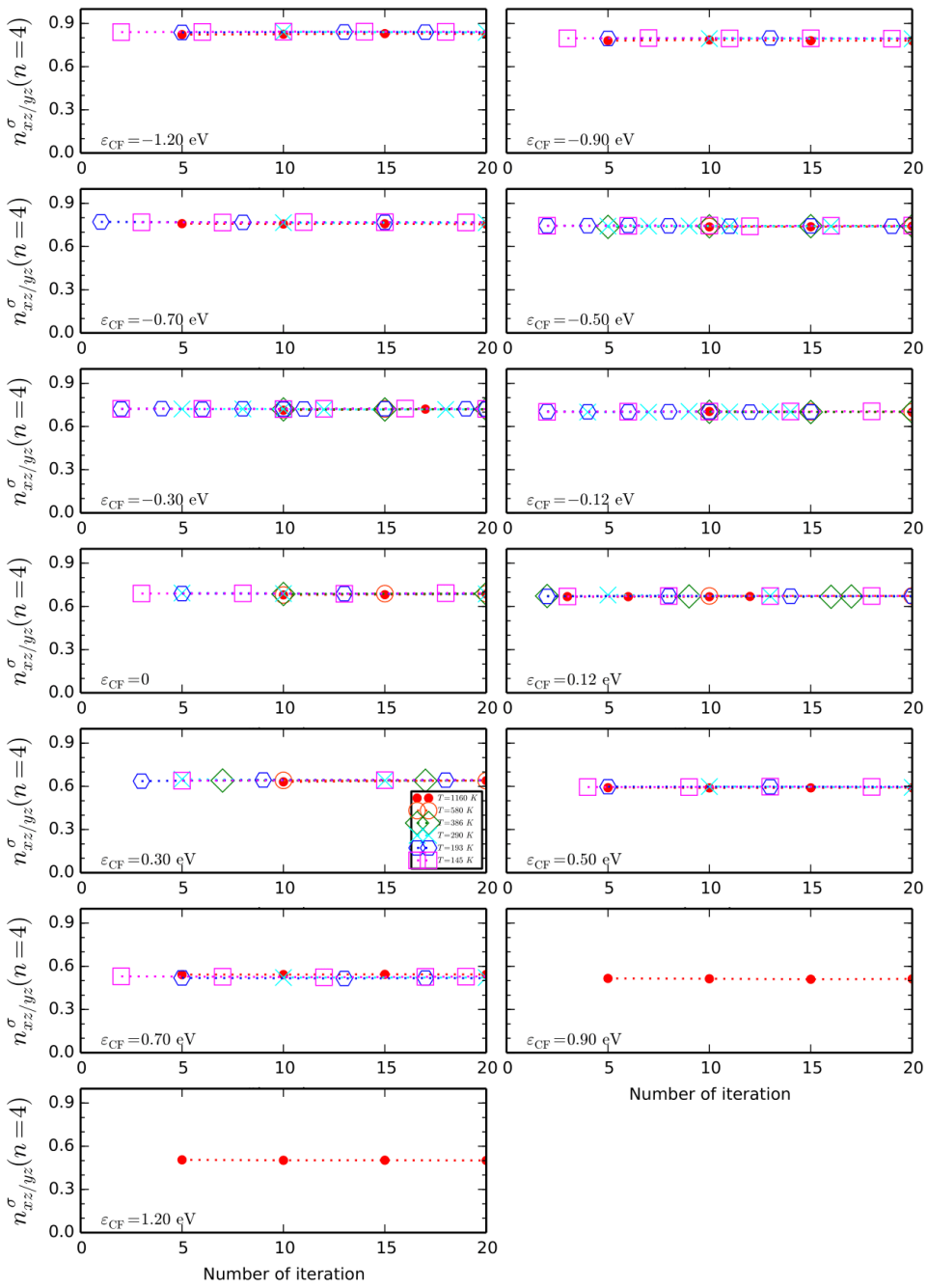


Figure 6.14: Convergence plots for $n^{\sigma}_{xz/yz}$ for n=4 case at different temperatures. Each panel shows the result for different values of $\varepsilon_{\mathrm{CF}}$.

6.2.3 Effective-masses and scattering rates

In this section, we investigate the effective-mass enhancement and the corresponding quasi-particle scattering rate versus $\varepsilon_{\rm CF}$. Using Eq. (5.46), the effective-mass enhancement, m^*, and the quasi-particle scattering rate, Γ, in each orbital can be written as follows:

$$m^{*\sigma}_{xy} = \frac{1}{\mathsf{Z}^{\sigma}_{xy}} = \Big(1 - \frac{\mathbf{Im}\,\Sigma^{\sigma}_{xy}(i\nu_0)}{\nu_0}\Big), \quad \Gamma^{\sigma}_{xy} = -\mathsf{Z}^{\sigma}_{xy}\mathbf{Im}\,\Sigma^{\sigma}_{xy}(i\nu_0), \tag{6.7}$$

$$m^{*\sigma}_{xz} = \frac{1}{\mathsf{Z}^{\sigma}_{xz}} = \Big(1 - \frac{\mathbf{Im}\,\Sigma^{\sigma}_{xz}(i\nu_0)}{\nu_0}\Big), \quad \Gamma^{\sigma}_{xz} = -\mathsf{Z}^{\sigma}_{xz}\mathbf{Im}\,\Sigma^{\sigma}_{xz}(i\nu_0), \tag{6.8}$$

$$m^{*\sigma}_{yz} = \frac{1}{\mathsf{Z}^{\sigma}_{yz}} = \Big(1 - \frac{\mathbf{Im}\,\Sigma^{\sigma}_{yz}(i\nu_0)}{\nu_0}\Big), \quad \Gamma^{\sigma}_{yz} = -\mathsf{Z}^{\sigma}_{yz}\mathbf{Im}\,\Sigma^{\sigma}_{yz}(i\nu_0). \tag{6.9}$$

Since the behavior of the results for the half-filling case, n=3, is different from the one obtained for all other n values, we present the discussion first for $n\neq3$. Figure (6.15) shows the corresponding results. In the figure, the first two columns show the evolution of the effective-mass enhancement in the xy and xz/yz orbitals, $m^{*\sigma}_{xy}$ and $m^{*\sigma}_{xz/yz}$, and the behavior of the corresponding quasi-particle scattering rates, Γ^{σ}_{xy} and $\Gamma^{\sigma}_{xz/yz}$, are delineated in the last two columns. Different rows illustrate the results for the filling numbers, sequentially. In each panel, different curves are results at different temperatures.

Fermi liquid theory relies on the assumption that the excitation created by adding/removing a particle to the system at low energy can be described via a *quasi-particle* with a long lifetime. For a free electron system, $m^*\approx1$, while approaching the Mott insulator regime $m^*\rightarrow\infty$. When the band becomes completely empty or filled, m^* and Γ have, of course, no physical meaning.

In the beginning, we look at the trend of the effective-mass enhancement of the electrons in the channels. First, let us investigate the $\mathbf{n=1}$ case. The mass in the xy channel increases when $\varepsilon_{\rm CF}$ increases, whereas $m^{*\sigma}_{xz/yz}$ shows descending behavior, shown in panels M_1 and M_1'. Furthermore, $m^{*\sigma}_{xy}$ and $m^{*\sigma}_{xz/yz}$ remain almost unvarying with lowering the temperature.

Next, we look at $\mathbf{n=2}$. Panel M_2 shows that the maximum of the mass in the xy channel is gained at $\varepsilon_{\rm CF}\approx0.90\,$eV where the band is half-filled. Also, the electrons in the xy channel become heavier when the temperature decreases. The temperature dependence is weak for $\varepsilon_{\rm CF}<0$, but becomes strong for large $\varepsilon_{\rm CF}>0$. Panel M_2' shows that decreasing the temperature enhances $m^{*\sigma}_{xz/yz}$,

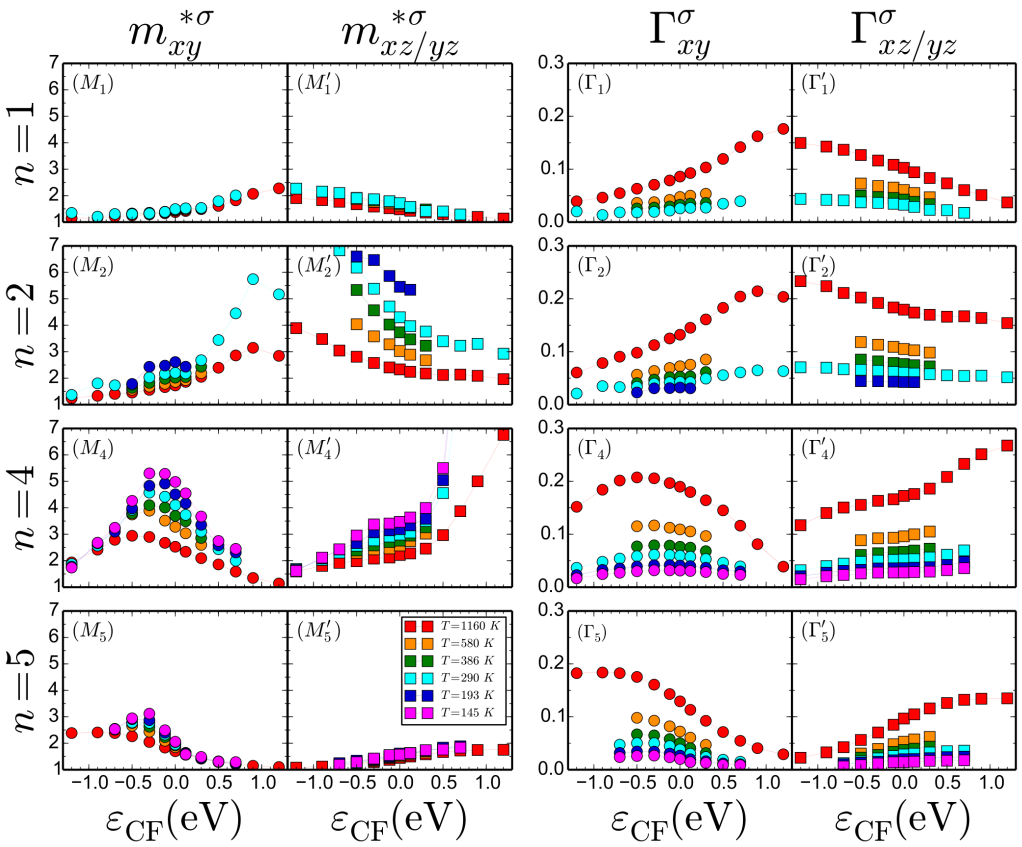


Figure 6.15: The behavior of the effective-mass enhancement in the xy and xz/yz orbitals per spin, $m^{*\sigma}_{xy}$ and $m^{*\sigma}_{xz/yz}$, and the corresponding quasi-particle scattering rate, Γ^{σ}_{xy} and $\Gamma^{\sigma}_{xz/yz}$, with increasing $\varepsilon_{\rm CF}$ at different temperatures. The quantities are represented for the four integer filling numbers, n=1, 2, 4, 5. The first two columns show the behavior of $m^{*\sigma}_{xy}$ and $m^{*\sigma}_{xz/yz}$, and the last two ones the behavior of Γ^{σ}_{xy} and $\Gamma^{\sigma}_{xz/yz}$, respectively. The behavior of $m^{*\sigma}_{xy}$ and $m^{*\sigma}_{xz/yz}$ are shown in panels M_n and M'_n, while Γ_n and Γ'_n panels represent the results for Γ^{σ}_{xy} and $\Gamma^{\sigma}_{xz/yz}$, respectively. In each panel different colors represent different temperatures, which are shown in the legend of panel M'_5.

but the rate of the enhancement is more rapid for larger $\varepsilon_{\rm CF}$<0. Furthermore, the electrons in the xz/yz channels become more massive when $\varepsilon_{\rm CF}$ decreases. This behavior is in agreement with the results of the corresponding $A^{\sigma}_{xz/yz}$, which shows that the system goes deeper into the strongly-correlated regime.

Then we consider the **n=4** case. We find that the mass in the xy channel has a maximum at $\varepsilon_{\rm CF}\approx -0.30\,$eV. This is true at any temperature, but the maximum is enhanced with lowering the temperature. However, $m^{*\sigma}_{xy}$ varies

little with the temperature for large $|\varepsilon_{\mathrm{CF}}|$. Panel M_4' illustrates that $m^{*\sigma}_{xz/yz}$ eventually diverges when $\varepsilon_{\mathrm{CF}}$ increases. This trend is in line with the behavior of equivalent $A^{\sigma}_{xz/yz}$ where the system is approaching the Mott insulator regime. In addition, when the temperature decreases $m^{*\sigma}_{xz/yz}$ becomes larger; the temperature dependence is strong for large positive $\varepsilon_{\mathrm{CF}}$.
Lastly, let us look at **n=5**. We find that at high temperatures, $m^{*\sigma}_{xy}$ decreases when $\varepsilon_{\mathrm{CF}}$ increases, but it has a maximum at $\varepsilon_{\mathrm{CF}}\approx -0.30\,\mathrm{eV}$ at lower temperatures. For $\varepsilon_{\mathrm{CF}}$ around the maximum, $m^{*\sigma}_{xy}$ increases somewhat when the temperature decreases. Furthermore, the electrons in the xz/yz channels become slightly heavier when $\varepsilon_{\mathrm{CF}}$ increases. In addition, $m^{*\sigma}_{xz/yz}$ remains almost unchanged with lowering the temperature at every $\varepsilon_{\mathrm{CF}}$.
Next, we analyze the corresponding quasi-particle scattering rates. Generally, the figure shows that at any $\varepsilon_{\mathrm{CF}}$, when the temperature decreases the quasi-particle scattering rates are reduced in all channels and for all filling numbers. This is in agreement with what we expect in Fermi liquid theory, where the scattering rate of the quasi-particles is approaching zero at $\nu,\, T \to 0$. Furthermore, Γ^{σ}_{xy} and $\Gamma^{\sigma}_{xz/yz}$ show a weak dependency on $\varepsilon_{\mathrm{CF}}$ at low temperatures. Thus in the following, we look at the evolution of Γ^{σ}_{xy} and $\Gamma^{\sigma}_{xz/yz}$ versus $\varepsilon_{\mathrm{CF}}$ at high temperatures, where the dependency on $\varepsilon_{\mathrm{CF}}$ is emphasized.
In panels Γ_1 and Γ_1', we observe that for **n=1**, Γ^{σ}_{xy} exhibits an ascending behavior when $\varepsilon_{\mathrm{CF}}$ increases, whereas $\Gamma^{\sigma}_{xz/yz}$ shows descending trend.
For the **n=2** case, Γ^{σ}_{xy} has a maximum at $\varepsilon_{\mathrm{CF}}\approx 0.90\,\mathrm{eV}$. This is in line with what we saw in the corresponding A^{σ}_{xy} where the width of the zero frequency quasi-particle peak is widest at $\varepsilon_{\mathrm{CF}}\approx 0.90\,\mathrm{eV}$. In addition, $\Gamma^{\sigma}_{xz/yz}$ decreases when $\varepsilon_{\mathrm{CF}}$ increases, as shown in panel Γ_2'. This behavior is in line with the result of the equivalent $A^{\sigma}_{xz/yz}$ where the width of the zero frequency quasi-particle peak becomes wider when $\varepsilon_{\mathrm{CF}}$ decreases.
Then, we investigate the **n=4** case. In panel Γ_4 we see that Γ^{σ}_{xy} has maximum at $\varepsilon_{\mathrm{CF}}\approx -0.50\,\mathrm{eV}$ and is quite low at very large positive $\varepsilon_{\mathrm{CF}}$ where the band is completely filled. Furthermore, panel Γ_4' shows that $\Gamma^{\sigma}_{xz/yz}$ is enhanced when $\varepsilon_{\mathrm{CF}}$ increases, until becomes very large at large positive $\varepsilon_{\mathrm{CF}}$ where the bands are half-filled.
Lastly, we consider the **n=5** case. Panel Γ_5 shows that Γ^{σ}_{xy} does not change at very large $\varepsilon_{\mathrm{CF}}<0$ when $\varepsilon_{\mathrm{CF}}$ increases. In this limit the band is half-filled and Γ^{σ}_{xy} has its highest value. At larger $\varepsilon_{\mathrm{CF}}$, it shows descending behavior. In addition, $\Gamma^{\sigma}_{xz/yz}$ is enhanced when $\varepsilon_{\mathrm{CF}}$ increases.

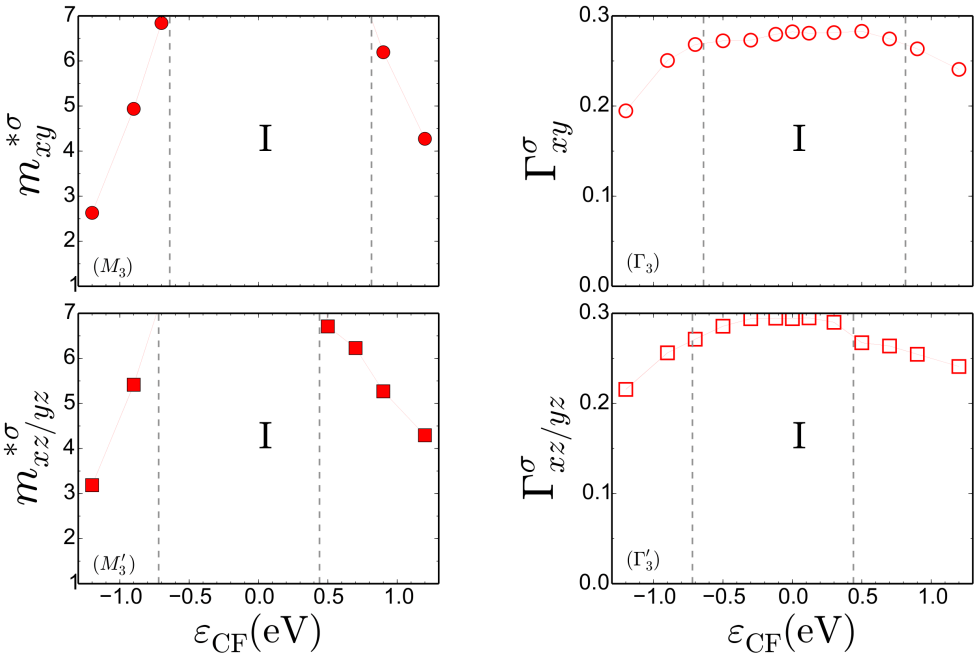


Figure 6.16: The evolution of the effective-mass enhancement in the xy and xz/yz orbitals, $m^{*\sigma}_{xy}$ and $m^{*\sigma}_{xz/yz}$, respectively and the corresponding quasi-particle scattering rate, Γ^{σ}_{xy} and $\Gamma^{\sigma}_{xz/yz}$ versus $\varepsilon_{\mathrm{CF}}$. The quantities are calculated at T=1160 K for the n=3 case.

We can summarize the description of Fig. (6.15) as follows. For the n=1 and n=5 cases, the effective-mass enhancements of the electrons in the xy and xz/yz orbitals do not change considerably with increasing $\varepsilon_{\mathrm{CF}}$. Furthermore, $m^{*\sigma}_{xy}$ and $m^{*\sigma}_{xz/yz}$ are almost temperature-independent (except for the n=5 case at $\varepsilon_{\mathrm{CF}} \leq 0$, where $m^{*\sigma}_{xy}$ increases slightly with decreasing the temperature). For the n=2 and n=4 cases, instead, the effective-mass changes noticeably when $\varepsilon_{\mathrm{CF}}$ is varying. In particular, when the temperature decreases to room temperature the electrons become very heavy in the xz/yz channels and finally $m^{*\sigma}_{xz/yz}$ diverges at very large negative $\varepsilon_{\mathrm{CF}}$ for the n=2 case, and for very large positive $\varepsilon_{\mathrm{CF}}$ for the n=4 case. The effective-mass enhancement of the electrons in the xy and xz/yz orbitals increase when the temperature is decreasing (except for the n=4 case where $m^{*\sigma}_{xy}$ and $m^{*\sigma}_{xz/yz}$ do not change with decreasing the temperature as well as for n=2 where $m^{*\sigma}_{xy}$ is almost unchanged for very large negative $\varepsilon_{\mathrm{CF}}$). The quasi-particle scattering rate decreases when the temperature decreases in all channels and for all filling numbers. At the low temperatures the quasi-particle scattering rate

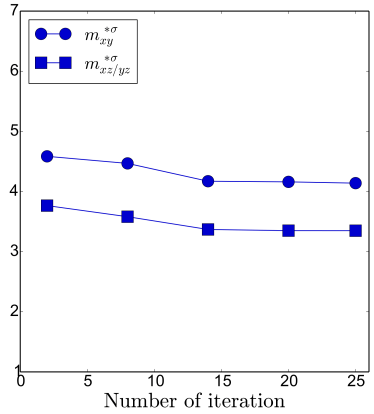


Figure 6.17: The convergence plot of the effective mass-enhancement in all channels for the n=4 case at T=193 K for $\varepsilon_{\mathrm{CF}}$=0.12 eV. The curve with circle marker shows the effective mass-enhancement in the xy channel, $m_{xy}^{*\sigma}$, and the curve with square marker presents the effective mass-enhancement in the xz/yz channels, $m_{xyz/yz}^{*\sigma}$. The horizontal axis indicates the number of performed iterations to obtain the convergence value of the quantities.

is very low. Furthermore, when the temperature decreases, the dependency of Γ_{xy}^{σ} and $\Gamma_{xz/yz}^{\sigma}$ on $\varepsilon_{\mathrm{CF}}$ becomes weak; at low temperature they are almost constant functions of $\varepsilon_{\mathrm{CF}}$.

Now let us analyze the results for the **n=3** case, shown in Fig. (6.16). In panels M_3 and M_3', $m_{xy}^{*\sigma}$ and $m_{xz/yz}^{*\sigma}$ are illustrated, respectively. Instead, Γ_{xy}^{σ} and $\Gamma_{xz/yz}^{\sigma}$ are plotted in panels Γ_3 and Γ_3'. The system is an insulator in the region which is indicated with I in the panels where m^* diverges. Since there is no carrier in the system, m^* and Γ are meaningless in this region of $\varepsilon_{\mathrm{CF}}$. The reason for the insulating behavior can be explained as follows. In that $\varepsilon_{\mathrm{CF}}$ region, the configuration of the t_{2g} orbitals is $xy^1xz^1yz^1$. Hence, each band is half-filled and the atomic gap becomes $E_g{\sim}U+2J$. Thus, the Hund's coupling effectively enhances the Coulomb repulsion energy between the electrons, leading to a gap opening.

Let us now discuss numerical details. As we already mentioned, the convergence of all quantities has to be separately checked, since it is not given that different parameters converge with the same speed. In Fig. (6.17) we show an example of the convergence plots of $m_{xy}^{*\sigma}$ and $m_{xz/yz}^{*\sigma}$. We consider the n=4 case at T=193 K for $\varepsilon_{\mathrm{CF}}$=0.12 eV. For this case, 25 iterations are sufficient to obtain accurate value. As a rule of thumb, when the temperature decreases often we need more iterations to achieve sufficiently accurate results for these

systems. This is because smaller energy scales can play role. However, the number of iterations can be reduced by starting from higher temperatures data.

6.2.4 Reduction of model size

For a free atom, the arrangement of electrons in the orbitals is determined by the Hund's rules. The first of these rules expresses that the ground state has the maximum possible total spin. However, the first Hund's rule no longer applies in the presence of a crystal-field. As was shown in panel B_1' of Fig. (6.9), for n=1, the xz/yz bands are completely empty for very large $\varepsilon_{\rm CF}>0$. In this limit, the system behaves as an effective 1-band model. In other words, the t_{2g}^1 3-band model in the very large $\varepsilon_{\rm CF}>0$ limit, is equivalent to the b_{2g}^1 (xy^1) 1-band model. The schematic diagram of the system in this limit is depicted in Fig. (6.18). In addition, for the n=5 case, a similar situ-

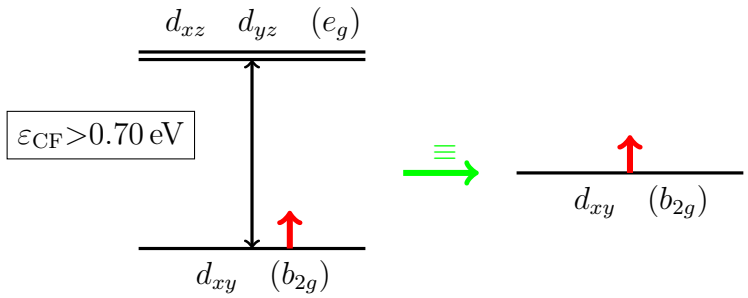


Figure 6.18: The figure shows that for the n=1 case for very large positive $\varepsilon_{\rm CF}$, $\varepsilon_{\rm CF}>0.70\,{\rm eV}$, the system can be mapped onto an 1-band model.

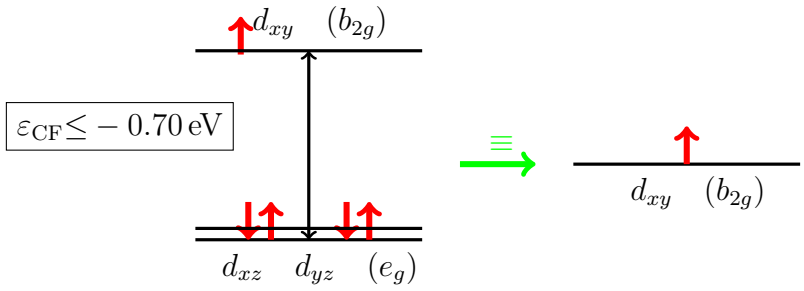


Figure 6.19: For the n=5 case, for $\varepsilon_{\rm CF}\leq -0.70\,{\rm eV}$, the xz/yz bands become completely filled. In this limit, the system can be mapped onto an 1-band model.

	b^1_{2g}	t^1_{2g}, $\varepsilon_{\rm CF}$=0.70 eV	t^5_{2g}, $\varepsilon_{\rm CF}$= − 0.70 eV
n^{σ}_{xy}	0.50	0.43	0.51
$m^{*\sigma}_{xy}$	2.45	2.00	2.51
Γ^{σ}_{xy}	0.03	0.04	0.04

Table 6.2: Comparison of the occupation number, the effective-mass enhancement and the quasi-particle scattering rate in the b^1_{2g} 1-band model with the t^1_{2g} 3-band for very large $\varepsilon_{\rm CF}$>0 and the t^5_{2g} 3-band in the very large $\varepsilon_{\rm CF}$<0 limit. The first column expresses the quantities for the b^1_{2g} model. The second column states the same quantities for the t^1_{2g} model for $\varepsilon_{\rm CF}$=0.70 eV. In this case the system, as shown in Fig. (6.18), can be mapped onto the b^1_{2g} model. In addition, the third column shows the quantities for the t^5_{2g} model for $\varepsilon_{\rm CF}$= − 0.70 eV. In this limit, the t^5_{2g} model is equivalent to the b^1_{2g} model, as depicted in Fig. (6.19).

ation occurs for very large $\varepsilon_{\rm CF}$<0 when the xz/yz bands become completely filled, as shown in panel B'_5 of Fig. (6.9). In this case, the t^5_{2g} system in the very large $\varepsilon_{\rm CF}$<0 limit can be mapped onto the b^1_{2g} model, depicted in Fig. (6.19).

In Tab. (6.2), the occupation number, the effective mass-enhancement and quasi-particle scattering rate in the b^1_{2g} model, the first column, are compared to the ones in the t^1_{2g} model for very large $\varepsilon_{\rm CF}$>0, the second column, and the t^5_{2g} model in the very large $\varepsilon_{\rm CF}$< 0 limit, the last column. The table shows that there is an excellent agreement between the quantities in the b^1_{2g} model, and the ones in the t^5_{2g} model for very large $\varepsilon_{\rm CF}$<0. However, for the t^1_{2g} model in the very large $\varepsilon_{\rm CF}$>0 limit, since the xy band is not completely half-filled, n^{σ}_{xy}≈0.43, $m^{*\sigma}_{xy}$ is slightly smaller than the one in the b^1_{2g} model. Furthermore, the behavior of the spectral function versus frequency for the t^1_{2g} and t^5_{2g} models in the limit cases and the reduced-size, b^1_{2g} model, are shown in Fig. (6.20). The spectral function of the b^1_{2g} model is the red curve, while the blue curve exhibits the spectral function of the xy band for the t^1_{2g} model at $\varepsilon_{\rm CF}$=0.70 eV and the green one for the t^5_{2g} model at $\varepsilon_{\rm CF}$= − 0.70 eV. The structure of the spectral function of the b^1_{2g} model is almost the same as the spectral function of the xy band in the t^5_{2g} model for very large $\varepsilon_{\rm CF}$<0, while for the t^1_{2g} model for very large $\varepsilon_{\rm CF}$>0 the spectral function of the xy band shows slightly different behavior. This is because, we are still not exactly at n^{σ}_{xy}=0.5. In all three cases, the spectral function exhibits the two sharp peaks at negative and positive frequencies. The height of the peaks is almost the same for the b^1_{2g} model and the t^5_{2g} model in very large $\varepsilon_{\rm CF}$<0.

Now we look at the cases which could be regarded as an effective 2-band model. For the n=4 case, the first Hund's rule is broken for very large $\varepsilon_{\rm CF}$>0.

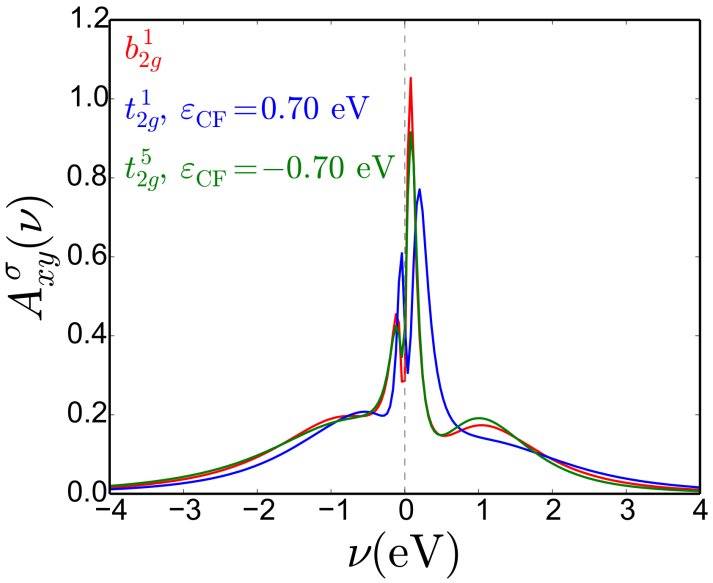


Figure 6.20: The spectral function per spin versus frequency of the b^1_{2g} 1-band model and t^n_{2g} 3-band models; n=1, 5. The red curve shows the spectral function for the b^1_{2g} 1-band model. The green curve shows the spectral function of the xy band for the t^5_{2g} 3-band for $\varepsilon_{\rm CF}=-0.70$ eV; in this limit the system is equivalent to the b^1_{2g} 1-band model, Fig. (6.19). The blue curve presents the spectral function of the xy band for the t^1_{2g} 3-band model for $\varepsilon_{\rm CF}$=0.70 eV. In this limit, the system can be mapped onto an b^1_{2g} 1-band model, Fig. (6.18). The red and green curve shows the same behavior. However, since in the t^1_{2g} 3-band model, the xy band is not completely half-filled, the behavior of the blue curve is slightly different.

Therefore, the xy band becomes completely filled and the xz/yz bands are half-filled, shown in panels B_4 and B'_4 of Fig. (6.9). In this situation, the size of the model could be reduced to an effective 2-band model ($t^4_{2g} \rightarrow e^2_g$). The schematic diagram of the system in this limit is shown in Fig. (6.21). Furthermore, for the n=5 case, in the very large $\varepsilon_{\rm CF}$>0 limit, the xy band becomes completely filled, panel B_5 of Fig. (6.9). Here, the model can be mapped onto an effective 2-band model ($t^5_{2g} \rightarrow e^3_g$), as shown in Fig. (6.22). The other case that could be considered as an effective 2-band system is the n=1 case, in the very large $\varepsilon_{\rm CF}$<0 limit. In this situation, the xy band becomes almost empty, panel B_1 of Fig. (6.9). For this case the system corresponds to the e^1_g model, as shown in Fig. (6.23). In order to check to what extent the quantities calculated from the t_{2g} models are similar to those obtained from the reduced-size 2-band models, we performed a set of DMFT calculations for the e^n_g model; n=1, 2, 3. In Tab. (6.3), the same quantities are provided for the e^2_g model and the t^4_{2g} system for very large $\varepsilon_{\rm CF}$>0. In this limit, the

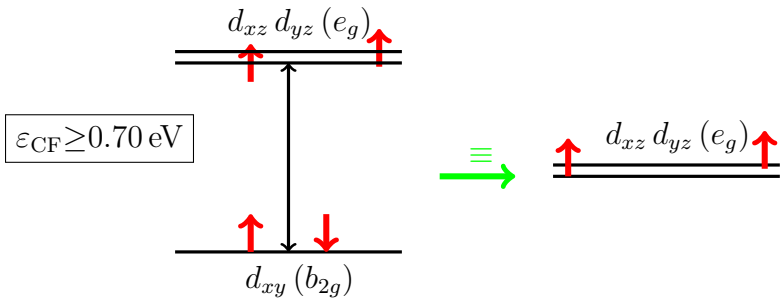


Figure 6.21: At very large positive $\varepsilon_{\mathrm{CF}}$, $\varepsilon_{\mathrm{CF}}{\geq}0.70\,\mathrm{eV}$, the xy band becomes completely filled for the n=4 case. In this limit, the system can be viewed as e_g^2 model.

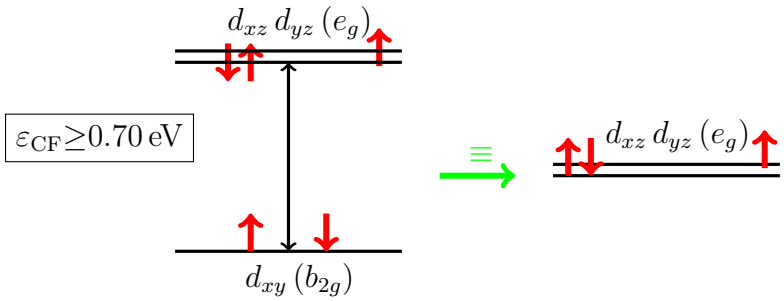


Figure 6.22: At very large positive $\varepsilon_{\mathrm{CF}}$, $\varepsilon_{\mathrm{CF}}{\geq}0.70\,\mathrm{eV}$, the xy band becomes completely filled for the n=5 case. In this limit, the system can be mapped onto a e_g^3 system.

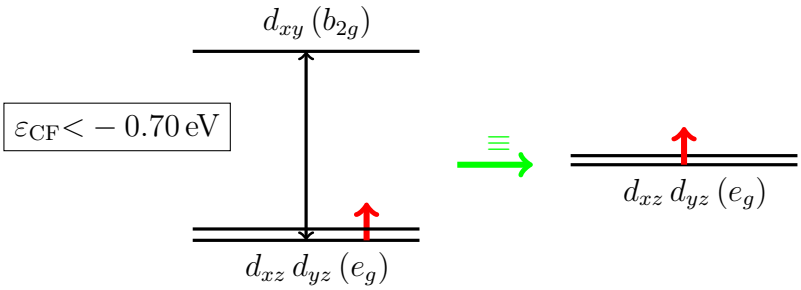


Figure 6.23: For the n=1 case at $\varepsilon_{\mathrm{CF}}{<}-0.70\,\mathrm{eV}$, the xy band becomes completely empty. In this limit, the system can be mapped onto a e_g^1 model.

	e_g^2	t_{2g}^4, $\varepsilon_{\rm CF}$=0.70 eV
$n^{\sigma}_{xz/yz}$	0.50	0.52
$m^{*\sigma}_{xz/yz}$	9.70	8.60
$\Gamma^{\sigma}_{xz/yz}$	0.05	0.07

Table 6.3: Comparison of $n^{\sigma}_{xz/yz}$, $m^{*\sigma}_{xz/yz}$ and $\Gamma^{\sigma}_{xz/yz}$ of the e_g^2 model, half-filled case, and the ones from the t_{2g}^4 model at $\varepsilon_{\rm CF}$=0.70 eV.

	e_g^3	t_{2g}^5, $\varepsilon_{\rm CF}$=0.70 eV
$n^{\sigma}_{xz/yz}$	0.75	0.75
$m^{*\sigma}_{xz/yz}$	1.96	1.84
$\Gamma^{\sigma}_{xz/yz}$	0.02	0.04

Table 6.4: Comparison of n^{σ}_{xy}, $m^{*\sigma}_{xz/yz}$ and $\Gamma^{\sigma}_{xz/yz}$ of the e_g^3 model, and the ones from the t_{2g}^5 model at $\varepsilon_{\rm CF}$=0.70 eV.

	e_g^1	t_{2g}^1, $\varepsilon_{\rm CF}$= − 0.70 eV
$n^{\sigma}_{xz/yz}$	0.25	0.21
$m^{*\sigma}_{xz/yz}$	2.43	2.09
$\Gamma^{\sigma}_{xz/yz}$	0.03	0.04

Table 6.5: The occupation number, the effective-mass enhancement and quasi-particle scattering rate of the e_g^1 model, the first column, and t_{2g}^1 system at $\varepsilon_{\rm CF}$= − 0.70 eV, the second column.

models are half-filled, therefore $m^{*\sigma}_{xz/yz}$ diverges. In Tab. (6.4) the results are illustrated for the e_g^3 model and for the t_{2g}^5 in the very large $\varepsilon_{\rm CF}$>0 limit. In both models, $n^{\sigma}_{xz/yz}$≈0.75, and $m^{*\sigma}_{xz/yz}$ and $\Gamma^{\sigma}_{xz/yz}$ are almost the same. In Tab. (6.5), $n^{\sigma}_{xz/yz}$, $m^{*\sigma}_{xz/yz}$ and $\Gamma^{\sigma}_{xz/yz}$ are given for the e_g^1 model and the equivalent t_{2g}^1 system. The xz/yz bands are more occupied and $m^{*\sigma}_{xz/yz}$ is slightly larger in the e_g^1 model, while $\Gamma^{\sigma}_{xz/yz}$ is almost the same in the two cases.
Now we compare the behavior of the spectral functions which are presented in Fig. (6.24). In all panels of the figure, the red curves show $A^{\sigma}_{xz/yz}(\nu)$ of the reduced-size 2-band model and the blue curves present $A^{\sigma}_{xz/yz}(\nu)$ of the equivalent t_{2g}^n system. In the first panel, $A^{\sigma}_{xz/yz}(\nu)$ of the e_g^1 and t_{2g}^1 in the very large $\varepsilon_{\rm CF}$<0 limit are plotted. The results show that $A^{\sigma}_{xz/yz}(\nu)$ for both cases is almost the same; $A^{\sigma}_{xz/yz}$ shows a sharp peak at the zero frequency energy. The middle panel presents the behavior of $A^{\sigma}_{xz/yz}(\nu)$ of the t_{2g}^4 model for very large $\varepsilon_{\rm CF}$>0 and the e_g^2 system. In this case the behavior of $A^{\sigma}_{xz/yz}(\nu)$

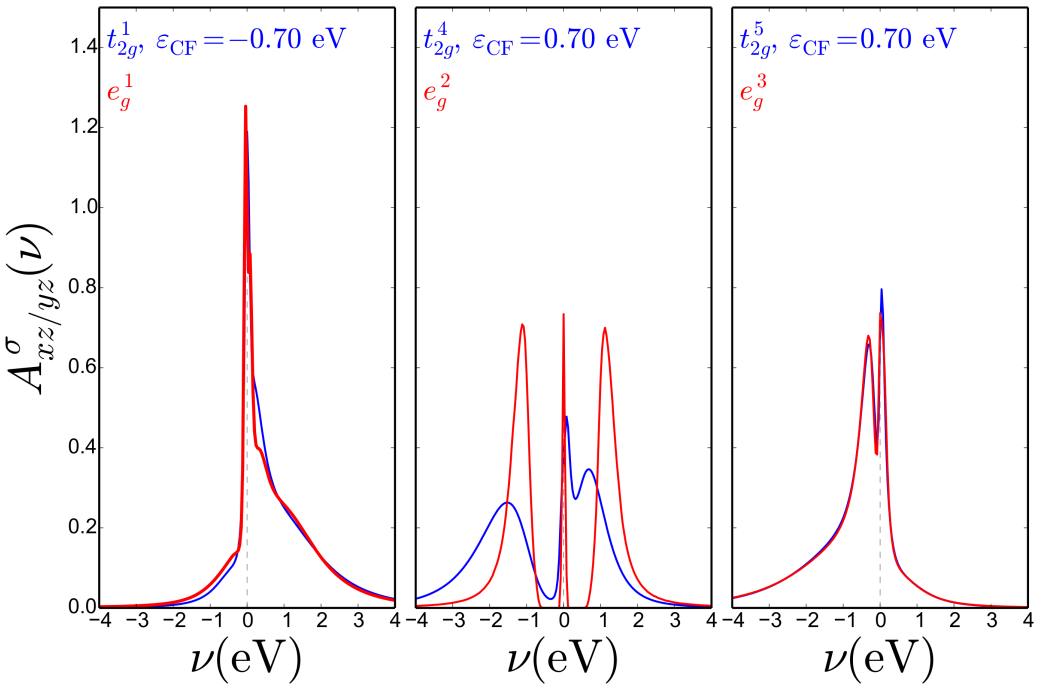


Figure 6.24: The behavior of the spectral function per spin of the xz/yz bands, $A^{\sigma}_{xz/yz}(\nu)$, for the e_g^n model and equivalent cases in the t_{2g}^n system; n=1, 2, 3. In each panel, the blue curve shows $A^{\sigma}_{xz/yz}(\nu)$ for the t_{2g}^n 3-band model while the red curve presents $A^{\sigma}_{xz/yz}(\nu)$ for the e_g^n 2-band system. In the first panel, $A^{\sigma}_{xz/yz}(\nu)$ is presented for the t_{2g}^1 system for $\varepsilon_{\rm CF}=-0.70$ eV and the e_g^1 model. The middle panel shows $A^{\sigma}_{xz/yz}(\nu)$ for the t_{2g}^4 model for $\varepsilon_{\rm CF}$=0.70 eV and e_g^2 system. In the last column, $A^{\sigma}_{xz/yz}(\nu)$ for the t_{2g}^5 model for $\varepsilon_{\rm CF}$=0.70 eV and the e_g^3 model are compared.

is not the same, since they have slightly different occupation numbers. The red curve exhibits three sharp peaks: at the Hubbard bands and one at the zero frequency, while the height of the peaks in the blue curve are smaller. The third column of the figure presents the behavior of $A^{\sigma}_{xz/yz}(\nu)$ of the t_{2g}^5 model for very large $\varepsilon_{\rm CF}>0$ and the e_g^3 model. The structure of the spectral function for these two cases is almost the same; $A^{\sigma}_{xz/yz}(\nu)$ shows two sharp peaks one at the negative frequency and the other on at the zero frequency.

6.2.5 Crystal-field splitting correction

In multi-orbital systems, many-body effects effectively change $\varepsilon_{\rm CF}$. The correction of $\varepsilon_{\rm CF}$ at Matsubara frequency $i\nu_n$, $\Delta^\sigma\varepsilon_{\rm CF}(i\nu_n)$, is defined as

$$\Delta^\sigma\varepsilon_{\rm CF}(i\nu_n) = \frac{1}{2}\left[\mathbf{Re}\,\Sigma^\sigma_{xz}(i\nu_n) + \mathbf{Re}\,\Sigma^\sigma_{yz}(i\nu_n)\right] - \mathbf{Re}\,\Sigma^\sigma_{xy}(i\nu_n). \tag{6.10}$$

Thus, the zero frequency correction of $\varepsilon_{\rm CF}$ per spin, $\Delta^\sigma\varepsilon_{\rm CF}(0)$, is given by

$$\begin{aligned}\Delta^\sigma\varepsilon_{\rm CF}(0) &\approx \Delta\mathbf{Re}\,\Sigma^\sigma(i\nu_0) \\ &= \frac{1}{2}\left[\mathbf{Re}\,\Sigma^\sigma_{xz}(i\nu_0) + \mathbf{Re}\,\Sigma^\sigma_{yz}(i\nu_0)\right] - \mathbf{Re}\,\Sigma^\sigma_{xy}(i\nu_0).\end{aligned} \tag{6.11}$$

Using the Hilbert transform, the self-energy on the Matsubara axis can be obtained from the self-energy on the real axis

$$\Sigma(i\nu_0) \approx \Sigma(\infty) + \frac{1}{\pi}\mathcal{P}\int_{-\infty}^{+\infty} d\nu\,\frac{\mathbf{Im}\,\Sigma(\nu)}{\nu}, \tag{6.12}$$

where $\mathcal{P}$ is the Cauchy principal value, defined in Appendix A. The self-energy in the high frequency limit, $\Sigma(\infty)$, becomes a frequency-independent constant. In fact, this constant is the result one could obtain in the static mean-field Hartree-Fock (HF) approximation. Therefore, using Eq. (A.5), in Appendix A, the zero frequency $\varepsilon_{\rm CF}$ correction, $\Delta\varepsilon_{\rm CF}(0)$, is given by

$$\Delta\mathbf{Re}\,\Sigma(i\nu_0) \approx \Delta\varepsilon_{\rm CF}(0) = \Delta\Sigma_{\rm HF} + \frac{1}{\pi}\mathcal{P}\int_{-\infty}^{+\infty} d\nu\,\frac{\Delta\mathbf{Im}\,\Sigma(\nu)}{\nu}, \tag{6.13}$$

where $\Delta\mathbf{Im}\,\Sigma(\nu) = \frac{1}{2}\left(\mathbf{Im}\,\Sigma_{yz}(\nu) + \mathbf{Im}\,\Sigma_{xz}(\nu)\right) - \mathbf{Im}\,\Sigma_{xy}(\nu)$. As shown in Eq. (6.13), $\Delta\varepsilon_{\rm CF}(0)$ is divided into a static part, coming from the HF approximation, and a dynamic part related to the imaginary part of the self-energy.

In the HF approximation, we assume that

$$\begin{aligned}
\hat{H}_U^{\mathrm{HF}} &= U\sum_m \left(\hat{n}_{m\uparrow}\overline{n}_{m\downarrow} + \overline{n}_{m\uparrow}\hat{n}_{m\downarrow} - \overline{n}_{m\uparrow}\overline{n}_{m\downarrow}\right) \\
&+ \frac{1}{2}\sum_{\substack{m\neq m'\\ \sigma}} (U-3J)\left(\hat{n}_{m\sigma}\overline{n}_{m'\sigma} + \overline{n}_{m\sigma}\hat{n}_{m'\sigma} - \overline{n}_{m\sigma}\overline{n}_{m'\sigma}\right) \\
&+ \frac{1}{2}\sum_{\substack{m\neq m'\\ \sigma\neq\sigma'}} (U-2J)\left(\hat{n}_{m\sigma}\overline{n}_{m'\sigma'} + \overline{n}_{m\sigma}\hat{n}_{m'\sigma'} - \overline{n}_{m\sigma}\overline{n}_{m'\sigma'}\right) \\
&- J\sum_{m\neq m'} \left[c^\dagger_{m'\downarrow}c_{m\downarrow}\langle c^\dagger_{m\uparrow}c_{m'\uparrow}\rangle + c^\dagger_{m\uparrow}c_{m'\uparrow}\langle c^\dagger_{m'\downarrow}c_{m\downarrow}\rangle - \langle c^\dagger_{m\uparrow}c_{m'\uparrow}\rangle\langle c^\dagger_{m'\downarrow}c_{m\downarrow}\rangle\right] \\
&+ J\sum_{m\neq m'} \left[c^\dagger_{m'\downarrow}c_{m'\uparrow}\langle c^\dagger_{m\uparrow}c_{m\downarrow}\rangle + c^\dagger_{m\uparrow}c_{m\downarrow}\langle c^\dagger_{m'\downarrow}c_{m'\uparrow}\rangle - \langle c^\dagger_{m'\downarrow}c_{m'\uparrow}\rangle\langle c^\dagger_{m\uparrow}c_{m\downarrow}\rangle\right] \\
&- J\sum_{m\neq m'} \left[c^\dagger_{m\downarrow}c_{m'\downarrow}\langle c^\dagger_{m\uparrow}c_{m'\uparrow}\rangle + c^\dagger_{m\uparrow}c_{m'\uparrow}\langle c^\dagger_{m\downarrow}c_{m'\downarrow}\rangle - \langle c^\dagger_{m\uparrow}c_{m'\uparrow}\rangle\langle c^\dagger_{m\downarrow}c_{m'\downarrow}\rangle\right] \\
&+ J\sum_{m\neq m'} \left[c^\dagger_{m\downarrow}c_{m'\uparrow}\langle c^\dagger_{m\uparrow}c_{m'\downarrow}\rangle + c^\dagger_{m\uparrow}c_{m'\downarrow}\langle c^\dagger_{m\downarrow}c_{m'\uparrow}\rangle - \langle c^\dagger_{m\downarrow}c_{m'\uparrow}\rangle\langle c^\dagger_{m\uparrow}c_{m'\downarrow}\rangle\right],
\end{aligned} \tag{6.14}$$

where, $\overline{n}_{m\sigma}$ is the HF expectation value of the operator $\hat{n}_{m\sigma}$, $\overline{n}_{m\sigma} = \langle\hat{n}_{m\sigma}\rangle$. Since the Hamiltonian does not mix spins, the on-site energy of the electrons in each band is modified as

$$\begin{aligned}
\varepsilon^\sigma_{xy} &\rightarrow \varepsilon^\sigma_{xy} + (U-3J)(\overline{n}_{xz\sigma} + \overline{n}_{yz\sigma}) + (U-2J)(\overline{n}_{xz\sigma'} + \overline{n}_{yz\sigma'}) \\
&+ U\overline{n}_{xy\sigma'}
\end{aligned} \tag{6.15}$$

$$\begin{aligned}
\varepsilon^\sigma_{xz} &\rightarrow \varepsilon^\sigma_{xz} + (U-3J)(\overline{n}_{xy\sigma} + \overline{n}_{yz\sigma}) + (U-2J)(\overline{n}_{xy\sigma'} + \overline{n}_{yz\sigma'}) \\
&+ U\overline{n}_{xz\sigma'}
\end{aligned} \tag{6.16}$$

Consequently, the HF approximation leads to an effective shift of the on-site parameters: $\varepsilon_{\mathrm{CF}} \rightarrow \varepsilon_{\mathrm{CF}} + \Delta^\sigma\varepsilon_{\mathrm{CF}}(\infty)$,

$$\Delta^\sigma\varepsilon_{\mathrm{CF}}(\infty) = \Delta\Sigma^\sigma_{\mathrm{HF}} = (U-5J)\,p^\sigma, \tag{6.17}$$

where p^σ is the polarization as it is defined in Eq. (6.6). The value of $\Delta^\sigma\varepsilon_{\mathrm{CF}}(\infty)$ can be obtained from the numerical data at high frequency,

$$\Delta^\sigma\varepsilon_{\mathrm{CF}}(\infty) = \frac{1}{2}\left[\mathbf{Re}\Sigma^\sigma_{xz}(\infty) + \mathbf{Re}\Sigma^\sigma_{yz}(\infty)\right] - \mathbf{Re}\Sigma^\sigma_{xy}(\infty). \tag{6.18}$$

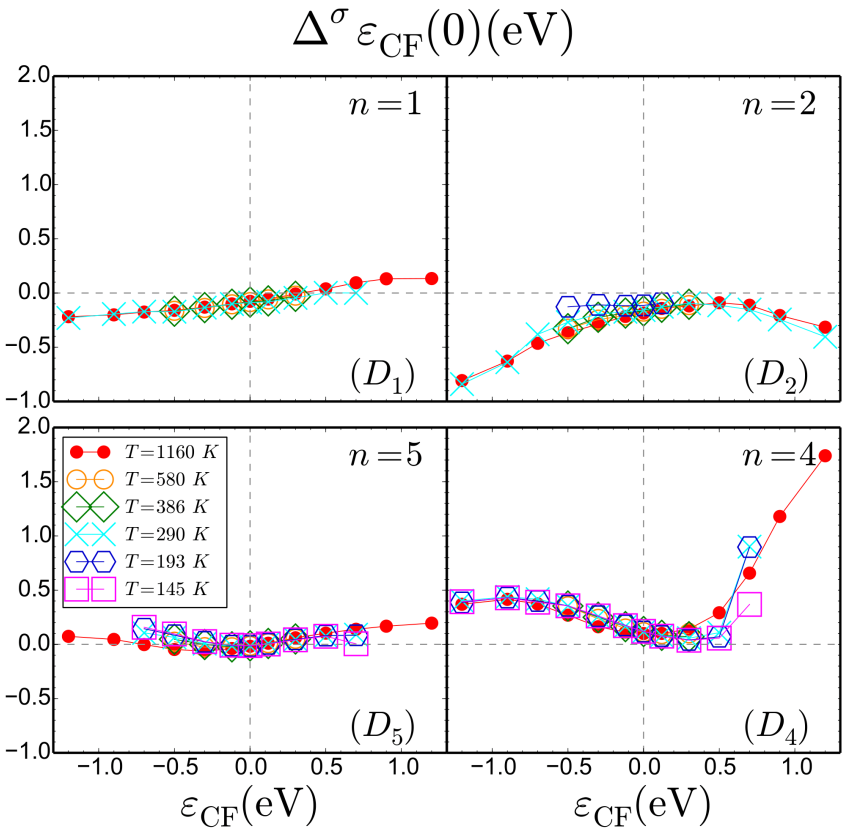


Figure 6.25: Evolution of the zero frequency correction of $\varepsilon_{\rm CF}$ per spin, $\Delta^\sigma\varepsilon_{\rm CF}(0)$, with increasing $\varepsilon_{\rm CF}$. The results are presented for the four integer filling numbers, n=1, 2, 4, 5, which are shown in panels D_n. In each panel, different curves represent the results for different temperatures. The vertical gray dashed line corresponds to $\varepsilon_{\rm CF}$=0 and the horizontal one shows $\Delta^\sigma\varepsilon_{\rm CF}(0)$=0.

Comparing these two values for $\Delta^\sigma\varepsilon_{\rm CF}(\infty)$, one from HF approximation, Eq. (6.17), and the other one from the numerical data, is a check of the accuracy of our numerical results.

Firstly, let us study the behavior of $\Delta^\sigma\varepsilon_{\rm CF}(0)$ with increasing $\varepsilon_{\rm CF}$ at different temperatures. At the first we look at the results for the n=1, 2, 4, 5 cases and later the analysis for n=3 will be presented. The evolution of $\Delta^\sigma\varepsilon_{\rm CF}(0)$ with increasing $\varepsilon_{\rm CF}$ is shown in Fig. (6.25). The results for different filling numbers are presented in panels D_n. In each panel, different temperatures are shown by different colors and markers. The horizontal gray dashed line represents $\Delta^\sigma\varepsilon_{\rm CF}(0)$=0, while the vertical one corresponds to $\varepsilon_{\rm CF}$=0.

First of all, the results are weakly temperature-dependent. Thus, in the

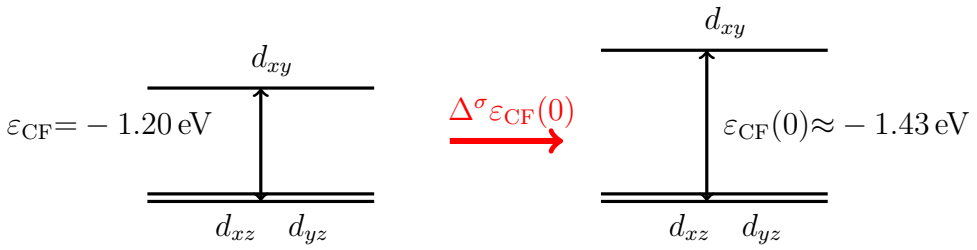


Figure 6.26: The many-body effects at zero frequency change $\varepsilon_{\rm CF}$ to $\varepsilon_{\rm CF}\rightarrow\varepsilon_{\rm CF}+\Delta^\sigma\varepsilon_{\rm CF}(0)$. The figure shows that for the n=1 case at T=290 K for $\varepsilon_{\rm CF}=-1.20\,{\rm eV}$, the many-body effects enhance $\varepsilon_{\rm CF}$, $\varepsilon_{\rm CF}\approx-1.43\,{\rm eV}$ where the enhancement is $\Delta^\sigma\varepsilon_{\rm CF}(0)\approx-0.23\,{\rm eV}$.

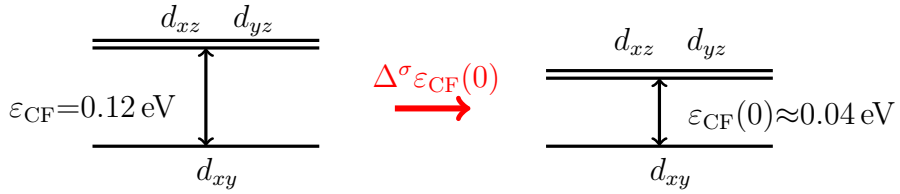


Figure 6.27: The many-body effects at zero frequency change $\varepsilon_{\rm CF}$ to $\varepsilon_{\rm CF}\rightarrow\varepsilon_{\rm CF}+\Delta^\sigma\varepsilon_{\rm CF}(0)$. The figure shows that when the filling number is n=1 at T=290 K for $\varepsilon_{\rm CF}$=0.12 eV, the many-body effects reduce $\varepsilon_{\rm CF}$ to $\varepsilon_{\rm CF}\approx$0.04 eV where the reduction in $\varepsilon_{\rm CF}$ is almost $\Delta^\sigma\varepsilon_{\rm CF}(0)\approx-0.08\,{\rm eV}$. As drawn, the reduction is not large enough to rearrange the orbitals arrangement.

following we look at the behavior of $\Delta^\sigma\varepsilon_{\rm CF}(0)$ with increasing $\varepsilon_{\rm CF}$.
Firstly let us analyze the results for the **n=1** case. As depicted in panel D_1, $\Delta^\sigma\varepsilon_{\rm CF}(0)$ increases monotonically when $\varepsilon_{\rm CF}$ increases. For $\varepsilon_{\rm CF}<0$, we see that $\Delta^\sigma\varepsilon_{\rm CF}(0)<0$. This means that the many-body effects at zero frequency enhances $\varepsilon_{\rm CF}$; an example of such $\varepsilon_{\rm CF}$ enhancement is shown in Fig. (6.26). Enhancing $\varepsilon_{\rm CF}$ corresponds to slightly moving the xy band downwards and the xz/yz bands upwards with respect to the Fermi level. For small positive $\varepsilon_{\rm CF}$, $\Delta^\sigma\varepsilon_{\rm CF}(0)<0$, hence $\varepsilon_{\rm CF}$ is reduced, as depicted in Fig. (6.27). In this situation, the xy and xz/yz bands shift toward the Fermi level. Furthermore, the figure shows that for large $\varepsilon_{\rm CF}>0$, $\varepsilon_{\rm CF}$ is enhanced once more.
Next, we investigate the **n=2** case. As illustrated in panel D_2, for all values of $\varepsilon_{\rm CF}$, $\Delta^\sigma\varepsilon_{\rm CF}(0)<0$. This indicates that $\varepsilon_{\rm CF}$ is enhanced for $\varepsilon_{\rm CF}<0$, while for $\varepsilon_{\rm CF}>0$ the many-body effects at zero frequency reduce $\varepsilon_{\rm CF}$. The reduction and the enhancement of $\varepsilon_{\rm CF}$, increases with $|\varepsilon_{\rm CF}|$. In particular, for very small $\varepsilon_{\rm CF}>0$, the reduction is high enough to reverse the orbitals arrangement as depicted in Fig. (6.28), or turns the system into effectively almost three-fold degenerate one, Fig. (6.29).

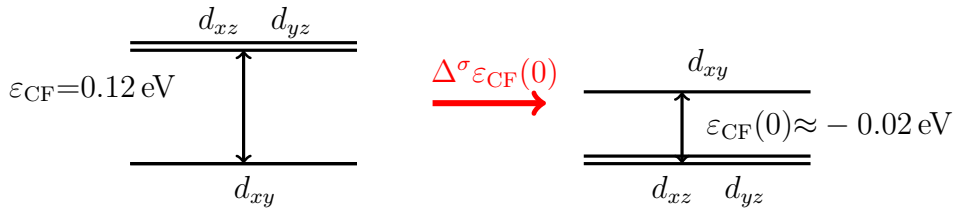


Figure 6.28: The many-body effects at zero frequency change $\varepsilon_{\rm CF}$ to $\varepsilon_{\rm CF} \rightarrow \varepsilon_{\rm CF} + \Delta^\sigma\varepsilon_{\rm CF}(0) \equiv \varepsilon_{\rm CF}(0)$. The figure shows that when the filling number is n=2, at T=1160 K, for $\varepsilon_{\rm CF}$=0.12 eV, the many-body effects reduce $\varepsilon_{\rm CF}$ to $\varepsilon_{\rm CF}\approx -0.02$ eV, where the reduction in $\varepsilon_{\rm CF}$ is almost $\Delta^\sigma\varepsilon_{\rm CF}(0)\approx -0.14$ eV. As drawn, the reduction is large enough to rearrange the orbitals arrangement and turns the positive $\varepsilon_{\rm CF}$ into negative one.

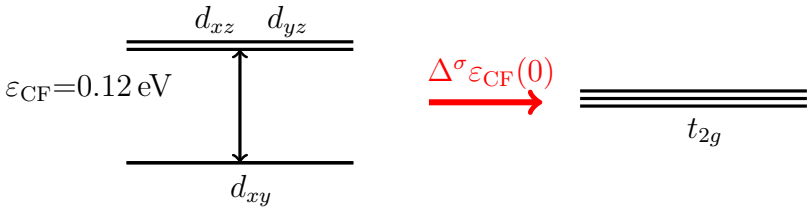


Figure 6.29: The many-body effects at zero frequency change $\varepsilon_{\rm CF}$ to $\varepsilon_{\rm CF} \rightarrow \varepsilon_{\rm CF} + \Delta^\sigma\varepsilon_{\rm CF}(0) \equiv \varepsilon_{\rm CF}(0)$. The figure shows that when the filling number is n=2 at T=290 K for $\varepsilon_{\rm CF}$=0.12 eV, the many-body effects reduce $\varepsilon_{\rm CF}$ at zero frequency, $\varepsilon_{\rm CF}(0)$, to $\varepsilon_{\rm CF}(0)\approx 0$ where the reduction in $\varepsilon_{\rm CF}$ is almost $\Delta^\sigma\varepsilon_{\rm CF}(0)\approx -0.12$ eV. As drawn, the reduction changes the orbitals arrangement that the final arrangement becomes effectively a three-fold degenerate system.

Then we look at the behavior of $\Delta^\sigma\varepsilon_{\rm CF}(0)$, for **n=4**. As plotted in panel D_4, $\Delta^\sigma\varepsilon_{\rm CF}(0)$ is positive for all values of $\varepsilon_{\rm CF}$. Therefore, $\varepsilon_{\rm CF}$ is enhanced for $\varepsilon_{\rm CF}>0$, while it is reduced for $\varepsilon_{\rm CF}<0$. For very small $\varepsilon_{\rm CF}<0$, the reduction leads to the rearrangement of the orbitals.

Finally, we consider the results for **n=5**. As presented in panel D_5, the many-body effects at zero frequency do not change $\varepsilon_{\rm CF}$ considerably, except at very large $\varepsilon_{\rm CF}>0$ where $\varepsilon_{\rm CF}$ is enhanced slightly.

In the $\varepsilon_{\rm CF}$=0 case, for all values of the filling number, we find that the many-body effects at zero frequency, split the levels. The arrangement of the states depends on the filling number. For the n=1, 2, 5 cases, since $\Delta^\sigma\varepsilon_{\rm CF}(0)<0$, the xy band is higher in energy with respect to the xz/yz bands. However, for the n=4 case, $\Delta^\sigma\varepsilon_{\rm CF}(0)>0$.

In order to investigate the many-body effects on $\varepsilon_{\rm CF}$ in the high frequency limit, let us look at the results for $\Delta^\sigma\varepsilon_{\rm CF}(\infty)$, presented in Fig. (6.30). The first row of the figure shows the results for the n=1 case, the second one for the n=5 case, the third one for the n=2 case and the fourth one for n=4. In

each panel, the results for different temperatures are plotted with different colors and markers. The vertical gray dashed line shows $\varepsilon_{\rm CF}$=0 and the horizontal one corresponds to $\Delta^\sigma\varepsilon_{\rm CF}(\infty)$=0. The results in the left panels, E_1, E_2, E_4 and E_5, are extracted from the numerical data, Eq. (6.18), while the right panels, E_1', E_2', E_4' and E_5', show the behavior of $\Delta^\sigma\varepsilon_{\rm CF}(\infty)$ with increasing $\varepsilon_{\rm CF}$ that are obtained from the HF approximation, Eq. (6.17). In our calculation, the direct Coulomb parameter, U, and the exchange Coulomb parameter, J, are U=2.3 eV and J=0.4 eV. Therefore, using Eq. (6.17), one can obtain

$$\Delta^\sigma\varepsilon_{\rm CF}(\infty) = 0.3\,p^\sigma \text{ eV}. \tag{6.19}$$

As it was shown in sub-section (6.2.2), the polarization, p^σ, is a temperature-independent quantity for all presented filling numbers. Therefore, based on Eq. (6.19), $\Delta^\sigma\varepsilon_{\rm CF}(\infty)$ is a temperature-independent quantity too. In addition, $\Delta^\sigma\varepsilon_{\rm CF}(\infty)$ corresponds to zero for the values of $\varepsilon_{\rm CF}$ where $p^\sigma\approx$0.
Thus, for these cases only the dynamical part of the many-body effects has contribution on the change in $\varepsilon_{\rm CF}$.
For $\varepsilon_{\rm CF}$=0, the effective $\varepsilon_{\rm CF}$ is finite; for the **n=1** case, $\Delta^\sigma\varepsilon_{\rm CF}(\infty)>0$, while for the **n=2**, **n=4** and **n=5** cases, $\Delta^\sigma\varepsilon_{\rm CF}(\infty)<0$. For the other values of $\varepsilon_{\rm CF}$, the many-body effects at high frequency enhances $\varepsilon_{\rm CF}$; the enhancement becomes larger at large $|\varepsilon_{\rm CF}|$.
In order to figure out which part of the many-body effects has more contribution to $\Delta^\sigma\varepsilon_{\rm CF}(0)$, the static part, $\Delta^\sigma\varepsilon_{\rm CF}(\infty)$, and the dynamic part,

$$\Delta^{D\sigma}\varepsilon_{\rm CF} \equiv \Delta^\sigma\varepsilon_{\rm CF}(0) - \Delta^\sigma\varepsilon_{\rm CF}(\infty) = \frac{1}{\pi}\mathcal{P}\int_{-\infty}^{+\infty} d\nu\,\frac{\Delta\mathbf{Im}\,\Sigma(\nu)}{\nu}, \tag{6.20}$$

are plotted in Fig. (6.31). The first column of the figure shows the behavior of $\Delta^\sigma\varepsilon_{\rm CF}(0)$, the second one of $\Delta^\sigma\varepsilon_{\rm CF}(\infty)$, and the third one of $\Delta^{D\sigma}\varepsilon_{\rm CF}$, while the first row presents the results for the n=1 case, the second one for n=5, the third one for n=2, and the fourth one for n=4. The vertical gray dashed line corresponds to $\varepsilon_{\rm CF}$=0 in all panels, while the horizontal gray dashed line in the left panels, D_1, D_2, D_4 and D_5 panels, represents $\Delta^\sigma\varepsilon_{\rm CF}(0)$=0, in the middle panels, E_1', E_2', E_4' and E_5', shows $\Delta^\sigma\varepsilon_{\rm CF}(\infty)$=0 and in the right panels, F_1, F_2, F_4 and F_5, corresponds to $\Delta^{D\sigma}\varepsilon_{\rm CF}$=0.
First of all, since $\Delta^\sigma\varepsilon_{\rm CF}(\infty)$ is almost temperature-independent, the weakly temperature dependence of $\Delta^\sigma\varepsilon_{\rm CF}(0)$ originates from the dynamical part of the many-body effects.
For the **n=1** case, as shown in panels E_1' and F_1, the contribution of the dynamical part is slightly larger than the static part of the many-body effects,

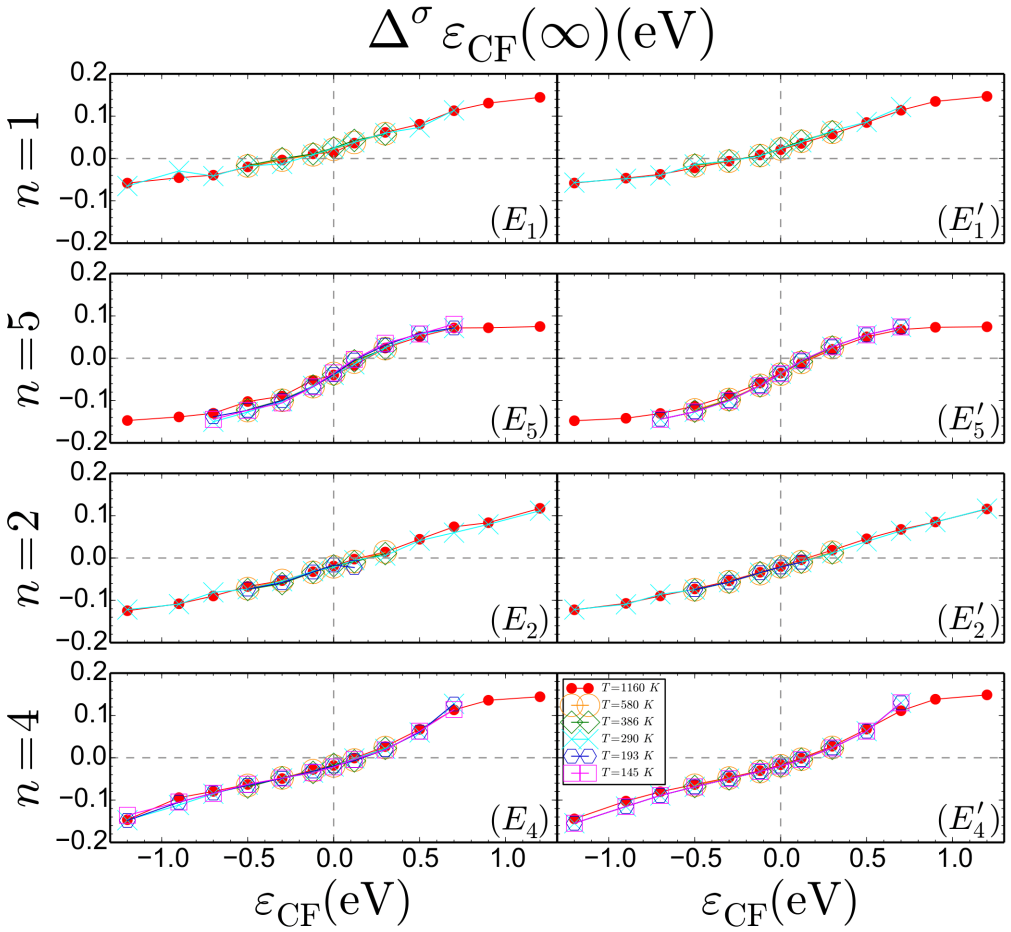


Figure 6.30: The behavior of $\Delta^\sigma \varepsilon_{\rm CF}(\infty)$ with increasing $\varepsilon_{\rm CF}$. The results are obtained for four integer filling numbers, n=1, 2, 4, 5. In each panel, different curves represent the results for different temperatures, which are shown in the legend of panel E_4'. The vertical gray dashed line corresponds to $\varepsilon_{\rm CF}$=0 and the horizontal one to $\Delta^\sigma \varepsilon_{\rm CF}(\infty)$=0. The first column presents the results which are extracted from the numerical data, Eq. (6.18), and the second column shows $\Delta^\sigma \varepsilon_{\rm CF}(\infty)$ which are obtained from the HF approximation, Eq. (6.17). The first row presents the results for the n=1 case, the second one for the n=5 case, while the third row shows for the n=2 case and the fourth one for the n=4 case.

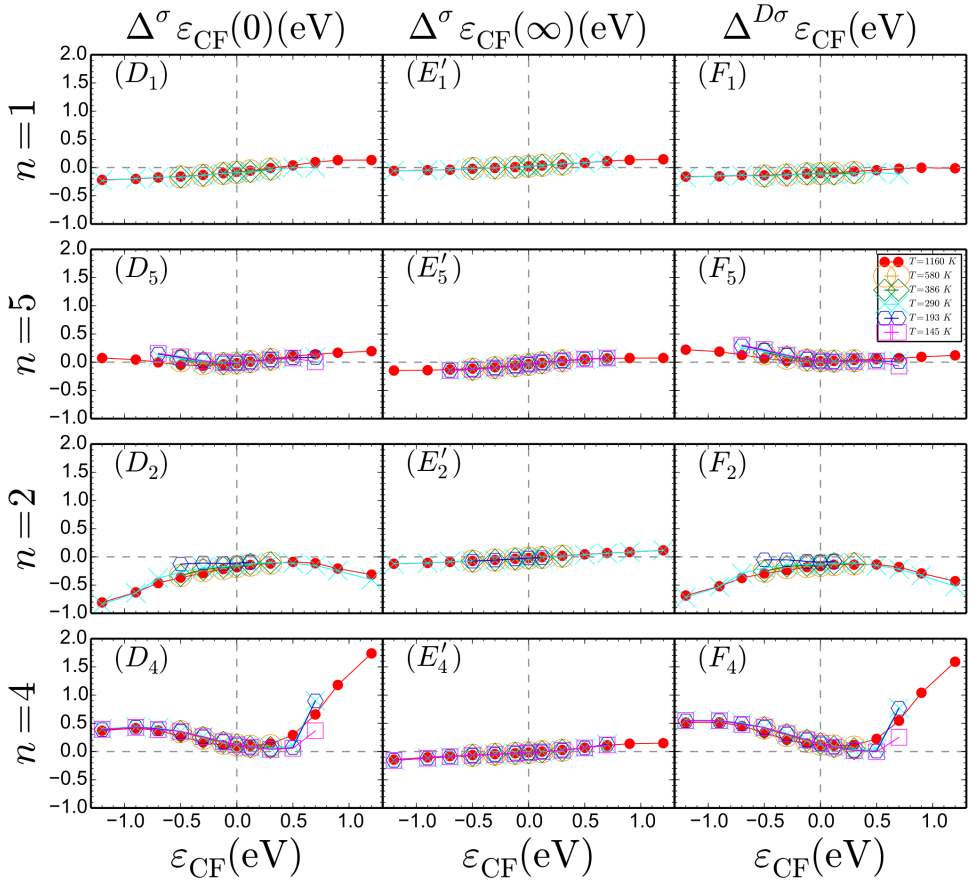


Figure 6.31: Evolution of the zero frequency $\varepsilon_{\rm CF}$ correction, $\Delta^{\sigma}\varepsilon_{\rm CF}(0)$ (the first column), the high frequency $\varepsilon_{\rm CF}$ correction $\Delta^{\sigma}\varepsilon_{\rm CF}(\infty)$ (the second column), and $\Delta^{D\sigma}\varepsilon_{\rm CF}$ (third column), with increasing $\varepsilon_{\rm CF}$. The first row presents the results for the n=1 case, the second one for n=5, the third one for n=2 and the fourth one for the n=4 case. Panels D_n show $\Delta^{\sigma}\varepsilon_{\rm CF}(0)$, E'_n present $\Delta^{\sigma}\varepsilon_{\rm CF}(\infty)$ and F_n show $\Delta^{D\sigma}\varepsilon_{\rm CF}$ where n is the introduced filling number. In each panel, different curves represent the results for different temperatures which are shown in the legend of panel F_5. The vertical gray dashed line corresponds to $\varepsilon_{\rm CF}$=0, while the horizontal gray dashed line in D_n panels corresponds to $\Delta^{\sigma}\varepsilon_{\rm CF}(0)$=0 , in E_n panels indicates $\Delta^{\sigma}\varepsilon_{\rm CF}(\infty)$=0 and in F_n panels shows $\Delta^{D\sigma}\varepsilon_{\rm CF}$=0.

except at very large $\varepsilon_{\rm CF}>0$. In this limit, $|\Delta^{D\sigma}\varepsilon_{\rm CF}|\approx 0$, and $\Delta^{\sigma}\varepsilon_{\rm CF}(0)$ comes from the static part of the many-body effects.
Next, we consider the $\mathbf{n=2}$ case. As shown in panels E_2' and F_2, for $\varepsilon_{\rm CF}<0$, both terms lead to an enhancement of $\varepsilon_{\rm CF}$, but the dynamical part has a larger contribution. For $\varepsilon_{\rm CF}>0$, on the one hand $\Delta^{D\sigma}\varepsilon_{\rm CF}<0$. On the other hand, $\Delta^{\sigma}\varepsilon_{\rm CF}(\infty)>0$ and since $|\Delta^{D\sigma}\varepsilon_{\rm CF}|\gg|\Delta^{\sigma}\varepsilon_{\rm CF}(\infty)|$, at zero frequency $\varepsilon_{\rm CF}$ is reduced.
Then, we consider $\mathbf{n=4}$. For $\varepsilon_{\rm CF}<0$, $\Delta^{\sigma}\varepsilon_{\rm CF}(\infty)<0$, while $\Delta^{D\sigma}\varepsilon_{\rm CF}>0$, and since $|\Delta^{D\sigma}\varepsilon_{\rm CF}|>|\Delta^{\sigma}\varepsilon_{\rm CF}(\infty)|$, $\varepsilon_{\rm CF}$ is reduced. However, for very large $\varepsilon_{\rm CF}>0$, the dynamical part has larger contribution to the enhancement of $\varepsilon_{\rm CF}$.
Finally, for $\mathbf{n=5}$, for $\varepsilon_{\rm CF}<0$, the static and dynamic parts of the many- body effects weaken each other. However, for $\varepsilon_{\rm CF}>0$, they reinforce each other.
We find that for large $|\varepsilon_{\rm CF}|$, for the $n=2,4$ cases, $\Delta^{D\sigma}\varepsilon_{\rm CF}$ is $\sim 1\,\text{eV}$ larger than $\Delta^{\sigma}\varepsilon_{\rm CF}(\infty)$. As a consequence, the dynamical part of the many-body effects is an essential ingredient. Now we consider the many-body effects on $\varepsilon_{\rm CF}$ for the $n=3$ case. The results are shown at $T=1160\,\text{K}$ in Fig. (6.32), where the vertical gray dashed line in each panel represents $\varepsilon_{\rm CF}=0$. The first column in the figure, panel D_3, shows the behavior of $\Delta^{\sigma}\varepsilon_{\rm CF}(0)$, where the horizontal gray dashed line indicates $\Delta^{\sigma}\varepsilon_{\rm CF}(0)=0$. The second column, panel E_3, presents $\Delta^{\sigma}\varepsilon_{\rm CF}(\infty)$; the filled circle markers come from the HF approximation, Eq. (6.17), while the empty diamond markers are extracted from the numerical data, Eq. (6.18) and the horizontal gray dashed line corresponds to $\Delta^{\sigma}\varepsilon_{\rm CF}(\infty)=0$. The last column, panel F_3, shows the behavior of $\Delta^{D\sigma}\varepsilon_{\rm CF}$ with increasing $\varepsilon_{\rm CF}$. First of all, the figure proofs the numerical accuracy. Furthermore, $\Delta^{\sigma}\varepsilon_{\rm CF}(\infty)\approx 0$, except for very large $|\varepsilon_{\rm CF}|$. In addition, $\Delta^{\sigma}\varepsilon_{\rm CF}(0)$ becomes very large for any $\varepsilon_{\rm CF}$, which is mainly the effect of the dynamical part of the many-body effects.
We can summarize the discussion of this section as follows. The results show that the static part of $\Delta^{\sigma}\varepsilon_{\rm CF}(0)$ always enhances $\varepsilon_{\rm CF}$ and is almost temperature-independent. However, $\Delta^{\sigma}\varepsilon_{\rm CF}(0)$ shows a weak dependency on the temperature. For the $\varepsilon_{\rm CF}=0$ case, $\Delta^{\sigma}\varepsilon_{\rm CF}(0)<0$ for $n=1,2,5$, while $\Delta^{\sigma}\varepsilon_{\rm CF}(0)>0$ for $n=4$. For $n=1$ and $n=5$, $\varepsilon_{\rm CF}$ correction at zero frequency is small. For $n=1$, $\varepsilon_{\rm CF}$ is always enhanced, except when it is small and positive. For $n=5$, $\varepsilon_{\rm CF}$ is changed slightly at large $|\varepsilon_{\rm CF}|$. Furthermore, for the $n=2$ case, $\varepsilon_{\rm CF}$ is enhanced for $\varepsilon_{\rm CF}<0$, while it is reduced for $\varepsilon_{\rm CF}>0$. In addition, for $n=4$, many-body effects reduce $\varepsilon_{\rm CF}$ for $\varepsilon_{\rm CF}<0$ and enhance it for $\varepsilon_{\rm CF}>0$. The enhancement of $\varepsilon_{\rm CF}$ is substantial. In particular, $\varepsilon_{\rm CF}$ is enhanced for very large $\varepsilon_{\rm CF}<0$ for the $n=2$ case and for very large $\varepsilon_{\rm CF}>0$ for the $n=4$

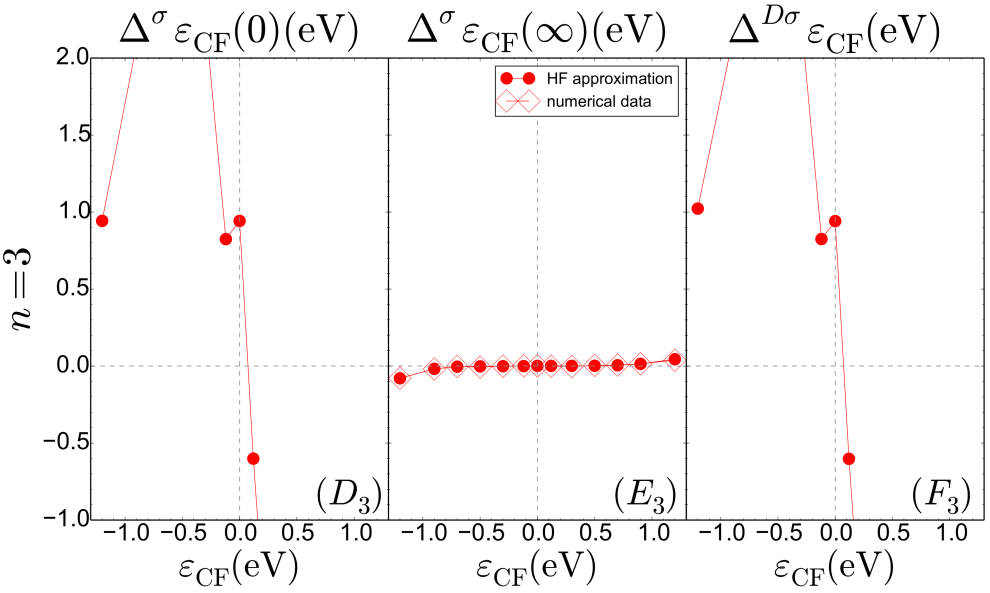


Figure 6.32: Evolution of the zero frequency crystal-field splitting correction per spin, $\Delta^{\sigma}\varepsilon_{\rm CF}(0)$, (the first column), the high frequency crystal-field splitting correction per spin, $\Delta^{\sigma}\varepsilon_{\rm CF}(\infty)$, (the second column) and $\Delta^{D\sigma}\varepsilon_{\rm CF}$ with increasing $\varepsilon_{\rm CF}$ from $\varepsilon_{\rm CF}=-1.20\,$eV to $\varepsilon_{\rm CF}=1.20\,$eV for the n=3 case at T=1160 K. The vertical gray dashed line corresponds to $\varepsilon_{\rm CF}$=0. The horizontal gray dashed line corresponds to $\Delta^{\sigma}\varepsilon_{\rm CF}(0)$=0 in panel $D3$, $\Delta^{\sigma}\varepsilon_{\rm CF}(\infty)$=0 in the panel E_3 and $\Delta^{D\sigma}\varepsilon_{\rm CF}$=0 in panel F_3.

case. In this situation, the xz/yz bands become half-filled and the xy band is inert, empty for the n=2 case and filled for n=4. At the same time $m^{*\sigma}_{xz/yz}$ diverge. In fact, the enhancement of $\varepsilon_{\rm CF}$ helps the metal insulator transition.

6.3 Effects of the SO interaction

The origin of the SO interaction can be understood by the following argument. The electric field of the nucleus is

$$\mathbf{E}_{nucl} = -\nabla v_{nucl}(\mathbf{r}) = -\frac{\mathbf{r}}{r}\frac{dv_{nucl}(r)}{dr}.$$

Seen by the electron, the nucleus is orbiting around it with velocity $\mathbf{v}$, creating a magnetic field $\mathbf{B}_{nucl}=-\alpha^2(\mathbf{v}\times\mathbf{E}_{nucl})$, where α is the fine structure constant. The magnetic moment of an electron $\boldsymbol{\mu}_e$ related to its spin angular momentum is $\boldsymbol{\mu}_e=-\frac{g_e}{2}\mathbf{S}$, where the electron spin g-factor is $g_e\approx 2$. The

energy of the magnetic moment of the electron is then

$$-\boldsymbol{\mu}_e \cdot \mathbf{B} = -\frac{\alpha^2}{r}\frac{dv(\mathbf{r})}{dr}\mathbf{S}\cdot\mathbf{L}. \tag{6.21}$$

For the hydrogen atom, the SO Hamiltonian, $\hat{H}_{\rm SO}$, is then

$$\hat{H}_{\rm SO} = \frac{\alpha^2}{r^3}\hat{\mathbf{S}}\cdot\hat{\mathbf{L}}. \tag{6.22}$$

In the presence of $\hat{H}_{\rm SO}$, $\hat{\mathbf{S}}$ and $\hat{\mathbf{L}}$ are no longer separately conserved quantities. However, rotational invariance guarantees the conservation of the total angular momentum $\hat{\mathbf{J}}$=$\hat{\mathbf{L}}+\hat{\mathbf{S}}$; it is thus often useful to rewrite $\hat{H}_{\rm SO}$ as

$$\hat{H}_{\rm SO} = \frac{\lambda}{2}\left(\hat{\mathbf{J}}^2 - \hat{\mathbf{L}}^2 - \hat{\mathbf{S}}^2\right), \tag{6.23}$$

where λ can be identified from Eq. (6.22).
In correlated materials, the SO interaction competes with the Coulomb parameters, the crystal-field, and the hopping integrals in determining the electronic properties. For the d shells, the SO Hamiltonian can be expressed as

$$\hat{H}_{SO} = \sum_{\mu}\lambda_\mu \sum_{mm'}\sum_{\sigma\sigma'}\epsilon^{\mu}_{m\sigma,m'\sigma'}c^{\dagger}_{m\sigma}c_{m'\sigma'}, \quad \epsilon^{\mu}_{m\sigma,m'\sigma'} = \langle m\sigma|\, l_\mu s_\mu \,|m'\sigma'\rangle\,, \tag{6.24}$$

where μ=x,y,z and λ_μ are the direction-dependent SO couplings.
Here, we consider systems in which the site symmetry is D_{4h}. Thus the SO parameters are also tetragonally anisotropic. By ordering the t_{2g}-states as $|xy\rangle_\uparrow$, $|yz\rangle_\uparrow$, $|xz\rangle_\uparrow$, $|xy\rangle_\downarrow$, $|yz\rangle_\downarrow$, $|xz\rangle_\downarrow$, in the presence of the SO interaction the on-site Hamiltonian is given by

$$\hat{\varepsilon} = \begin{pmatrix} \varepsilon_{xy} & 0 & 0 & 0 & \frac{\lambda_{xy}}{2} & \frac{-i\lambda_{xy}}{2} \\ 0 & \varepsilon_{yz} & \frac{i\lambda z}{2} & \frac{-\lambda_{xy}}{2} & 0 & 0 \\ 0 & \frac{-i\lambda_z}{2} & \varepsilon_{xz} & \frac{i\lambda_{xy}}{2} & 0 & 0 \\ 0 & \frac{-\lambda_{xy}}{2} & \frac{-i\lambda_{xy}}{2} & \varepsilon_{xy} & 0 & 0 \\ \frac{\lambda_{xy}}{2} & 0 & 0 & 0 & \varepsilon_{yz} & \frac{-i\lambda_z}{2} \\ \frac{i\lambda_{xy}}{2} & 0 & 0 & 0 & \frac{i\lambda_z}{2} & \varepsilon_{xz} \end{pmatrix}. \tag{6.25}$$

The coupling λ_{xy} is the SO matrix element between xy and xz/yz orbitals, in the different spin channels. Instead, λ_z couples the $|yz,\sigma\rangle$ orbital to the

$|xz,\sigma\rangle$ orbital, which are in the same spin channel. Here, we adopt the values of the SO parameters obtained for Sr_2RuO_4 in DFT calculations, λ_z=0.102 eV and λ_{xy}=0.100 eV; the tetragonal anisotropy is small, $\delta_\lambda=\lambda_z-\lambda_{xy}$=0.002 eV [83]. The on-site Hamiltonian, in the absence of a crystal-field is diagonal in the total angular momentum basis. In the presence of a crystal-field, states with different total angular momentum are coupled, however.
In this section, we study the electronic properties in the presence of the SO interaction. Firstly we present the results in the t_{2g} basis. Later we investigate the properties in the natural orbitals basis.

6.3.1 Results in the t_{2g} basis

Orbital-resolved spectral functions

Here, we investigate the effects of the SO interaction on the spectral functions. The results are shown in Fig. (6.33) at high temperature. We find that the SO interaction does not change the structure of the t_{2g} spectral functions. However in the low temperature regime, the effect of the SO interaction appears. This can be seen in Fig. (6.34). We start from panel A_2. Here, one can see that for the n=2 case, in the xy channel, the SO interaction makes the zero frequency quasi-particle peak more pronounced for large $\varepsilon_{\rm CF}$, while for the other values of $\varepsilon_{\rm CF}$, A^σ_{xy} is almost unchanged. Now let us look at the results in the xz/yz channels which are presented in panel $\mathsf{A'}_2$. For all values of considered $\varepsilon_{\rm CF}$, the SO interaction transfers spectral weight from the lower Hubbard band to positive frequency. The same effect can be seen in the behavior of the total spectral function, panel $\mathsf{A''}_2$. For the n=4 and n=5 cases, the results in all channels are almost unchanged.

Occupation number matrix and orbital polarization

Using Eq. (6.25) the occupation matrix in the presence of the SO interaction, is given by

$$\hat{n}=\begin{pmatrix} n^{\uparrow\uparrow}_{xy} & 0 & 0 & 0 & n^{\uparrow\downarrow}_{y} & -in^{\uparrow\downarrow}_{x} \\ 0 & n^{\uparrow\uparrow}_{yz} & in^{\uparrow\uparrow}_{z} & -n^{\uparrow\downarrow}_{y} & 0 & 0 \\ 0 & -in^{\uparrow\uparrow}_{z} & n^{\uparrow\uparrow}_{xz} & in^{\uparrow\downarrow}_{x} & 0 & 0 \\ 0 & -n^{\downarrow\uparrow}_{y} & -in^{\downarrow\uparrow}_{x} & n^{\downarrow\downarrow}_{xy} & 0 & 0 \\ n^{\downarrow\uparrow}_{y} & 0 & 0 & 0 & n^{\downarrow\downarrow}_{yz} & -in^{\downarrow\downarrow}_{z} \\ in^{\downarrow\uparrow}_{x} & 0 & 0 & 0 & in^{\downarrow\downarrow}_{z} & n^{\downarrow\downarrow}_{xz} \end{pmatrix}, \tag{6.26}$$

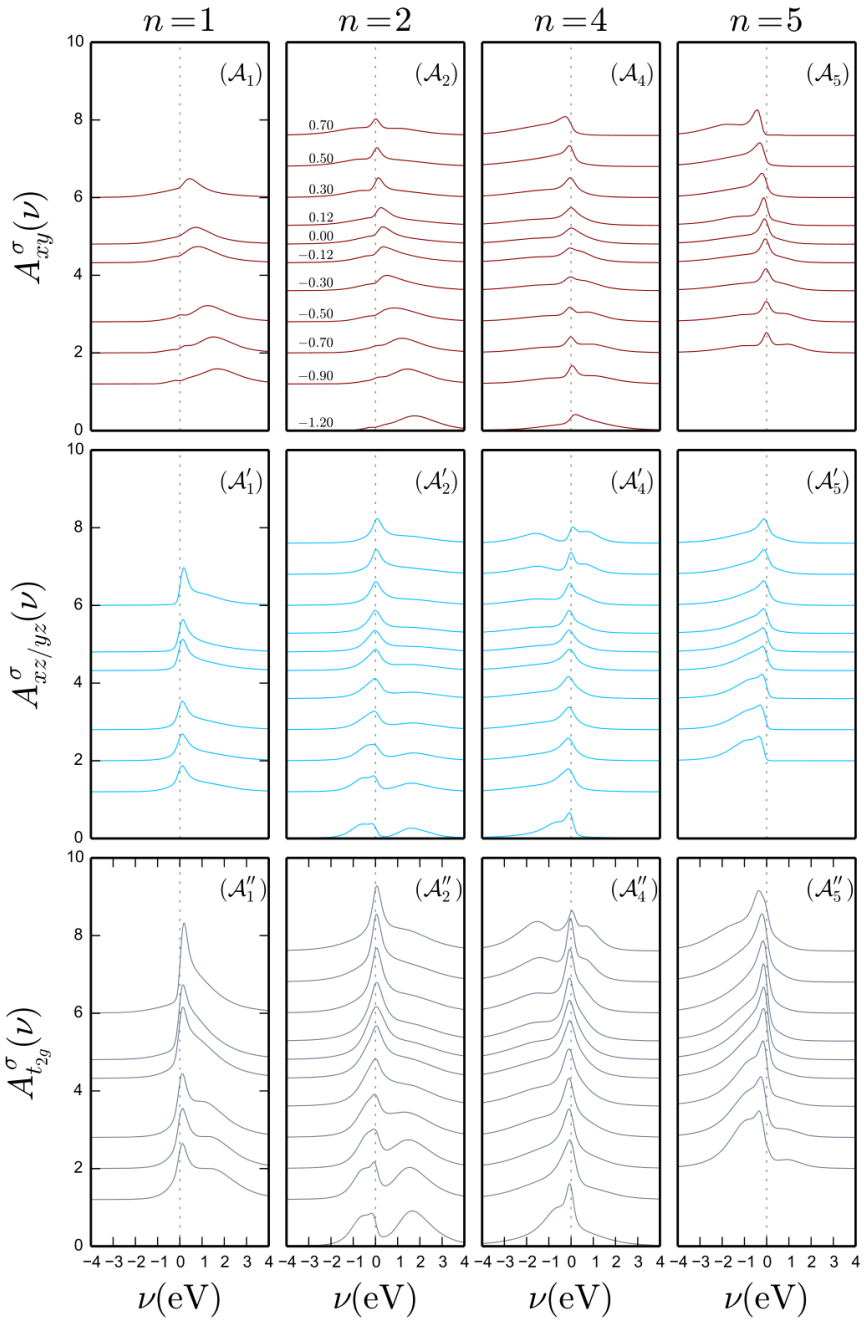


Figure 6.33: Evolution of the spectral functions in the presence of the SO interaction, at T=1160 K with increasing $\varepsilon_{\rm CF}$, for different integer filling numbers. Panels $\mathcal{A}_n$ show the spectral function of the xy channel, $\mathcal{A}'_n$ the spectral function of the xz/yz channels and $\mathcal{A}''_n$ the total spectral function of the system where n is the integer value of the filling number, n=1, 2, 4, 5. In all panels, curves are for different values of $\varepsilon_{\rm CF}$, defined as $\varepsilon_{\rm CF}$=$\varepsilon_{xz/yz}$−ε_{xy}. The chemical potential is set as the energy zero. The curves are shifted by an amount proportional to $\varepsilon_{\rm CF}$.

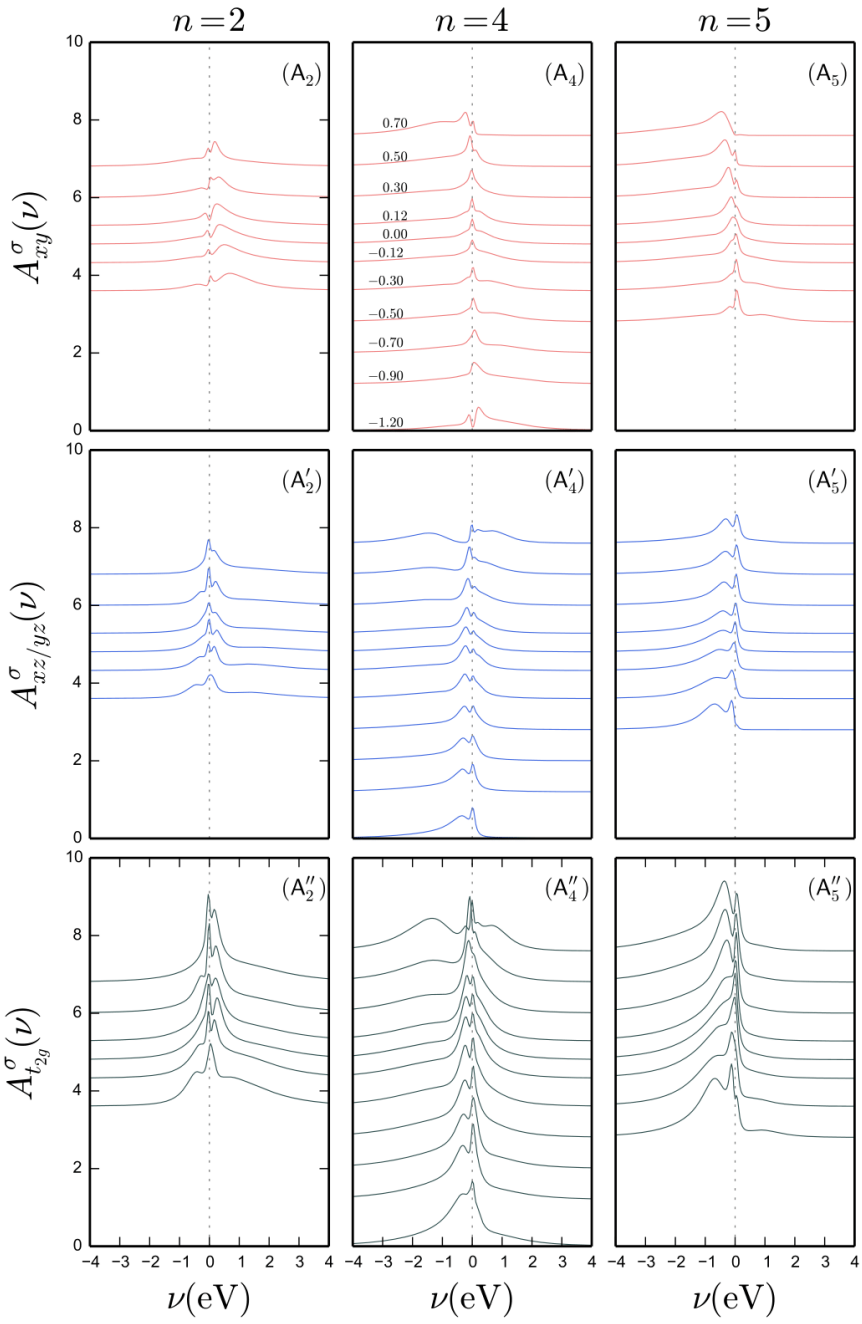


Figure 6.34: The behavior of the spectral functions in the presence of the SO interaction at T=290 K with increasing $\varepsilon_{\rm CF}$, for different integer filling numbers. Panels A_n show the spectral function of the xy channel, A'_n the spectral function of the xz/yz channels and A''_n the total spectral function of the system where n is the integer value of the filling number, n=2, 4, 5. In all panels, curves are for different values of $\varepsilon_{\rm CF}$, defined as $\varepsilon_{\rm CF}$=$\varepsilon_{xz/yz}$−ε_{xy}. The chemical potential is set as the energy zero. The curves are shifted by an amount proportional to $\varepsilon_{\rm CF}$.

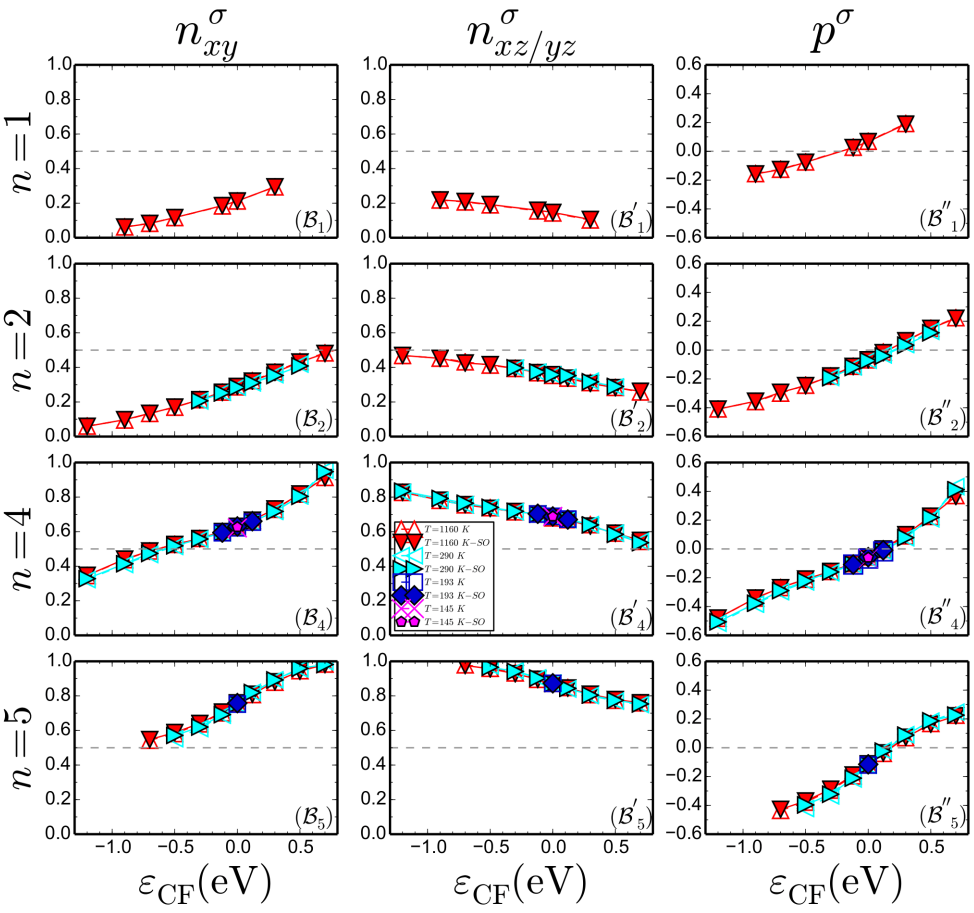


Figure 6.35: Evolution of n^{σ}_{xy} and $n^{\sigma}_{xz/yz}$, and p^{σ} with increasing $\varepsilon_{\rm CF}$. The filled markers show the results in the presence and the empty ones in the absence of the SO interaction. The results are shown at different temperatures, indicated in the legend of panel $\mathcal{B}'_4$, for the four integer filling numbers, n=1, 2, 4, 5. The behavior of n^{σ}_{xy}, $n^{\sigma}_{xz/yz}$ and p^{σ} is plotted in panels $\mathcal{B}_n$, $\mathcal{B}'_n$ and $\mathcal{B}''_n$, respectively.

where $n^{\sigma\sigma}_{m}$=$n^{\sigma'\sigma'}_{m}$ and $n^{\sigma\sigma}_{xz}$=$n^{\sigma\sigma}_{yz}$≠$n^{\sigma\sigma}_{xy}$; m=xy, xz, yz. In addition, $n^{\sigma\sigma}_{z}$=$n^{\sigma'\sigma'}_{z}$, $n^{\sigma\sigma'}_{y}$=$n^{\sigma'\sigma}_{y}$, $n^{\sigma\sigma'}_{x}$=$n^{\sigma'\sigma}_{x}$ and $n^{\sigma\sigma'}_{x}$=$n^{\sigma\sigma'}_{y}$. The elements of the occupation matrix are obtained from the Matsubara Green function, as previously discussed. To investigate the SO interaction effects on n^{σ}_{xy}, $n^{\sigma}_{xz/yz}$ and p^{σ}, we plot the results in the absence of the SO (no-SO) interaction (empty markers) and in the presence of the SO interaction (filled markers) in Fig. (6.35). All parameters are the same as in Fig. (6.9). We find that switching on the SO interaction does not change the results of n^{σ}_{xy}, $n^{\sigma}_{xz/yz}$ and p^{σ}. This conclusion is valid for all filling numbers and all values of considered $\varepsilon_{\rm CF}$ and temperatures.

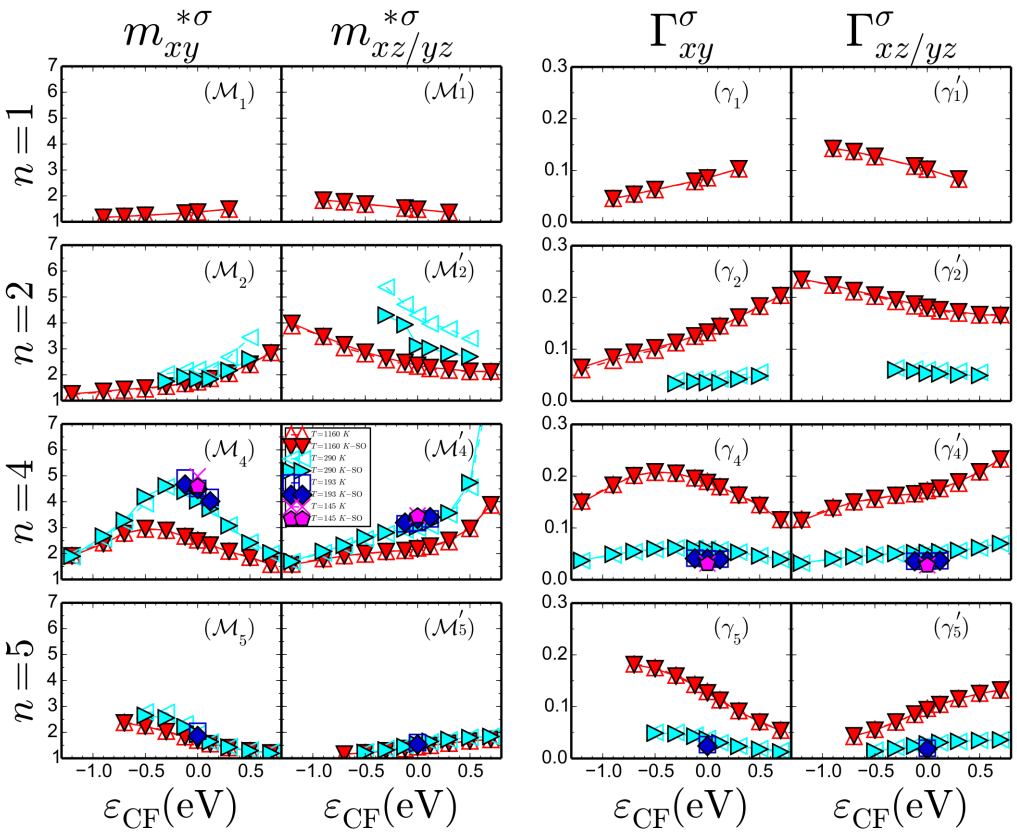


Figure 6.36: The behavior of $m^{*\sigma}_{xy}$, $m^{*\sigma}_{xz/yz}$, Γ^{σ}_{xy} and $\Gamma^{\sigma}_{xz/yz}$, with increasing $\varepsilon_{\rm CF}$ at different temperatures. The quantities are represented for the four integer filling numbers, n=1, 2, 4, 5. The first two columns show the behavior of $m^{*\sigma}_{xy}$ and $m^{*\sigma}_{xz/yz}$, and the second ones the behavior of Γ^{σ}_{xy} and $\Gamma^{\sigma}_{xz/yz}$, respectively. The filled markers show the results in the presence and the empty ones in the absence of the SO interaction. The behavior of $m^{*\sigma}_{xy}$ and $m^{*\sigma}_{xz/yz}$ are shown in panels $\mathcal{M}_n$ and $\mathcal{M}'_n$, while γ_n and γ'_n panels, represent the results for Γ^{σ}_{xy} and $\Gamma^{\sigma}_{xz/yz}$, respectively. The thermal energy for the highest temperature is $E_{T_h}\sim k_B T_h\sim 0.10\,$eV, which is in the same energy scale of the SO parameters, and for the lowest one is $E_{T_l}\sim k_B T_l\sim 0.01\,$eV. At room temperature $E_{T_r}\sim k_B T_r\sim 0.025\,$eV.

Effective-masses and scattering rates

In the presence of the SO interaction, the effective-mass enhancement and the corresponding quasi-particle scattering rate matrices have the same form of as the occupation matrix, Eq. (6.26). The diagonal elements of the effective-mass enhancement are the same as defined in Eqs. (6.7) to (6.9). The ele-

ments of the quasi-particle scattering rate can be obtained from

$$\left[\hat{\Gamma}\right]^{\sigma,\sigma'}_{m,m'} = -\left[[\hat{m}^*]^{-1}\left[\mathbf{Im}\,\hat{\Sigma}(i\nu_0)\right]\right]^{\sigma,\sigma'}_{m,m'}. \tag{6.27}$$

The off-diagonal elements of $\hat{m}$ and $\hat{\Gamma}$ matrices are small in comparison with the diagonal ones. In Fig. (6.36), the behavior of $m^{*\sigma}_{xy}$, $m^{*\sigma}_{xz/yz}$ and the corresponding quasi-particle scattering rates Γ^{σ}_{xy}, $\Gamma^{\sigma}_{xz/yz}$ are presented. The empty markers show the results for the no-SO case, while the filled ones are the same quantities in the presence of the SO interaction. Let us first look at the results of $m^{*\sigma}_{xy}$ and $m^{*\sigma}_{xz/yz}$, the first two columns in the figure. We find that for the $\mathbf{n}$=$\mathbf{1}, \mathbf{4}, \mathbf{5}$ cases, the SO interaction does not lead to any significant changes in $m^{*\sigma}_{xy}$ and $m^{*\sigma}_{xz/yz}$. However, one can see that for $\mathbf{n}$=$\mathbf{2}$, switching on the SO interaction at room temperature changes the behavior of $m^{*\sigma}_{xy}$ and $m^{*\sigma}_{xz/yz}$. As shown in panel $\mathcal{M}_2$, $m^{*\sigma}_{xy}$ is slightly smaller when the SO interaction is taken into account; the difference between $m^{*\sigma}_{xy}$ in these two set up of the calculations becomes larger when $\varepsilon_{\rm CF}$ increases. For what concerns $m^{*\sigma}_{xz/yz}$, panel $\mathcal{M}'_2$, we can see a drop of one unit for all considered values of $\varepsilon_{\rm CF}$. Now we consider the results of Γ^{σ}_{xy} and $\Gamma^{\sigma}_{xz/yz}$, the last two columns in the figure. We find that, the quasi-particle scattering rates in all channels, are very similar in no-SO and SO interaction calculations. This holds for the n=2 case too, in fact, in this situation the parameter dependence of $\frac{1}{m^*}$ and $\mathbf{Im}\,\Sigma(i\nu_0)$ compensate each other.

On-site parameters correction

Within LDA+DMFT the on-site Hamiltonian is modified by the self-energy. Therefore, in addition to $\varepsilon_{\rm CF}$, the SO couplings are also changed. The effective correction of the SO couplings at high frequency is given by the corresponding off-diagonal elements of the real part of the self-energy in high frequency limit, as follows:

$$\Delta\lambda_z(\infty) = -\big[\mathbf{Re}\Sigma_{yz\uparrow,xz\uparrow}(\infty) + \mathbf{Re}\Sigma_{yz\downarrow,xz\downarrow}(\infty)\big], \tag{6.28}$$

$$\Delta\lambda_{xy}(\infty) = \frac{1}{2}\sum_{\sigma}\sigma\big[\mathbf{Re}\Sigma_{xy\sigma,yz-\sigma}(\infty) - \mathbf{Re}\Sigma_{xy\sigma,xz-\sigma}(\infty)\big]. \tag{6.29}$$

As previously discussed, in the high frequency limit, the DMFT self-energy

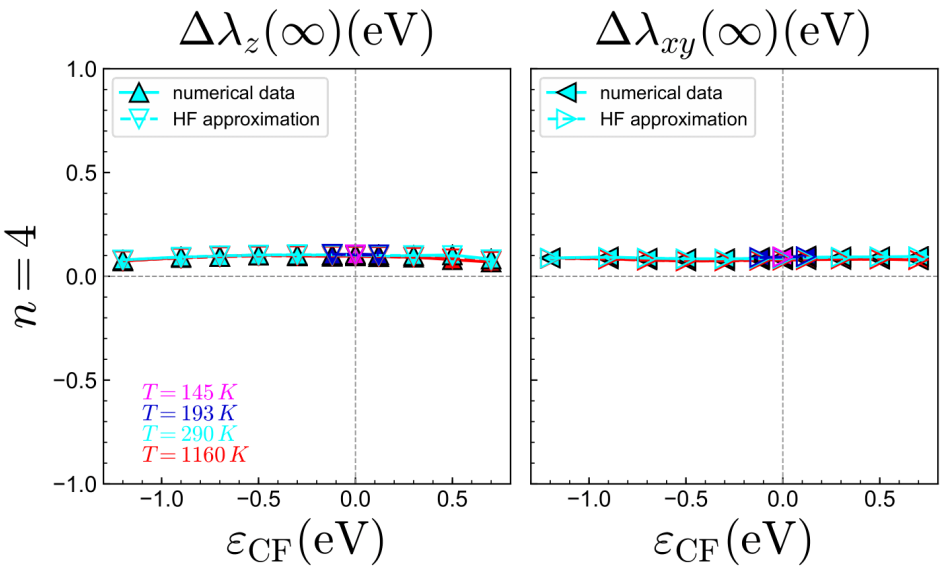


Figure 6.37: Evolution of the SO coupling correction, $\Delta\lambda_z(\infty)$ and $\Delta\lambda_{xy}(\infty)$ with increasing $\varepsilon_{\mathrm{CF}}$, at different temperatures for the n=4 case. The filled markers represent the results obtained via the numerical data, Eqs. (6.28) and (6.29), and the empty ones from the HF approximation, Eqs. (6.30) and (6.31).

equals the HF self-energy. Using the HF approximation, one can obtain

$$\frac{\Delta\lambda_z(\infty)}{2} = -\big[U-3J\big]n^{\sigma\sigma'}_{xz,yz}\delta_{\sigma,\sigma'}, \tag{6.30}$$

$$\frac{\Delta\lambda^{xz/yz}_{xy}(\infty)}{2} = -\big[U-3J\big]n^{\sigma\sigma'}_{xy,xz/yz}\delta_{\sigma,-\sigma'}. \tag{6.31}$$

Thus, we can check the accuracy of our numerical results by comparing the SO coupling correction from the HF approximation to ones from the numerical data. As an example, in Fig. (6.37), the SO couplings correction at high frequency is represented for the n=4 case. The left panel shows the behavior of $\Delta\lambda_z(\infty)$ and the right one of $\Delta\lambda_{xy}(\infty)$ with increasing $\varepsilon_{\mathrm{CF}}$. In each panel the filled markers present the SO couplings correction which is obtained from the numerical data, Eqs. (6.28) and (6.29), and the empty ones from the HF approximation, Eqs. (6.30) and (6.31). The figure shows that the results of $\Delta\lambda_z(\infty)$ and $\Delta\lambda_{xy}(\infty)$ from the numerical data are very close to the HF approximation formula.

Next, we investigate the effects of the SO interaction on the $\varepsilon_{\mathrm{CF}}$ correction. The results are presented in Fig. (6.38). In the figure, the empty markers present the values of $\varepsilon_{\mathrm{CF}}$ which are obtained from no-SO and the filled ones

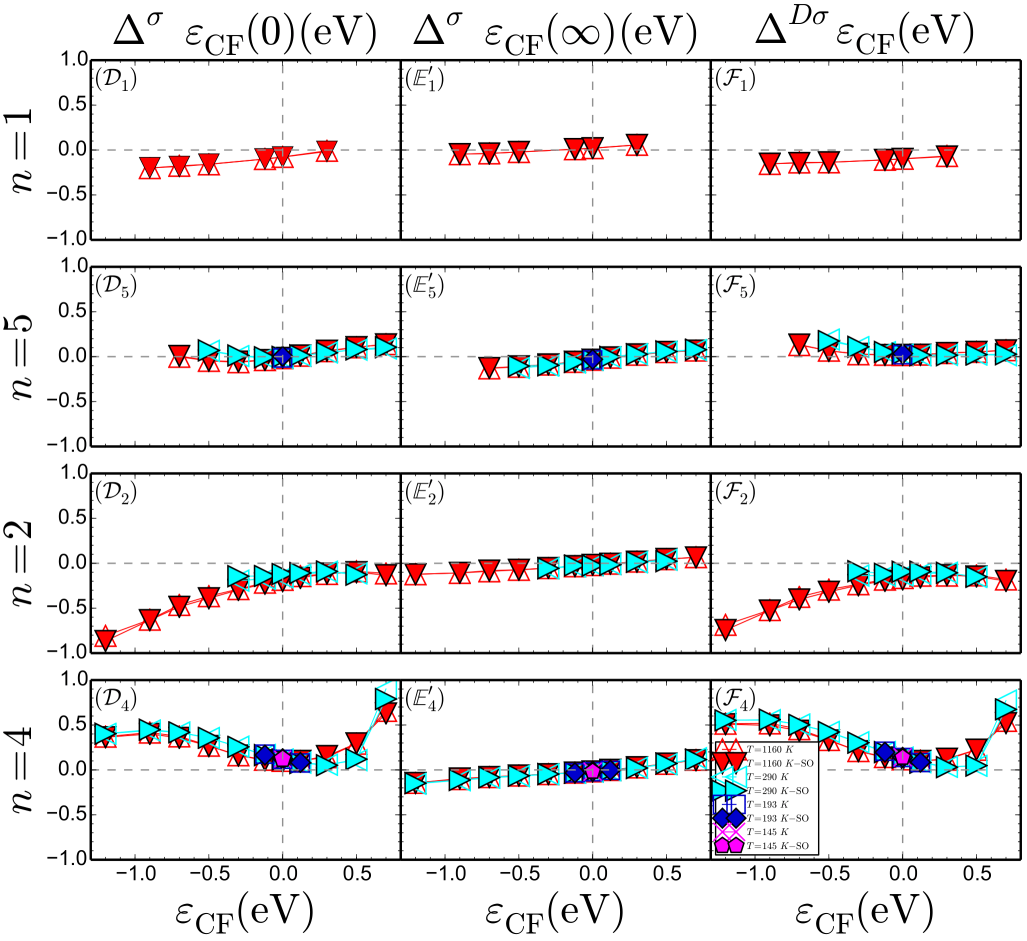


Figure 6.38: Evolution of the zero frequency $\varepsilon_{\rm CF}$ correction, $\Delta^{\sigma}\varepsilon_{\rm CF}(0)$ (the first column), the high frequency $\varepsilon_{\rm CF}$ correction $\Delta^{\sigma}\varepsilon_{\rm CF}(\infty)$ (the second column) and $\Delta^{D\sigma}\varepsilon_{\rm CF}$ (third column), with increasing $\varepsilon_{\rm CF}$. The filled markers shows the results in the presence of the SO interaction and the empty ones in the absence of the SO interaction. The first row presents the results for the n=1 case, the second one for n=5, the third one for n=2 and the fourth one for the n=4 case. In each panel, different curves represent the results for different temperatures which are shown in the legend of panel $\mathcal{F}_4$. The vertical gray dashed line corresponds to $\varepsilon_{\rm CF}$=0, while the horizontal gray dashed line in $\mathcal{D}_n$ panels corresponds to $\Delta^{\sigma}\varepsilon_{\rm CF}(0)$=0, in $\mathbb{E}_n$ panels indicates $\Delta^{\sigma}\varepsilon_{\rm CF}(\infty)$=0 and in $\mathcal{F}_n$ panels illustrates $\Delta^{D\sigma}\varepsilon_{\rm CF}$=0.

from the SO calculations. The parameters in the figure, are the same as defined in subsection (6.2.5). We find that by switching on the SO interaction, the behavior of $\Delta^{\sigma}\varepsilon_{\rm CF}(0)$, $\Delta^{\sigma}\varepsilon_{\rm CF}(\infty)$ and $\Delta^{D\sigma}\varepsilon_{\rm CF}(\infty)$ remains almost unchanged. This conclusion is true for all filling numbers.

6.3.2 Results in the natural orbitals basis

In the t_{2g} basis, the Green function, and therefore, the occupation matrix is not diagonal. We can however diagonalize it via a unitary transformation U

$$U^{-1}\hat{n}U = \hat{n}^{\rm d}. \tag{6.32}$$

The U matrix is given by the eigenvectors of the $\hat{n}$ matrix, the *natural orbitals*. We label the eigenvectors as $\{|a\rangle, |a'\rangle, |b\rangle, |b'\rangle, |c\rangle, |c'\rangle\}$ and the corresponding eigenvalues as $\{n_a, n_{a'}, n_b, n_{b'}, n_c, n_{c'}\}$. We order the states such that $n_a{=}n_{a'} < n_b{=}n_{b'} < n_c{=}n_{c'}$. The levels are doubly degenerate because of *Kramers degeneracy*. In the atomic limit, the natural orbitals are the eigenvectors of the on-site Hamiltonian, Eq. (6.25). In the presence of crystal-field and SO interaction, one can obtain them from those for $n{=}5$ represented in Ref. [84], using particle-hole symmetry. In the presence of hopping integrals the natural orbitals can differ from the eigenstates of the t_{2g}^1 configuration. It is however useful to discuss the atomic limit to qualitatively understand the results. In this case, the eigenvectors of the on-site Hamiltonian are expressed as

$$|1,\sigma\rangle = \chi_6 |xy,\sigma\rangle - \frac{\chi_5}{\sqrt{2}}\left[|xz,\sigma\rangle - 2i\sigma\,|yz,-\sigma\rangle\right], \tag{6.33}$$

$$|2,\sigma\rangle = \frac{1}{\sqrt{2}}\left[|xz,\sigma\rangle + 2i\sigma\,|yz,\sigma\rangle\right], \tag{6.34}$$

$$|3,\sigma\rangle = \chi_5 |xy,\sigma\rangle + \frac{\chi_6}{\sqrt{2}}\left[|xz,\sigma\rangle - 2i\sigma\,|yz,-\sigma\rangle\right], \tag{6.35}$$

where the coefficients χ_5 and χ_6 are positive and given by

$$\chi_5^2 = \frac{2\lambda_{xy}^2}{\left(-\varepsilon_{\rm CF} - \frac{\lambda_z}{2} + \sqrt{\left(\varepsilon_{\rm CF} + \frac{\lambda_z}{2}\right)^2 + 2\lambda_{xy}^2}\right)^2 + 2\lambda_{xy}^2}, \tag{6.36}$$

$$\chi_6^2 = 1 - \chi_5^2. \tag{6.37}$$

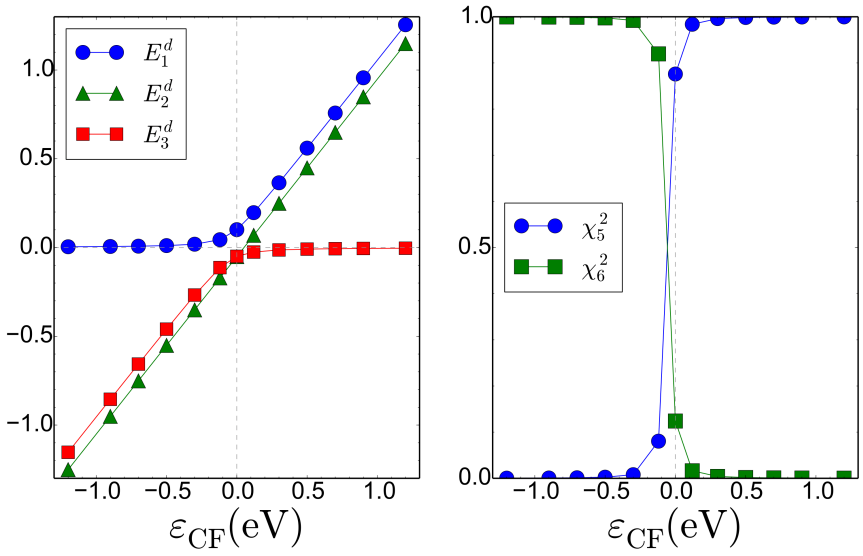


Figure 6.39: (Left) Evolution of the eigenenergies of the on-site Hamiltonian in the presence of the crystal-field and SO interaction. The expressions of the energies are given in Eqs. (6.38) to (6.40). The on-site Hamiltonian is presented in Eq. (6.25). (Right) The behavior of χ_5^2 and χ_6^2 versus $\varepsilon_{\rm CF}$. These coefficients are defined in Eqs. (6.36) and (6.37).

The states $|m,\sigma\rangle$ are defined as $|m,\sigma\rangle = c^\dagger_{m\sigma}|0\rangle$. The corresponding energies are given by

$$E_1^d = \frac{-1}{2}\left[-\varepsilon_{\rm CF} - \frac{\lambda_z}{2} - \sqrt{\left(\varepsilon_{\rm CF}+\frac{\lambda_z}{2}\right)^2 + 2\lambda_{xy}^2}\right], \tag{6.38}$$

$$E_2^d = \varepsilon_{\rm CF} - \frac{\lambda_z}{2}, \tag{6.39}$$

$$E_3^d = \frac{-1}{2}\left[-\varepsilon_{\rm CF} - \frac{\lambda_z}{2} + \sqrt{\left(\varepsilon_{\rm CF}+\frac{\lambda_z}{2}\right)^2 + 2\lambda_{xy}^2}\right]. \tag{6.40}$$

The behavior of the eigenenergies are plotted in the left panel of Fig. (6.39), which shows that the ground state depends on the value of $\varepsilon_{\rm CF}$. For $\varepsilon_{\rm CF} < 0$, the energy of the states in descending order is: $E_2^d < E_3^d < E_1^d$; E_2^d and E_3^d are slightly different, while E_3^d is much larger. For $\varepsilon_{\rm CF} > 0$: $E_3^d < E_2^d < E_1^d$; the values of E_2^d and E_1^d are close, while E_3^d is much smaller. Furthermore in the right panel of Fig. (6.39), the evolution of χ_5^2 and χ_6^2 versus $\varepsilon_{\rm CF}$ is plotted. The panel shows that for large negative $\varepsilon_{\rm CF}$, $|1,\sigma\rangle \sim |xy,\sigma\rangle$ and

for large positive $\varepsilon_{\rm CF}$, $|3,\sigma\rangle \sim |xy,\sigma\rangle$. Therefore, for large $\varepsilon_{\rm CF} < 0$, the xy orbital is the least occupied, while for large $\varepsilon_{\rm CF} > 0$, the xy orbital is the most occupied state.

Orbital-resolved spectral function

In order to obtain the spectral functions in the natural orbitals basis, we transform the Matsubara Green function as

$$U^{-1}\hat{G}(\tau)U = \hat{G}^{\rm d}(\tau). \tag{6.41}$$

Then the spectral functions, $A^{\rm d}_a(\nu)$, $A^{\rm d}_b(\nu)$ and $A^{\rm d}_c(\nu)$ can be obtained from the corresponding components of $\hat{G}^{\rm d}(\tau)$. One should notice that since the trace is invariant under the transformation, the total spectral function is the same in both bases. In Fig. (6.40), the behavior of the spectral functions in the natural orbitals basis at T=1160 K are shown. The first row of the figure shows the results of $A^{\rm d}_a(\nu)$, the second one of $A^{\rm d}_b(\nu)$, the third one of $A^{\rm d}_c(\nu)$ and the last one of the total spectral function, $A^{\rm d}_{tot}(\nu)$. For all presented filling numbers, $A^{\rm d}_b(\nu)$ and $A^{\sigma}_{xz/yz}(\nu)$ have the same structure at any $\varepsilon_{\rm CF}$. The reason is that the $|b\rangle$ is a linear combination of $|xz,\sigma\rangle$ and $|yz,\sigma\rangle$ and therefore the spectral function of this component has the character of $A^{\sigma}_{xz/yz}(\nu)$. In addition, we find that for $\mathbf{n}$=$\mathbf{1},\mathbf{2},\mathbf{4}$, $A^{\rm d}_a(\nu)$ and $A^{\sigma}_{xy}(\nu)$ show similar behavior for negative $\varepsilon_{\rm CF}$.
We start from the top left panel. The figure shows that for $\mathbf{n}$=$\mathbf{1}$, for positive $\varepsilon_{\rm CF}$, $A^{\rm d}_a(\nu)$ has a pronounced peak at positive frequency and the orbital occupancy of the a band is tiny. Next we consider the results of $A^{\rm d}_c(\nu)$, shown in panel $\mathbb{A}''_1$. For $\varepsilon_{\rm CF}\leq$0, the spectral function exhibits a broad quasi-particle peak at zero frequency. Increasing $\varepsilon_{\rm CF}$, $A^{\rm d}_c(\nu)$ develops a small peak at positive frequency. The quasi-particle peak spread out and sizable spectral weight is transferred to positive frequency.
Then, we consider the results of $\mathbf{n}$=$\mathbf{2}$. Panel $\mathbb{A}_2$ shows that for $\varepsilon_{\rm CF}$=0, $A^{\rm d}_a(\nu)$ exhibits a quite broad quasi-particle peak at zero frequency which becomes slightly narrower, when $\varepsilon_{\rm CF}$ increases. Now we look at the results of $A^{\rm d}_c(\nu)$, shown in panel $\mathbb{A}''_2$. For very large negative $\varepsilon_{\rm CF}$, $A^{\rm d}_c(\nu)$ shows two peaks at positive and negative frequencies. Increasing $\varepsilon_{\rm CF}$, spectral weight is transferred from negative to zero frequency, until at $\varepsilon_{\rm CF}$=0, $A^{\rm d}_c(\nu)$ develops a broad zero frequency quasi-particle peak. Further increasing $\varepsilon_{\rm CF}$, the peak becomes more pronounced. Finally, for large positive $\varepsilon_{\rm CF}$, $A^{\rm d}_c(\nu)$ exhibits the characteristic three peaks structure.

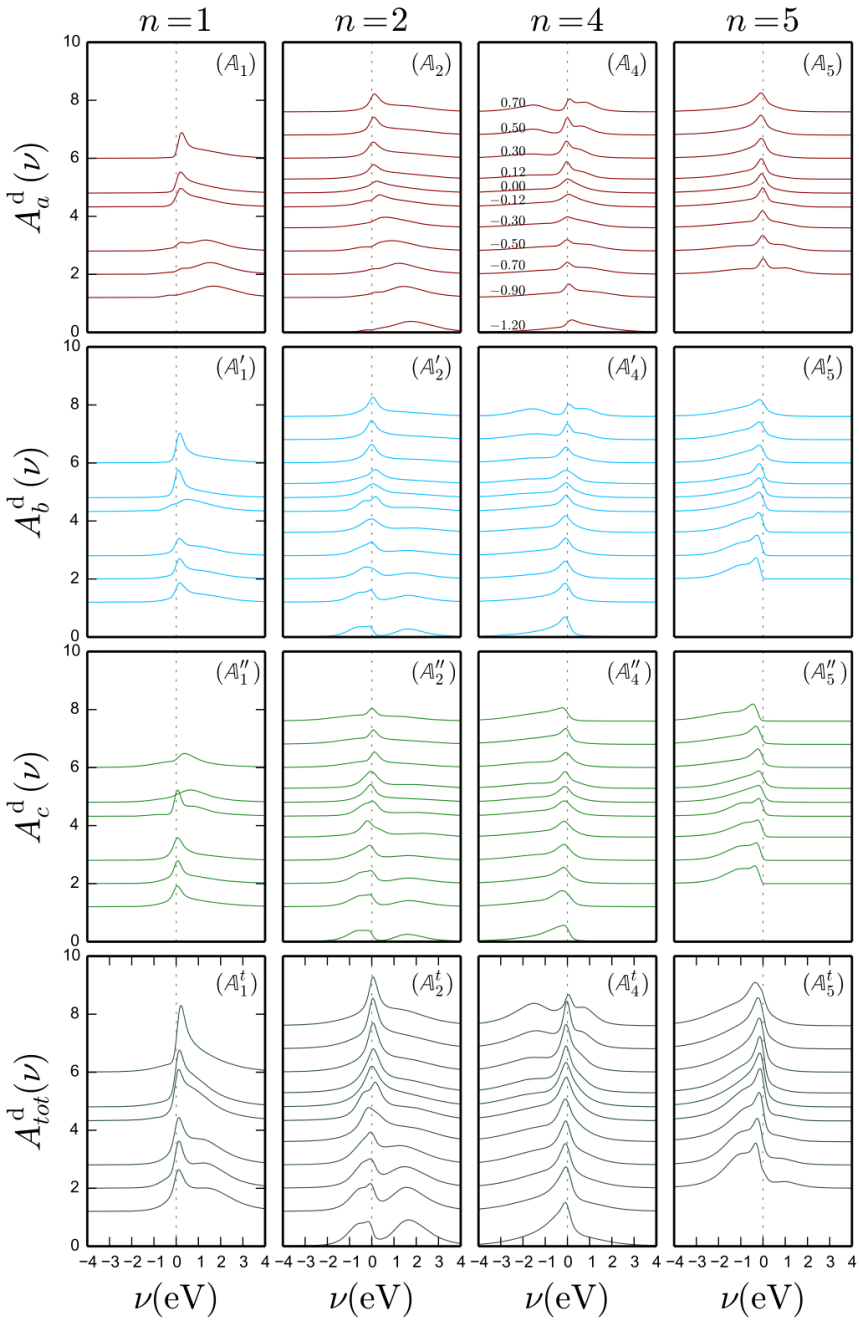


Figure 6.40: Evolution of the spectral functions in the presence of the SO interaction, at T=1160 K with increasing $\varepsilon_{\rm CF}$. The spectral functions are obtained in the natural orbitals basis. Panels $\mathbb{A}_n$, $\mathbb{A}'_n$ and $\mathbb{A}''_n$ show the spectral functions in the a, b and c channels, respectively. In addition, panels $\mathbb{A}^t_n$ present the total spectral functions, where n=1, 2, 4, 5. In all panels, curves are for different values of $\varepsilon_{\rm CF}$, defined as $\varepsilon_{\rm CF}$=$\varepsilon_{xz/yz}-\varepsilon_{xy}$. The chemical potential is set as the energy zero in all panels. The curves are shifted by an amount proportional to $\varepsilon_{\rm CF}$.

Next, let us investigate the **n=4** case. Panel $\mathbb{A}_4$ shows that for positive $\varepsilon_{\mathrm{CF}}$, spectral weight is transferred from zero frequency to the lower and upper Hubbard bands, when $\varepsilon_{\mathrm{CF}}$ increases. In this situation, the zero frequency quasi-particle peak becomes narrower and the system goes deeply into the strongly-correlated regime.
Finally, we look at the results of **n=5**. We find that $A^{\sigma}_{xy}(\nu)$ and $A^{d}_{a}(\nu)$ have the same structure, except for large positive $\varepsilon_{\mathrm{CF}}$. Panel $\mathbb{A}_5$ illustrates that the band is still occupied and has a broad zero frequency quasi-particle peak, for large positive $\varepsilon_{\mathrm{CF}}$. Instead, panel $\mathbb{A}''_5$ shows that the c band is fully occupied, except for small $|\varepsilon_{\mathrm{CF}}|$.

Occupation numbers and natural orbital polarization

Here, we investigate the occupation numbers in the natural orbitals basis. We define the natural orbital polarization as

$$p^{\mathrm{d}} = n^{\mathrm{d}}_{c} - \frac{1}{2}\left(n^{\mathrm{d}}_{a} + n^{\mathrm{d}}_{b}\right). \tag{6.42}$$

The natural occupation numbers fulfill the two conditions

$$0 \leq n^{\mathrm{d}}_{\mathsf{m}} \leq 1, \quad \sum_{\mathsf{m}} n^{\mathrm{d}}_{\mathsf{m}} = \frac{n_{tot}}{2}; \quad \mathsf{m} = a, b, c, \tag{6.43}$$

where n_{tot} is the total number of the electrons. The results are presented in Fig. (6.41). The first column shows the behavior of n^{d}_{a}, the second one n^{d}_{b}, the third one n^{d}_{c}, and the last one p^{d}. Instead, different rows correspond to different filling numbers. The gray dashed line in the panels shows $n^{\mathrm{d}}_{\mathsf{m}} = 0.5$. First of all, the figure illustrates that lowering the temperature does not change the results significantly. Therefore, we look at the behavior of the quantities with increasing $\varepsilon_{\mathrm{CF}}$.
For the **n=1** case, we find that the occupation number in the a and b orbitals are almost unvarying when $\varepsilon_{\mathrm{CF}}$ increases. Instead, n^{d}_{c} has a minimum around small negative $\varepsilon_{\mathrm{CF}}$. In addition, all three orbitals are less than half-filled; the occupation number in the a orbital is very small.
One can see for **n=2, 4, 5**, that for $\varepsilon_{\mathrm{CF}} \leq 0$, n^{σ}_{xy} and n^{d}_{a} behave similarly, while for $\varepsilon_{\mathrm{CF}} > 0$, n^{d}_{a} decreases slightly when $\varepsilon_{\mathrm{CF}}$ increases. In addition, the behavior of n^{d}_{b} and $n^{\sigma}_{xz/yz}$ is almost the same. Now we look at the results of n^{d}_{c} for each filling number. The figure shows that for **n=2**, the c orbital is half-filled, except for small $|\varepsilon_{\mathrm{CF}}|$ where n^{d}_{c} becomes $n^{\mathrm{d}}_{c} < 0.5$. For **n=4**, for all

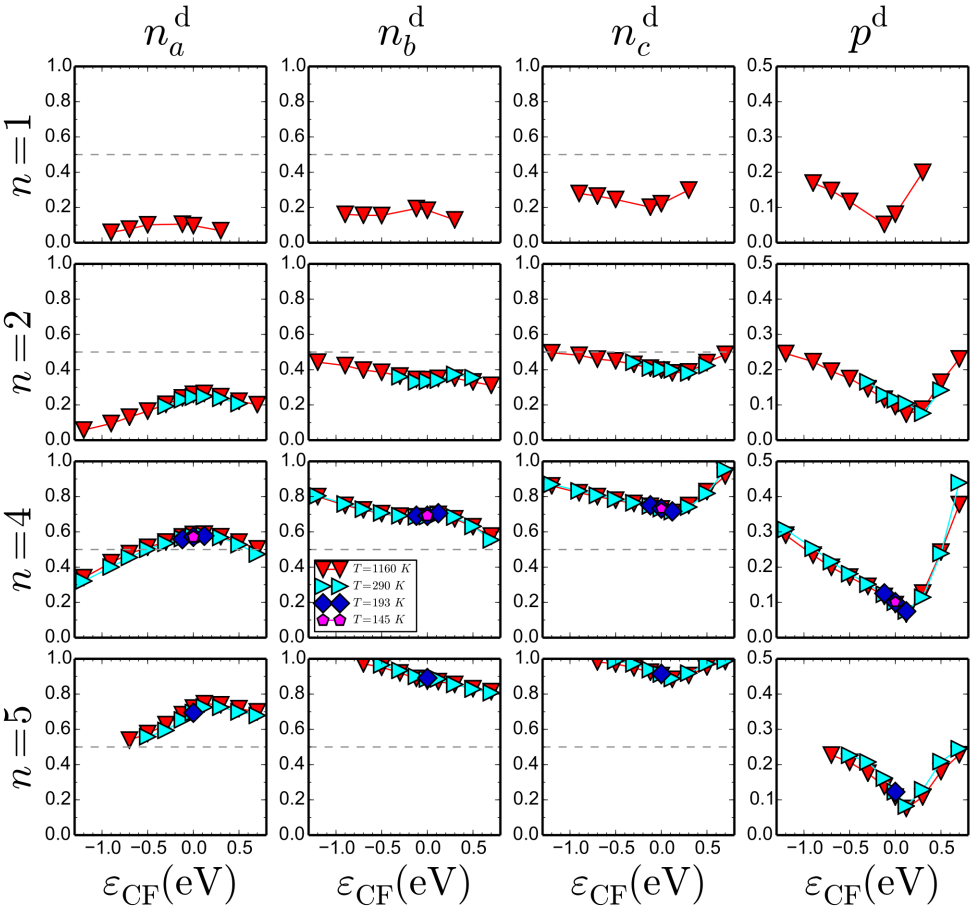


Figure 6.41: Evolution of the eigenvalues of the occupation matrix in the presence of the SO interaction and the corresponding orbital polarization with increasing $\varepsilon_{\mathrm{CF}}$. The results are shown at different temperatures, for the four integer filling numbers, n=1, 2, 4, 5. Here, the natural orbital polarization is defined as p^{d}=$n_c^{\mathrm{d}} - \frac{1}{2}\left(n_a^{\mathrm{d}} + n_b^{\mathrm{d}}\right)$, where the c orbital is the most occupied and the a orbital is the least occupied one.

considered $\varepsilon_{\mathrm{CF}}$, n_c^{d}>0.5 and it has a minimum around very small $|\varepsilon_{\mathrm{CF}}|$. In addition, for **n=5**, the c orbital is almost filled, except for very small $|\varepsilon_{\mathrm{CF}}|$. We find that the natural orbital polarization is positive and has a minimum for all filling numbers. The minimum value occurs around $\varepsilon_{\mathrm{CF}}\approx$0.12 eV for **n=2, 4, 5**, while for **n=1** it happens for $\varepsilon_{\mathrm{CF}}\approx -0.12$ eV.
One can see that for large $\varepsilon_{\mathrm{CF}}$<0, the occupation numbers of the b and c orbitals are close and larger than the one of the a orbital. Instead, for large $\varepsilon_{\mathrm{CF}}$>0, the occupation numbers of the a and b orbitals are slightly different

and smaller than the one of the c orbital. In addition, the occupation number of the b orbital decreases linearly with increasing $\varepsilon_{\rm CF}$. These trends are in line with the behavior of the eigenenergies in the atomic limit, which was shown in the left panel of Fig. (6.39).

Effective-masses and scattering rates

The effective-mass enhancement and quasi-particle scattering rate matrices in the basis of the natural orbitals are given by

$$\hat{m}^{*\rm d} = U^{-1}\hat{m}^{*}U, \tag{6.44}$$
$$\hat{\Gamma}^{\rm d} = U^{-1}\hat{\Gamma}U, \tag{6.45}$$

where the off-diagonal elements of the matrices are now very small in comparison with the diagonal ones. The behavior of the diagonal elements of $\hat{m}^{*\rm d}$ and $\hat{\Gamma}^{\rm d}$ are presented in Fig. (6.42). The first three panels show the results of $m_a^{*\rm d}$, $m_b^{*\rm d}$ and $m_c^{*\rm d}$, and the second three ones, present the behavior of the corresponding quasi-particle scattering rates, $\Gamma_a^{\rm d}$, $\Gamma_b^{\rm d}$ and $\Gamma_c^{\rm d}$, respectively. Different rows present the results for different filling numbers, sequentially. The figure shows that for all three orbitals, the corresponding quasi-particle scattering rates decrease with lowering the temperature. In addition, $\Gamma_a^{\rm d}$, $\Gamma_b^{\rm d}$ and $\Gamma_c^{\rm d}$ are almost unchanged when $\varepsilon_{\rm CF}$ increases, except at very high temperature. Thus, in the following we look at the behavior of the quasi-particle scattering rates at very high temperature. The comparison between Figs. (6.36) and (6.42) illustrates that the results of $m_a^{*\rm d}$ and $\Gamma_a^{\rm d}$ are similar to $m_{xy}^{*\sigma}$ and Γ_{xy}^{σ} for $\varepsilon_{\rm CF}\leq 0$, correspondingly. In addition, $m_b^{*\rm d}$ and $\Gamma_b^{\rm d}$ behave almost as $m_{xz/yz}^{*\sigma}$ and $\Gamma_{xz/yz}^{\sigma}$, for all cases. Thus, we focus only on the a orbital for positive $\varepsilon_{\rm CF}$ and the c channel.
First, let us discuss the a orbital. For $\mathbf{n}=\mathbf{1}$, it is almost empty, so $m_a^{*\rm d}$ and $\Gamma_a^{\rm d}$ have no physical meaning. For the $\mathbf{n}=\mathbf{2},\mathbf{5}$ cases, $m_a^{*\rm d}$ and $\Gamma_a^{\rm d}$ are almost unchanged when $\varepsilon_{\rm CF}$ increases. Furthermore, the results of $m_a^{*\rm d}$ are nearly temperature-independent. For $\mathbf{n}=\mathbf{4}$, we find that $m_a^{*\rm d}$ has a minimum for very small positive $\varepsilon_{\rm CF}$. In addition, $m_a^{*\rm d}$ grows on lowering the temperature. The figure shows that $\Gamma_a^{\rm d}$ increases when $\varepsilon_{\rm CF}$ increases.
Next, we consider the c channel. For $\mathbf{n}=\mathbf{1},\mathbf{2}$, $m_c^{*\rm d}$ and $\Gamma_c^{\rm d}$ has a minimum around small $|\varepsilon_{\rm CF}|$. The value of $m_c^{*\rm d}$ is larger for n=2 in comparison with one for n=1 for any $\varepsilon_{\rm CF}$. Furthermore, $m_c^{*\rm d}$ is almost temperature-independent for $\varepsilon_{\rm CF}\geq 0$, while for the other values of $\varepsilon_{\rm CF}$, $m_c^{*\rm d}$ increases with lowering

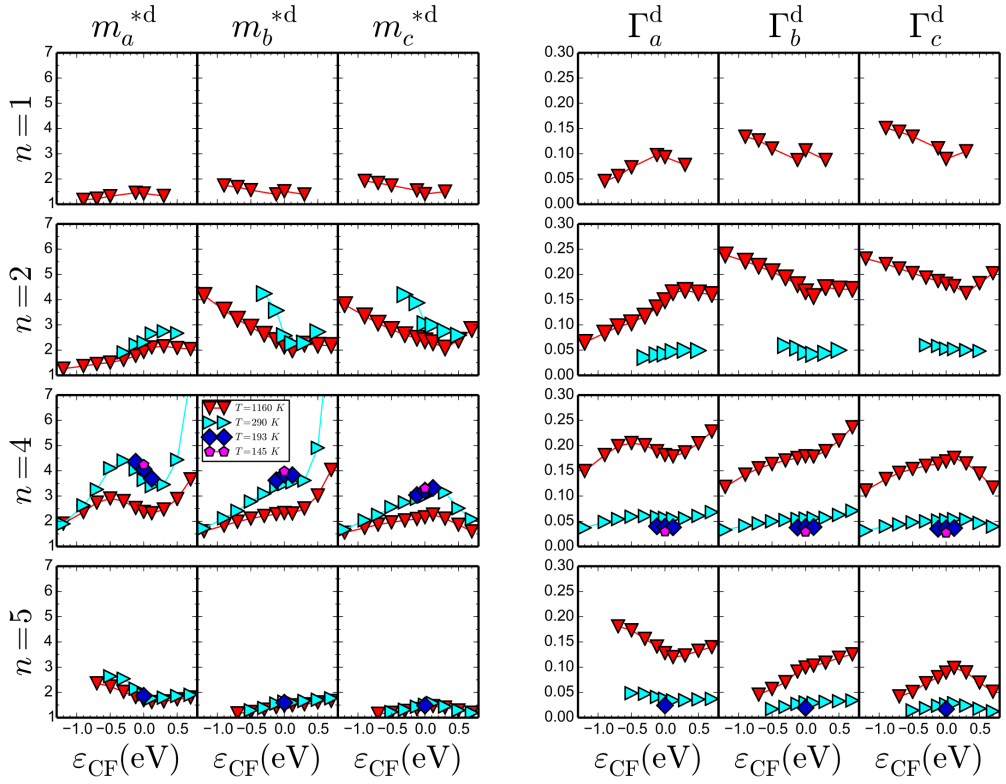


Figure 6.42: Evolution of the diagonal elements of the effective-mass enhancement (the first three columns) and the quasi-particle scattering rate (the second three columns) matrices in the presence of the SO interaction in the natural orbitals basis, with increasing $\varepsilon_{\mathrm{CF}}$. The quantities are represented for the four integer filling numbers, n=1, 2, 4, 5. The first row show the results for n=1, the second one for n=2, the third one for n=4 and the fourth one for n=5. In each panel different colors represent different temperatures.

the temperature. Then, we investigate the **n=4** case. The figure shows that $m_c^{*\mathrm{d}}$ and Γ_c^{d} have a maximum around very small positive $\varepsilon_{\mathrm{CF}}$. Around the maximum, lowering the temperature, $m_c^{*\mathrm{d}}$ becomes slightly larger. Finally, for **n=5**, the c orbital is almost filled except for small $|\varepsilon_{\mathrm{CF}}|$; for small $|\varepsilon_{\mathrm{CF}}|$, the value of $m_c^{*\mathrm{d}}$ is tiny.

Natural orbitals energy correction

The many-body effects at low energy change the energy levels of the natural orbitals. In order to investigate these effects, we need to transform the real

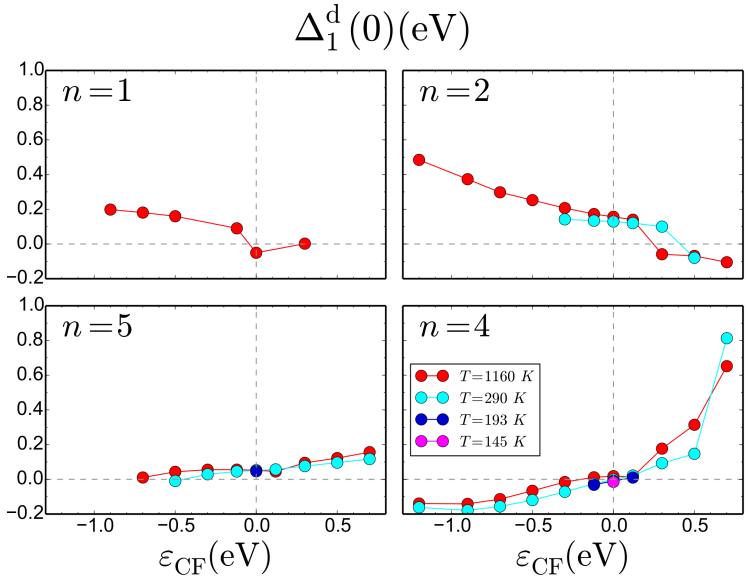


Figure 6.43: Evolution of $\Delta_1^{\rm d}(0)$, which is defined in Eq. (6.47), with increasing $\varepsilon_{\rm CF}$. The results are presented for the four integer filling numbers, n=1, 2, 4, 5. In each panel, different curves represent the results for different temperatures. The vertical gray dashed line corresponds to $\varepsilon_{\rm CF}$=0 and the horizontal one shows $\Delta_1^{\rm d}(0)$=0, in each panel.

part of the self-energy at zero frequency to the natural orbitals basis

$$U^{-1}\left[\mathbf{Re}\,\hat{\Sigma}(i\nu_0)\right]U=\left[\mathbf{Re}\,\hat{\Sigma}(i\nu_0)\right]^{\rm d}. \tag{6.46}$$

The off-diagonal elements of $\left[\mathbf{Re}\,\hat{\Sigma}(i\nu_0)\right]^{\rm d}$ are small and can be neglected. We define the quantities

$$\Delta_1^{\rm d}(0)=\left(\frac{\mathbf{Re}\,\Sigma_a^{\rm d}(i\nu_0)+\mathbf{Re}\,\Sigma_b^{\rm d}(i\nu_0)}{2}\right)-\mathbf{Re}\,\Sigma_c^{\rm d}(i\nu_0), \tag{6.47}$$

and

$$\Delta_2^{\rm d}(0)=\mathbf{Re}\,\Sigma_b^{\rm d}(i\nu_0)-\mathbf{Re}\,\Sigma_a^{\rm d}(i\nu_0). \tag{6.48}$$

Firstly, let us investigate $\Delta_1^{\rm d}(0)$, which is presented in Fig. (6.43). We start from the top left panel. The figure shows that for **n=1**, $\Delta_1^{\rm d}(0)\approx 0$ for $\varepsilon_{\rm CF}>0$ and becomes $\Delta_1^{\rm d}(0)>0$ for the other values of $\varepsilon_{\rm CF}$.
We find that for **n=2**, $\Delta_1^{\rm d}(0)$ shows descending behavior, while for **n=4** it increases with increasing $\varepsilon_{\rm CF}$.

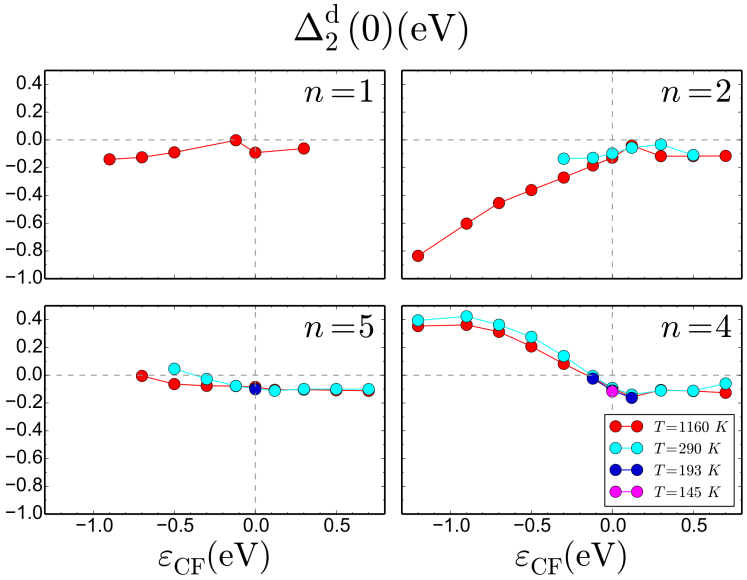


Figure 6.44: The behavior of $\Delta_2^{\rm d}(0)$, which is defined in Eq. (6.48), with increasing $\varepsilon_{\rm CF}$. The results are presented for the four integer filling numbers, n=1, 2, 4, 5. In each panel, different curves represent the results for different temperatures. The vertical gray dashed line corresponds to $\varepsilon_{\rm CF}$=0 and the horizontal one shows $\Delta_2^{\rm d}(0)$=0, in each panel.

The figure shows that for **n=5** case, $\Delta_1^{\rm d}(0)\approx 0$ for $\varepsilon_{\rm CF}\leq 0$ and increases slightly for positive $\varepsilon_{\rm CF}$.We can conclude that the value of $\Delta_1^{\rm d}(0)$ for **n=2**, for very large negative $\varepsilon_{\rm CF}$ as well as for **n=4**, for large positive $\varepsilon_{\rm CF}$, is considerable. However for **n=1** and **n=5**, it is not very large.
Now we consider the results of $\Delta_2^{\rm d}(0)$, shown in Fig. (6.44). The figure shows that for **n=1** and **n=5**, $\Delta_2^{\rm d}(0)\leq 0$ for any value of $\varepsilon_{\rm CF}$. For **n=1**, $\Delta_2^{\rm d}(0)$ increases, while for **n=5** it decreases slightly and becomes almost unchanged for positive $\varepsilon_{\rm CF}$. One can see that for **n=2**, $\Delta_2^{\rm d}(0)\leq 0$ for all values of $\varepsilon_{\rm CF}$ and has a maximum at small $\varepsilon_{\rm CF}>0$. Instead, for **n=4**, $\Delta_2^{\rm d}(0)$ decreases quickly and becomes almost unvarying for $\varepsilon_{\rm CF}>0$. The value of $\Delta_2^{\rm d}(0)$ is small for the **n=1** and **n=5** cases, while it becomes larger for the **n=2** and **n=4** for large negative $\varepsilon_{\rm CF}$.
Finally, for what concerns to temperature effect, $\Delta_1^{\rm d}(0)$ and $\Delta_2^{\rm d}(0)$ are weakly temperature-dependent.

7

Summary

This work aimed to investigate the electronic properties of correlated single-layered perovskites. To this end, we combined density functional theory (DFT), in the local-density approximation (LDA) with dynamical mean-field theory (DMFT). Specifically, we studied the effects of crystal-field and spin-orbit interaction on the system.

Although LDA fails to capture the essential physics of strongly-correlated systems, it can be used to construct minimal model Hamiltonians, which are material-specific and have as few degrees of freedom and parameters as possible. We first discussed in chapter 2 the basic concepts of DFT and the LDA for the exchange-correlation functional. Then, in chapter 3 we introduced the DMFT method. In DMFT, the lattice Hubbard model is mapped onto a self-consistent quantum-impurity model which can be solved exactly via numerical methods. In chapter 4 we reviewed one of the most flexible solvers, continuous-time quantum Monte Carlo. Correlated perovskites can be described via multi-orbital Hubbard models, which we discussed in chapter 5. This chapter was followed by a short overview of single-particle Green functions.

After we presented the methods and tools which we used throughout the thesis, in chapter 6 we discussed our results. We started with an introduction to representative single-layered t_{2g}^n perovskites. We calculated the electronic properties for the different filling numbers, n=1, 2, 3, 4, 5.

Firstly, we investigated the effects of crystal-field in the absence of spin-orbit (SO) coupling. We fixed the direct, U, and exchange, J, screened Coulomb parameters and varied the t_{2g} crystal-field splitting, $\varepsilon_{\mathrm{CF}}$, from $-3J$ to $3J$; at the extremes of this interval, we can reach the regime in which the Hund's

rules break down. A key question is how large $\varepsilon_{\mathrm{CF}}$ should be to map the model onto a smaller effective model. We found that this limit can be only reached for very large $|\varepsilon_{\mathrm{CF}}|$. Our investigation of spectral functions, effective-mass enhancement and quasi-particle scattering rate showed that the system is a metal for n=1, 2, 5 at all considered values of $\varepsilon_{\mathrm{CF}}$. For the n=4 case, a Mott-transition is obtained only for very large positive $\varepsilon_{\mathrm{CF}}$. For the n=3 case, instead, the system is an insulator except for very large $|\varepsilon_{\mathrm{CF}}|$. The other essential aspect is the effects of correlation on the Fermi surface. These effects are related to the zero frequency self-energies which yield a low energy effective $\varepsilon_{\mathrm{CF}}$. Typically, the Coulomb interaction enhances $\varepsilon_{\mathrm{CF}}$. If the low energy effective $\varepsilon_{\mathrm{CF}}$ becomes sufficiently large, it modifies the shape of the Fermi surface, makes some of the bands inert and eventually leads to an orbitally-ordered metal-insulator transition. Here, we found that the low energy effective $\varepsilon_{\mathrm{CF}}$ can be either enhanced or reduced, depending on n and the initial value of $\varepsilon_{\mathrm{CF}}$. Furthermore, our results showed that these modifications are to a large extent dynamical in nature.
Secondly, we investigated how these results changed switching on the SO interaction. We found that the latter introduces a strong intra-orbital coupling, and thus we studied the evolution of parameters in the natural orbital basis. We identified the point at which the behavior is the one of an effectively-degenerate t_{2g} system. We found that the low energy natural orbital energy correction, due to the many-body effects is more pronounced for the n=2 and n=4, in comparison with n=1 and n=5.

Appendix A

Kramers-Kronig relations

In the Lehmann representation, the retarded Green function in the frequency domain, using the set of eigenstates, $\{|n\rangle\}$, of the full Hamiltonian $\hat{H}$ as basis set, can be expressed as

$$\mathcal{C}_{\alpha}^{R}(\nu) = \frac{1}{Z}\sum_{nn'} \frac{\langle n|c_{\alpha}|n'\rangle \langle n'|c_{\alpha}^{\dagger}|n\rangle}{\nu + E_n - E_{n'} + i\delta} \left(\mathrm{e}^{-\beta E_n} + \mathrm{e}^{-\beta E_{n'}}\right). \tag{A.1}$$

Here, the index α is a flavor, $c^{\dagger}\,(c)$ is a fermionic creation (annihilation) operator, E_n ($E_{n'}$) is the corresponding eigenenergy of $|n\rangle$ ($|n'\rangle$) and δ is an infinitesimally small positive number. In addition, Z is the partition function

$$Z{=}\mathrm{Tr}\left[\mathrm{e}^{-\beta(\hat{H}-\mu\hat{N})}\right],\ \beta = 1/k_B T.$$

This equation shows that the complex function, $G(z)$, obtained from $\mathcal{C}^{R}(\nu)$, replacing ν with complex variable z, thanks to the positive infinitesimal δ, is analytic in the upper half plane and has a series of poles at $E_{n'} - E_n$ along the real axis. The Green function is related to the self energy via the Dyson equation, $G^{-1}(z){=}G_0^{-1}(z) - \Sigma(z)$, where $G_0^{-1}(z)$ is the Green function of the non-interacting system. Thus the self energy is an analytical function as well. Let us consider the integral on the real axis of an analytic function $f(z)$

$$X = \int_{-\infty}^{+\infty} \frac{f(\nu')}{\nu' - \nu + i\delta}\, d\nu', \tag{A.2}$$

assuming that $f(z)$ vanishes in the limit $|z| \to \infty$. The positive infinitesimal δ ensures that the poles of the integrand at $\nu'{=}\nu - i\delta$ lie in the lower half-plane. Therefore, using the Cauchy integral theorem, the integral has to

vanish for any closed contour $\mathcal{C}$ in the upper half-plane:

$$I_{\mathcal{C}} = \oint_{\mathcal{C}} \frac{f(z)}{z - \nu + i\delta}\, dz = 0. \tag{A.3}$$

The contour $\mathcal{C}$ is made by a straight line along the real axis and a semicircle. If $f(z)$ decays fast enough at infinity, faster than $\frac{1}{z}$, then the integrand vanishes on the semicircle. Hence the integral on the real axis, has to vanish too. For the self energy the real part of $\Sigma(\nu')$ can be finite at $\nu' \to \infty$, the condition of the theorem is only met if we subtract from the real part of the self energy its infinite frequency limit $\mathbf{Re}\,\Sigma(\infty)$. Next, using the Sokhotski-Plemelj formula,

$$\frac{1}{\nu + i\delta} = \mathcal{P}\frac{1}{\nu} - i\pi\delta(\nu),$$

where $\mathcal{P}$ is the Cauchy principal value

$$\int_{-\infty}^{+\infty} \mathcal{P}\frac{1}{\nu}\, d\nu = \int_{-\infty}^{\epsilon} \frac{1}{\nu}\, d\nu + \int_{\epsilon}^{+\infty} \frac{1}{\nu}\, d\nu,$$

and $\delta(\nu)$ the Dirac delta function. Thus Eq. (A.2) yields

$$\mathcal{P}\int_{-\infty}^{+\infty} \frac{\Sigma(\nu') - \mathbf{Re}\,\Sigma(\infty)}{\nu' - \nu}\, d\nu' - i\pi\left\{\Sigma(\nu) - \mathbf{Re}\,\Sigma(\infty)\right\}. \tag{A.4}$$

It then follows that the real and imaginary parts of self energy are Hilbert transforms of one another and satisfy the *Kramers-Kronig relations*:

$$\mathbf{Re}\,\Sigma(\nu) - \mathbf{Re}\,\Sigma(\infty) = \frac{1}{\pi}\mathcal{P}\int_{-\infty}^{+\infty} \frac{\mathbf{Im}\,\Sigma(\nu')}{\nu' - \nu}\, d\nu', \tag{A.5}$$

$$\mathbf{Im}\,\Sigma(\nu) = -\frac{1}{\pi}\mathcal{P}\int_{-\infty}^{+\infty} \frac{\mathbf{Re}\,\Sigma(\nu') - \mathbf{Re}\,\Sigma(\infty)}{\nu' - \nu}\, d\nu'. \tag{A.6}$$

References

1. S. H. Simon, The Oxford Solid State Basics,
(Oxford University Press, 2016).
2. W. Kohn, Rev. Mod. Phys. **71**, 1253 (1998).
3. U. von Barth, Physica Scripta **109**, 9 (2004).
4. P. Hohenberg and W. Kohn, Phys. Rev. **136**, B864 (1964).
5. W. Kohn and S. Sham, Phys. Rev. **14**, A1133 (1965).
6. The LDA+DMFT approach to strongly correlated materials,
E. Pavarini, E. Koch, D. Vollhardt, and A. I. Lichtenstein (eds),
Modeling and Simulation, Vol. **1**
(Verlag des Forschungszentrum Jülich, 2011).
7. Many-Body Methods for Real Materials,
E. Pavarini, E. Koch, and S. Zhang (eds),
Modeling and Simulation, Vol. **9**
(Verlag des Forschungszentrum Jülich, 2019).
8. D. M. Ceperley and B. J. Alder, Phys. Rev. Lett. **45**, 566 (1980).
9. DMFT at 25: Infinite Dimensions,
E. Pavarini, E. Koch, D. Vollhardt, and A. I. Lichtenstein (eds),
Modeling and Simulation, Vol. **4**
(Verlag des Forschungszentrum Jülich, 2014).
10. O. Gunnarsson, O. K. Andersen, O. Jepsen, and J. Zaanen,
Phys. Rev. B **37**, 1708 (1989).
11. F. Aryasetiawan, M. Imada, A. Georges, G. Kotliar, S. Biermann, and
A. I. Lichtenstein, Phys. Rev. B **70**, 195104 (2004).
12. E. Pavarini, A. Yamasaki, J. Nuss, and O. K. Andersen,
New J. Phys. **7**, 188 (2005).

13. N. Marzari and D. Vanderbilt, Phys. Rev. B **56**, 12847 (1997).

14. P. Fazekas, Lecture Notes on Electron Correlation and Magnetism, (World Scientific, 1999).

15. E. H. Lieb and F. Y. Wu, Phys. Rev. Lett. **20**, 1445 (1968).

16. W. Metzner and D. Vollhardt, Phys. Rev. Lett. **62**, 324 (1989).

17. A. Georges and G. Kotliar, Phys. Rev. B **45**, 6479 (1992).

18. E. Müller-Hartmann, Z Phys B Condensed Matter **74**, 507 (1989); Int. J. Mod. Phys. B **3**, 2169 (1989).

19. M. Caffarel and W. Krauth, Phys. Rev. Lett. **72**, 1545 (1994).

20. R. Bulla, T. A. Costi, and D. Vollhardt, Phys. Rev. B **64**, 045103 (2001).

21. E. Gull, A. J. Millis, A. I. Lichtenstein, A. N. Rubtsov, M. Troyer, and P. Werner, Rev. Mod. Phys. **83**, 349 (2011).

22. W. Krauth, Statistical mechanics: algorithms and computations, (Oxford University Press, 2012).

23. A. N. Rubtsov, V. V. Savkin, and A. I. Lichtenstein, Phys. Rev. B **72**, 035122 (2005).

24. S. M. A. Rombouts, K. Heyde, and N. Jachowicz, Phys. Rev. Lett. **82**, 4155 (1999).

25. E. Gull, P. Werner, O. Parcollet, and M. Troyer, Europhys. Lett. **82**, 57003 (2008).

26. P. Werner, A. Comanac, L. de' Medici, M. Troyer, and A. J. Millis, Phys. Rev. Lett. **97**, 076405 (2006).

27. F. F. Assaad and T. C. Lang, Phys. Rev. B **76**, 035116 (2007).

28. M. Hohenadler, Z. Y. Meng, T. C. Lang, S. Wessel, A. Muramatsu, and F. F. Assaad, Phys. Rev. B **85**, 115132 (2012).

29. J. Yoo, S. Chandrasekharan, R. K. Kaul, D. Ullmo, and H. U. Baranger, J. Phys. A **38**, 10307 (2005).

30. Correlated Electrons: From Models to Materials, E. Pavarini, E. Koch, F. Anders, and M. Jarrell (eds), Modeling and Simulation, Vol. **2** (Verlag des Forschungszentrum Jülich, 2012).

31. L. D. Landau and E. M. Lifshitz, Lehrbuch der Theoretischen Physik, (Akademie verlag Berlin, 1988).

32. H. Bruus and K. Flensberg, Many-Body Quantum Theory in Condensed Matter Physics: An Introduction, (Oxford University Press, 2004).

33. J. Bednorz and K. A. Müller, Z Phys B Condensed Matter **64**, 189 (1986).

34. Y. Maeno, H. Hashimoto, K. Yoshida, S. Nishizaki, T. Fujita, J. G. Bednorz, and F. Lichtenberg, Nature **372**, 532 (1994).

35. C. S. Alexander, G. Cao, V. Dobrosavljevic, S. McCall, J. E. Crow, E. Lochner, and R. P. Guertin, Phys. Rev. B **60**, R8422(R) (1999).

36. O. Friedt, M. Braden, G. André, P. Adelmann, S. Nakatsuji, and Y. Maeno, Phys. Rev. B **63**, 174432 (2001).

37. S. Nakatsuji and Y. Maeno, Phys. Rev. Lett. **84**, 2666 (2000).

38. J. Burschka, N. Pellet, S.-J. Moon, R. Humphry-Baker, P. Gao, M. K. Nazeeruddin, and M. Grätzel, Nature **499**, 7458 (2013).

39. M. Neupane, P. Richard, Z.-H. Pan, Y.-M. Xu, R. Jin, D. Mandrus, X. Dai, Z. Fang, Z. Wang, and H. Ding, Phys. Rev. Lett. **103**, 097001 (2009).

40. S. Nakatsuji, D. Hall, L. Balicas, Z. Fisk, K. Sugahara, M. Yoshioka, and Y. Maeno, Phys. Rev. Lett. **90**, 137202 (2003).

41. A. Tamai, M. P. Allan, J. F. Mercure, W. Meevasana, R. Dunkel, D. H. Lu, R. S. Perry, A. P. Mackenzie, D. J. Singh, Z.-X. Shen, and F. Baumberger, Phys. Rev. Lett. **101**, 026407 (2008).

42. R. A. Borzi, S. A. Grigera, R. S. Perry, N. Kikugawa, K. Kitagawa, Y. Maeno, and A. P. Mackenzie, Phys. Rev. Lett. **92**, 216403 (2004).

43. J. Lee, M. P. Allan, M. A. Wang, J. Farrell, S. A. Grigera, F. Baumberger, J. C. Davis, and A. P. Mackenzie, Nature **5**, 800 (2009).

44. M. Malvestuto, E. Carleschi, R. Fittipaldi, E. Gorelov, E. Pavarini, M. Cuoco, Y. Maeno, F. Parmigiani, and A. Vecchione, Phys. Rev. B **83**, 165121 (2011).

45. E. Pavarini and I. I. Mazin, Phys. Rev. B **74**, 035115 (2006).

46. A. P. Mackenzie, S. R. Julian, A. J. Diver, G. J. McMullan, M. P. Ray, G. G. Lonzarich, Y. Maeno, S. Nishizaki, and T. Fujita, Phys. Rev. Lett. **76**, 3786 (1996).

47. A. P. Mackenzie, S.-I. Ikeda, Y. Maeno, T. Fujita, S. R. Julian, and G. G. Lonzarich, J. Phys. Soc. Jpn. **67**, 385 (1998).

48. A. P. Mackenzie, S. R. Julian, G. G. Lonzarich, Y. Maeno, and T. Fujita, Phys. Rev. Lett. **78**, 2271 (1997).

49. S. Liu, H. Weng, D. Mou, W. Zhang, Q. Wu, J. He, G. Liu, L. Zhao, H. Liu, X. Jia, Y. Peng, S. He, X. Dong, J. Zhang, Z. Q. Mao, C. Chen, Z. Xu, X. Dai, Z. Fang, and X. J. Zhou, Phys. Rev. B **86**, 165112 (2012).

50. D. H. Lu, M. Schmidt, T. R. Cummins, S. Schuppler, F. Lichtenberg, and J. G. Bednorz, Phys. Rev. Lett. **76**, 4845 (1996).

51. A. Damascelli, D. H. Lu, K. M. Shen, N. P. Armitage, F. Ronning, D. L. Feng, C. Kim, Z.-X. Shen, T. Kimura, Y. Tokura, Z. Q. Mao, and Y. Maeno, Phys. Rev. Lett. **85**, 5194 (2000).

52. M. W. Haverkort, I. S. Elfimov, L. H. Tjeng, G. A. Sawatzky, and A. Damascelli, Phys. Rev. Lett. **101**, 026406 (2008).

53. G. Zhang, E. Gorelov, E. Sarvestani, and E. Pavarini, Phys. Rev. Lett. **116**, 106402 (2016).

54. L. de' Medici, J. Mravlje, and A. Georges, Phys. Rev. Lett. **107**, 256401 (2011).

55. C. Bergemann, A. P. Mackenzie, S. R. Julian, D. Forsythe, and E. Ohmichi, Adv. Phys. **52**, 639 (2003).

56. N. J. C. Ingle, K. M. Shen, F. Baumberger, W. Meevasana, D. H. Lu, Z.-X. Shen, S. Nakatsuji, Z. Q. Mao, Y. Maeno, T. Kimura, and Y. Tokura, Phys. Rev. B **72**, 205114 (2005).

57. T. E. Kidd, T. Valla, A. V. Fedorov, P. D. Johnson, R. J. Cava, and M. K. Haas, Phys. Rev. Lett. **94**, 107003 (2005).

58. Z. V. Pchelkina, I. A. Nekrasov, T. Pruschke, A. Sekiyama, S. Suga, V. I. Anisimov, and D. Vollhardt, Phys. Rev. B **75**, 035122 (2007).

59. G. Zhang and E. Pavarini, Phys. Rev. B **99**, 125102 (2019).

60. F. Aryasetiawan, M. Imada, A. Georges, G. Kotliar, S. Biermann, and A. I. Lichtenstein, Phys. Rev. B **70**, 195104 (2004).

61. R. S. Perry, F. Baumberger, L. Balicas, N. Kikugawa, N. J. C. Ingle, A. Rost, J. F. Mercure, Y. Maeno, Z. X. Shen, and A. P. Mackenzie, New J. Phys. **8**, 175 (2006).

62. F. Baumberger, N. J. C. Ingle,W. Meevasana, K. M. Shen, D. H. Lu, R. S. Perry, A. P. Mackenzie, Z. Hussain, D. J. Singh, and Z.-X. Shen, Phys. Rev. Lett. **96**, 246402 (2006).

63. B. J. Kim, J. Yu, H. Koh, I. Nagai, S.-I. Ikeda, S.-J. Oh, and C. Kim, Phys. Rev. Lett. **97**, 106401 (2006).

64. E. Ko, B. J. Kim, C. Kim, and H. J. Choi, Phys. Rev. Lett. **98**, 226401 (2007).

65. M. W. Haverkort, I. S. Elfimov, L. H. Tjeng, G. A. Sawatzky, and A. Damascelli, Phys. Rev. Lett. **101**, 026406 (2008).

66. G.-Q. Liu, V. N. Antonov, O. Jepsen, and O. K. Andersen, Phys. Rev. Lett. **101**, 026408 (2008).

67. K.-A. Ahn, K.-W. Lee, and J. Kuneš, J. Phys. Condens. Matter **27**, 085602 (2015).

68. W. E. Pickett, D. Singh, D. A. Papaconstantopoulos, H. Krakauer, M. Cyrot, and F. Cyrot-Lackmann, Physica C, **162-164**, 1433 (1989).

69. J. Matsuno, Y. Okimoto, M. Kawasaki, and Y. Tokura, Phys. Rev. Lett. **95**, 176404 (2005).

70. V. Giannakopoulou, P. Odier, J. M. Bassat, and J. P. Loup, Solid State Commun. **93**, 579 (1995).

71. R. Arita, A. Yamasaki, K. Held, J. Matsuno, and K. Kuroki, Phys. Rev. B **75**, 174521 (2007).

72. Y. Imai, I. Solovyev, and M. Imada, Phys. Rev. Lett. **95**, 176405 (2005).

73. O. Tchernyshyov, Phys. Rev. Lett. **93**, 157206 (2004).

74. S. Gangadharaiah, J. Sun, and O. A. Starykh, Phys. Rev. Lett. **100**, 156402 (2008).

75. G. Jackeli and G. Khaliullin, Phys. Rev. Lett. **102**, 017205 (2009).

76. G. Chen, L. Balents, and A. P. Schnyder, Phys. Rev. Lett. **102**, 096406 (2009).

77. L. Ortega-San-Martin, A. J. Williams, J. Rodgers, J. P. Attfield, G. Heymann, and H. Huppertz, Phys. Rev. Lett. **99**, 255701 (2007).

78. H. Sakurai, J. Phys. Soc. Jpn. **83**, 123701 (2014).

79. J. Jeanneau, P. Toulemonde, G. Remenyi, A. Sulpice, C. Colin, V. Nassif, E. Suard, E. Salas Colera, G. R. Castro, F. Gay, C. Urdainz, R. Weht, C. Fevrier, A. Ralko, C. Lacroix, A. A. Aligia, and M. Núñez-Regueiro, Phys. Rev. Lett. **118**, 207207 (2017).

80. J. Jeanneau, P. Toulemonde, G. Remenyi, A. Sulpice, C. V. Colin, V. Nassif, E. Suard, F. Gay, R. Weht, and M. Núñez-Regueiro, Europhys. Lett. **127**, 27002 (2019).

81. J. Mravlje, M. Aichhorn, T. Miyake, K. Haule, G. Kotliar, and A. Georges, Phys. Rev. Lett. **106**, 096401 (2011).

82. M. Jarrell and J. E. Gubernatis, Phys. Rep. **269**, 133 (1996).

83. G. Zhang and E. Pavarini, Phys. Status Solidi Rapid Res. Lett. **12**, 1800211 (2018).

84. E. Sarvestani, G. Zhang, and E. Pavarini, Phys. Rev. B **97**, 085141 (2018).

Acknowledgments

I would like to take this opportunity to express my sincere appreciation to the individuals and institutions who have supported and guided me throughout my doctoral journey. Completing this thesis would not have been possible without their invaluable contributions.

First and foremost, I am grateful to my supervisor, **Prof. Eva Pavarini**, for introducing me to strongly correlated materials, enriching my research experience, and for her guidance and constructive feedback. I am especially appreciative of her mentorship, particularly during the challenging times of the pandemic, for reviewing my thesis with patience and care, and investing substantial time in the process.

I am thankful to **Prof. Stefan Wessel** for being the second reviewer of my thesis and offering very useful feedback.

I would also like to thank **Prof. Erik Koch** for providing very valuable comments on the thesis, and interesting discussions.

I am grateful to **Prof. Matthias Wuttig** and **Prof. Silvia Viola Kusminskiy** for being the members of my Ph.D. committee.

I greatly appreciate the assistance and insights provided by my colleague, **Dr. Julian Mußhoff**, regarding computational many-body physics, Python codes, and group theory. Additionally, I extend my thanks to **Dr. Qian Zhang** for his support and for fostering a friendly work environment.

I am sincerely grateful to **IAS-3** for funding my Ph.D., and also to the **Jülich Supercomputing Center (JSC)**, which made this research possible.

I would also like thank to **Ms. Luise Snyders** for her support with administrative issues.

I am deeply thankful to all those who positively influenced me during my educational journey. I thank **Dr. Jahanfar Abouie**, my master supervisor, who always encouraged me and instilled a positive attitude. Additionally, I would like to express my heartfelt gratitude to **Dr. Abolfazl Jafari** and

Prof. Mohammad Mardani for introducing me to Quantum Mechanics and Condensed Matter Physics during my bachelor studies.
This work would not have been possible without the care and support of my friends. I would like to thank **Pegah, Irene, Shirin, Somayeh, and Neda** for always lending an ear and for continuously encouraging me to gain confidence in my work.
Most of all, I thank my parents, **Zahra and Esmaeel** for their loving care and attention during my difficult moments. I am incredibly grateful to my siblings, **Hamidreza, Ahmadreza, and Leyla**, and my nieces, **Fatemeh and Zeynab**, for their unconditional support and interest in my work.
Finally, I dedicate this thesis to all those who persistently support justice, equality, and freedom worldwide, including the courageous Iranians who initiated the "WOMAN, LIFE, FREEDOM" movement and firmly defend their cause despite difficult obstacles.

Declaration of Authorship

I, Neda Riahisamani, declare that this thesis and the work presented in it are my own and has been generated by me as the result of my own original research.
I do solemnly swear that:

1. This work was done wholly or mainly while in candidature for the doctoral degree at this faculty and university;

2. Where any part of this thesis has previously been submitted for a degree or any other qualification at this university or any other institution, this has been clearly stated;

3. Where I have consulted the published work of others or myself, this is always clearly attributed;

4. Where I have quoted from the work of others or myself, the source is always given. This thesis is entirely my own work, with the exception of such quotations;

5. I have acknowledged all major sources of assistance;

6. Where the thesis is based on work done by myself jointly with others, I have made clear exactly what was done by others and what I have contributed myself;

7. None of this work has been published before submission.

24. January 2024